University of Alberta

DEVELOPMENT OF SILICON CARBONITRIDE NANOMECHANICAL RESONATORS FOR
BIOLOGICAL DETECTION APPLICATIONS

by

Lee M. Fischer ©

A thesis submitted to the Faculty of Graduate Studies and Research in partial
fulfillment of the requirements for the degree of **Master of Science**

Department of Electrical and Computer Engineering

Edmonton, Alberta
Fall 2007

Library and
Archives Canada

Bibliothèque et
Archives Canada

Published Heritage
Branch

Direction du
Patrimoine de l'édition

395 Wellington Street
Ottawa ON K1A 0N4
Canada

395, rue Wellington
Ottawa ON K1A 0N4
Canada

NOTICE:
The author has granted a non-exclusive license allowing Library and Archives Canada to reproduce, publish, archive, preserve, conserve, communicate to the public by telecommunication or on the Internet, loan, distribute and sell theses worldwide, for commercial or non-commercial purposes, in microform, paper, electronic and/or any other formats.

The author retains copyright ownership and moral rights in this thesis. Neither the thesis nor substantial extracts from it may be printed or otherwise reproduced without the author's permission.

AVIS:
L'auteur a accordé une licence non exclusive permettant à la Bibliothèque et Archives Canada de reproduire, publier, archiver, sauvegarder, conserver, transmettre au public par télécommunication ou par l'Internet, prêter, distribuer et vendre des thèses partout dans le monde, à des fins commerciales ou autres, sur support microforme, papier, électronique et/ou autres formats.

L'auteur conserve la propriété du droit d'auteur et des droits moraux qui protège cette thèse. Ni la thèse ni des extraits substantiels de celle-ci ne doivent être imprimés ou autrement reproduits sans son autorisation.

In compliance with the Canadian Privacy Act some supporting forms may have been removed from this thesis.

While these forms may be included in the document page count, their removal does not represent any loss of content from the thesis.

Conformément à la loi canadienne sur la protection de la vie privée, quelques formulaires secondaires ont été enlevés de cette thèse.

Bien que ces formulaires aient inclus dans la pagination, il n'y aura aucun contenu manquant.

Canada

I dedicate this thesis to my parents: Harold and Gale, for supporting and encouraging me to do my best, and for inspiring me to do things "my way".

Abstract

This work investigates the deposition of silicon carbonitride by plasma enhanced chemical vapor deposition and the development of nanomechanical resonators. The film composition was controlled through precursor gas flow ratio (NH_3:DES) modulation. Post-deposition annealing was found to remove incorporated hydrogen, changing the intrinsic stress from compressive to tensile. Resonant assaying of nanocantilevers yielded a speed of sound of 6.20×10^3 m/s and 8.35×10^3 m/s for high and low carbon films, respectively. Nanobridges with stress-dominated resonant behavior exhibited a L^{-1} dependence of length on frequency, as well as a dramatic increase in quality, up to $Q = 26\ 000$. Vapor-deposition of mercaptopropyl trimethoxysilane (MPTMS) was measured in real-time, resulting in a detected mass-per-area-per-hour loading of 13.6 ± 0.4 μg-m^{-2}/h. The presence of silanol groups was confirmed on the SiCN surface, which facilitated the binding of streptavidin via biotin. Streptavidin was specifically bound to the SiCN resonator surface by MPTMS/biotin, and the protein mass-per-area detected was 3.6 mg/m^2, corresponding to 1 protein per 27 nm^2.

Acknowledgements

I would first like to thank my supervisor, Dr. Stéphane Evoy for setting the wheels in motion. It was Dr. Evoy who first introduced me to the field of MEMS/NEMS which, over the past two years, has become my world. The concepts and ideas he introduced to me forged the base upon which my entire expertise now rests on. He has supported my efforts and kept me focused on this great scientific journey. Indeed, to Dr. Evoy, very many thanks.

Thanks to Shane McColman who guided me in the ways of microfabrication during my first months. Shane was always there to train me or answer a question, no matter how trivial. Thanks for putting up with a beginner.

Dr. Ken Westra, whose patience and helpful discussions kept me and my project from derailing many times. Additional thanks go to Dr. Westra for trusting me and giving me the opportunity to design and teach a section of his course, the experience of which proved invaluable in both technical and interpersonal skills. And thanks to the staff of the University of Alberta Micromachining and Nanofabrication Facility, specifically Keith Franklin, Bob Brebber, Stephanie Bozic, Kristian Olsen, Les Schowalter, Melissa Hawrelechko, and Scott Munro for providing an absolutely top-notch facility that will forever remain in the minds of those who use it. Without their help, all wafers would forever remain flat and grey.

Thanks to Dr. Mark T. McDermott and Dr. Jillian Buriak for very useful discussions on surface functionalization, and Wally Qiu, Ni Yang, and Dr. Vincent Wright for carrying out chemistry protocols, and putting up with a non-chemist. Also to Dr. Dimitre Karpuzov for teaching me the ways of XPS, and providing an invaluable facility.

To fellow students, past and present: Neal Wilding for help with experiments in my

first year (when time got short), Andrew Murray and Aruna Kroetch for their expertise in SEM countless times, Luc Gervais for sharing his biology knowledge, and Miro Belov for his assistance with resonance measurements. Also, thanks goes to Colin Ophus for his (sometimes insane) scientific discussions, and Erik Luber for his love of math, both of whose contributions are not forgotten.

A very many thanks to Shufen Tsoi, who opened up her home and provided me with the perfect place to write my thesis, a thesis that would not exist without her kindness. And a special thanks to Chuhong Fang, who supported me before and during the writing of my thesis, and continues to provide encouragement in my life pursuits.

Finally, an additional thanks to my friends, who, each in their own way, taught me to live.

Table of Contents

List of Tables

List of Figures

List of Abbreviations

1G	First-generation
2G	Second-generation
AFM	Atomic force microscope
BOE	Buffered oxide etch
CMOS	Complementary metal-oxide semiconductor
Da	Dalton, $1.660538783 \times 10^{-27}$ kg
DES	Diethylsilane
DNA	Deoxyribonucleic acid
EBL	Electron-beam lithography
FE-SEM	Field-emission scanning electron microscope
FT-IR	Fourier-transform infrared spectroscopy
GADDS	General area detector diffraction software
HPDP	Hexylpyridyl dithiopropionamide
IC	Integrated circuit
IPA	Isopropanol
KOH	Potassium hydroxide

LPCVD	Low-pressure chemical vapor deposition
MEMS	Microelectromechanical systems
MIBK	Methylisobutylketone
MPA	Mercaptopropionic acid
MPTMS	Mercaptopropyl trimethoxysilane
NEMS	Nanoelectromechanical systems
ODT	Octadecanethiol
PECVD	Plasma-enhanced chemical vapor deposition
PMMA	Polymethyl methacrylate
poly-Si	Polycrystalline silicon
PZT	Lead-zirconium titanate
QCM	Quartz-crystal microbalance
RIE	Reactive ion etch
RF	Radio frequency
SAM	Self-assembled monolayer
sccm	Standard cubic centimetre per minute
SEM	Scanning electron microscope
SPM	Scanning probe microscopy
SPR	Surface plasmon resonance
XPS	X-ray photoelectron spectroscopy
XRD	X-ray diffraction

1

An Introduction to MEMS

1.1 What are MEMS?

Microelectromechanical systems, or MEMS, reside under the broader umbrella term microsystems technology, which refers to devices or groups of devices designed to perform a certain function while having dimensions well under 1 mm. The crux of this *microsystems* term is that everything in the system is constructed on a common substrate, or rather the system is *integrated*. These systems can be complementary metal-oxide semiconductor (CMOS) integrated circuitry (IC) for one of many applications (personal computers, signal processing, cellular telephones, etc.), or sensors/actuators of some type. Sensor microsystems consist of a sensing element, which transduces the external stimulus into an electrical signal, and the supporting circuitry, which receives the electrical signal and processes it for further interpretation [1]. Other microsystems include those in which a microactuator is employed to perform a useful task, such as micro-manipulation or transport. From these three categories (integrated circuits, sensors, and actuators), it is the latter two that can be described as MEMS. Thus, MEMS characterize systems in which a micro-scale mechanical structure is either acted upon by an external force which is transduced into an electrical signal by a specific method, or in which the structure

1

itself generates a mechanical force to perform work. Recently, the MEMS term is no longer restricted to systems in which there moving structures, but also extends to include thermal, magnetic, optical, or other transduction methods [2]. Essentially, MEMS are the microscopic eyes, ears, noses, and hands of the 21st century.

1.2 The Evolution of MEMS

The rapid progression of the MEMS field is due to many of the same factors that have led to the success of integrated circuitry. First, the dominance of silicon MEMS directly mirrors the use of silicon as the primary IC substrate. The ability to produce silicon of amazing purity (99.999999999% pure) [3] in large, flawless single crystals made silicon the material of choice for semiconductor electronics [4]. Based primarily on silicon, fabrication techniques and processes were developed to create integrated circuitry, and over the years these techniques were extensively refined [5]. Wet chemical iso/anisotropic etching of silicon and silicon-containing materials, photolithography for pattern transfer and masking, plasma and dry-etching methods, the wide array of material deposition techniques, impurity doping, as well as many others aided in the advancement of the integrated circuit, and eventually CMOS processing as it is today. Aditionally, all of these techniques lend themselves quite readily to batch fabrication, which drives down the per unit cost, which in turn has greatly contributed to the proliferation of this technology [6]. Perhaps the leading contributor to the growth of silicon MEMS is the success of the IC industry itself, which provides a variety of well-developed fabrication methods that can be directly applied to mechanical structures. Silicon was an appropriate choice as the first MEMS material not only because of its success as a semiconductor or the vast collection of fabrication techniques available to it, but also because of the optimized mechanical properties of its highly pure, defect-free, single-crystal form [7]. Photolithography and etching techniques then allow small mechanical components to be defined and precisely machined. Finally, these factors which allowed for the development of silicon micromechanics from IC technology are also directly responsible for enabling the integration of these two fields to create full-fledged integrated microsystems. Indeed, as described by Petersen in his 1982 paper "Silicon as a Mechanical Material", silicon MEMS and micromechanics is

an evolution of microelectronics technology as the diversity of devices is pushed ever further [7].

1.3   Commercialization of MEMS: The Accelerometer

Microelectromechanical systems have reached maturity within the past decade, it has moved out of the laboratory setting and into our homes, automobiles, and hands. MEMS devices have found applications where their small size, integrated nature, and, often most importantly, their ability to be batch fabricated for a fraction of the cost of conventional devices have made them commercially successful. The quintessential examples of this are the accelerometers built and marketed by Analog Devices, Inc., the most famous of which is the ADXL50 [8], recently replaced by the ADXL78 [9]. The monolithic design of the ADXL50 meant that the entire device, including sensing structure, accompanying circuitry, and self-testing portions could be produced on a single chip of silicon, allowing for rapid, mass-fabrication. This in-turn drove down the cost of the device, making it competitive and even superior to conventional devices for use as an automobile crash sensor for airbag deployment. Recently Analog Devices has been enjoying more success through a partnership with Nintendo Co., Ltd. [10]. The Nintendo Wii video game console launched in November 2006 with the hook of the entire system being its novel control scheme. Instead of relying solely on buttons to play a game, the Analog Devices ADXL330 [11] 3-axis accelerometer senses the forces exerted on the controller and translates them into movements in the games. The existence of such a system is enabled by the accelerometer being incredibly small, low in power consumption, and fully-integrated; the definitive virtues of MEMS.

1.4   Versatility of MEMS: The Atomic Force Microscope

Sensor technology has evolved to the point where it is commercially viable. Two prevalent examples of this are micromachined accelerometers [12, 13] and pressure sensors [14, 15], both of which are being sold by companies such as Analog Devices, Inc. and Honeywell International, Inc. Another versatile example of commercialized MEMS technology is the

atomic force microscope (AFM) [16]. The AFM is a type of scanning probe microscopy (SPM), which employs a specific sensing element brought in close proximity to and then systematically scanned across a target surface. As the *probe* is scanned, it reacts to the variations in height, electrical or magnetic properties, or other surface properties. In the case of the AFM, this probe is a cantilever. The basic mode of AFM operation is *contact mode*, wherein the cantilever is pressed against the sample surface and the close-range repulsive atomic forces cause the cantilever to bend. A laser is trained on the cantilever backside (figure 1.1), and a photodiode senses the reflected light to measure cantilever deflection. The cantilever is scanned across the surface and the tip deflection is monitored to create a three-dimensional image of the surface. Contact mode AFM has two configurations; constant-height and constant-force. In constant-height configuration, the cantilever is held at a set height above the surface and scanned, using the deflection measurements to create a height-mapping of the sample. In constant-force configuration, a control system is used to adjust the vertical height of the tip such that the cantilever deflection (and thus the force on the sample) remains constant, and these height adjustments are then used to crete the image [17, 18]. *Non-contact mode* AFM operation involves the cantilever being driven at its resonant frequency. Equation 1.1 is the basic formula relating the resonant frequency, f, of any spring-mass system to the stiffness or spring constant, k, and the effective load or mass of the oscillator, m (further description of resonant behavior to follow in Chapter 3).

$$f \propto \sqrt{\frac{k}{m}} \tag{1.1}$$

When the tip of the vibrating cantilever is brought close to the surface it experiences an attractive force towards the sample atoms [19, 20]. This atomic force puts a load on the resonating cantilever, thus changing its resonant frequency, which can be used as an indicator of the tip-sample distance.

In non-contact mode the cantilever is approached to the surface so that mild interaction forces cause a frequency shift. Then, as the tip is scanned across the surface the resonance of the cantilever shifts due to an effective change in its spring constant [18]. The change in frequency is detected by a control system and converted into a change in height, which
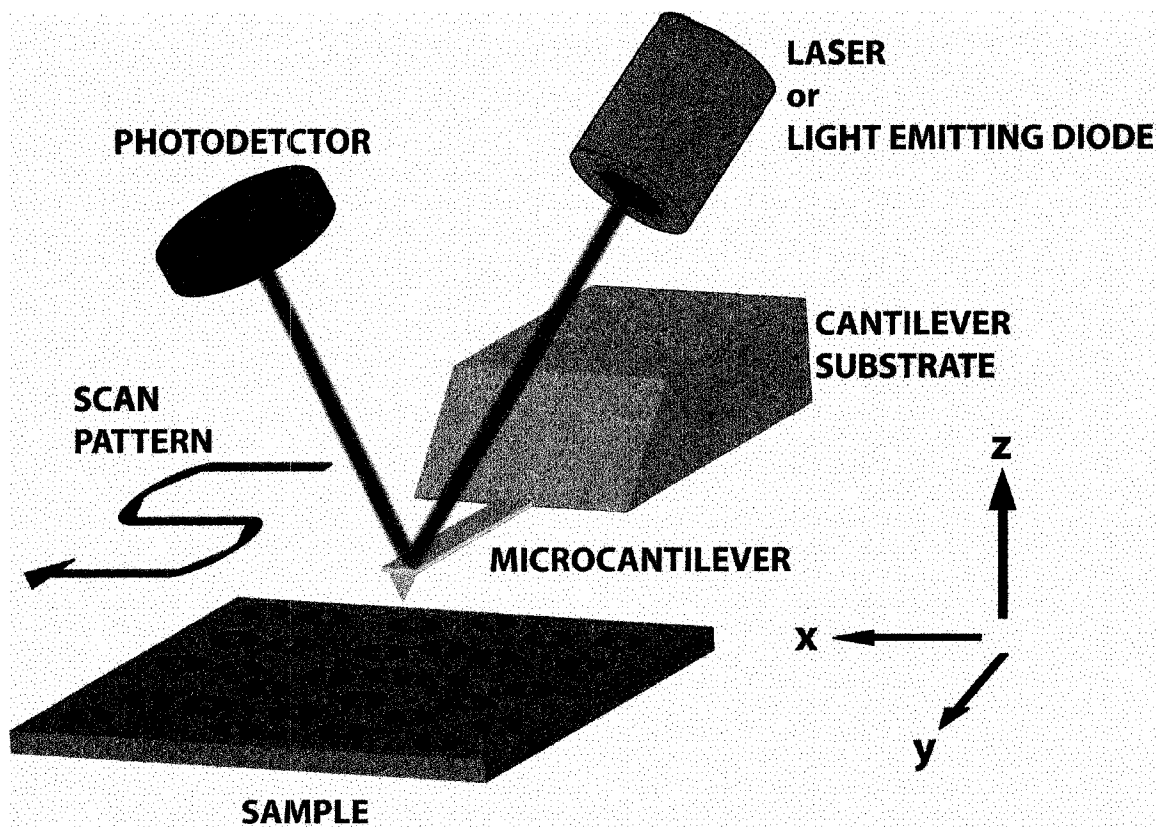
Figure 1.1: Basic configuration of a modern atomic force microscope. The cantilever substrate is typically fastened to the piezo-actuator to provide the driving force for cantilever resonance.

is then applied to the z-axis piezo-actuator to change the tip position to restore the original resonance (similar to contact-mode constant force operation). The tip scans the surface, raising and lowering as the surface changes, and the AFM software once again generates a three-dimensional plot of the sample surface. Yet another form of operation, known as *tapping-mode* is similar to non-contact operation, except the tip makes intermittent physical contact with the surface [20]. For further explanations of these, as well as additional modes of operation, please refer to the cited literature.

However, much of the usefulness of cantilevers has come out of their operation far from any surface. As stated earlier, the resonance of any spring-mass system can be basically described with equation 1.1. If the mass m of the oscillator is increased, then a decrease in resonant frequency occurs. Alternatively, the surface of the cantilever can be coated with a reactive layer, which will exert a surface stress upon adsorption of a specific analyte [21].

This expansion will both cause a deflection of the cantilever, which can be measured by a variety of methods, and change the total spring constant k of the cantilever, leading to a shift in resonant frequency. Operating a cantilever-based sensor in the non-vibrating, deflection-sensing configuration is known as *static mode* operation [22–25], while observing an effect by measuring the shift in resonant frequency is termed *dynamic mode* operation [22,26–28].

Through a variety of configurations and surface treatments microcantilever-based sensing-platforms have been able to transduce a wide range of signal domains into the mechanical domain [29,30]. A cantilever composed of two different materials will deflect under the application of heat, due to a mismatch of coefficients of thermal expansion [31], while adding or subtracting mass will result in a frequency shift (as previously mentioned). Fianlly, chemical reactions on the surface of the cantilever can change the stress-gradient, resulting in a deflection of the beam. Picogram (1 pg = 10^{-12} g) resolution (2.5 pg/Hz) was attained by Sone *et al.* [26] using resonating AFM-style cantilevers. Dynamic mode has been used to perform thermogravimetric studies [28, 32], while cantilever arrays are employed to both simultaneously detect multiple agents, as well as provide unmodified control or base-line cantilevers to compare with the detection structures. The microcantilevers are even moving out of their birthplace of the AFM and into devices specifically designed to detect cantilever bending and resonance, without any intention of scanning a surface, such as the Cantisens platform developed by Concentris [33]. There is even work of integrating cantilevers capable of self-actuation and self-sensing [24] with CMOS circuitry [27,34] to create a monolithic sensing platform.

1.5 NEMS

With the commercial success of MEMS technology as it is, it seems somewhat unnecessary to push the length scales any smaller. MEMS are mature, reliable, and, as have been demonstrated as very marketable. Additionally, as the size of a device decreases the amount of noise in the sensor signal increases [35], partially due to the increasing effect of Brownian motion of the device molecules [36]. Then why would anybody want to miniaturize further?

The mass of an Escherichia coli (E. coli) bacterium is approximately 665 fg [37].

Consider, for example, a typical MEMS (micron-scale) cantilever with a length of 85 um, width of 20 um, and thickness of 4 μm. If fabricated out of bulk, single-crystal silicon, the cantilever would have a mass of 15.6 ng, and a resonant frequency of 2.62 MHz. This corresponds to a mass sensitivity of 12 fg/Hz, which is in agreement with other MEMS cantilevers where values as low as 1 fg/Hz have been reported [37]. Therefore, MEMS structures are certainly capable of bacterium detection. Viruses, however, pose a larger challenge. The mass of a single virus particle can range from 170 - 1000 attograms (1 ag = 10^{-18} g), with some of the largest viruses having masses up to to 9 fg [38–40]. This means that most viruses are at or up to an order of magnitude below the detection limit of many MEMS-size resonators. Look further down in size to single protein molecules, many of which have masses of 10 - 500 zeptograms (1 zg = 10^{-21} g) [41], putting them far below the detection limit of microcantilever sensors. However there are many who would benefit from a resonator based assaying tool for viruses and proteins, including hospitals, biochemical research labs, and even homeland security.

This demand for greater sensitivity is the primary reason for pursuing systems of smaller length scales than MEMS. This is where nanoelectromechnical systems, or NEMS, enter the field, with typical dimensions approaching a few nanometers in some cases. Still a developing technology, NEMS remain restricted to a laboratory setting. However, the potential applications are being quickly developed. Extremely-small mass detection has already been demonstrated multiple times. In 2004, Ilic *et al.* used polycrystalline silicon nanocantilevers with sub-attogram/Hz sensitivity, coated with a monolayer of AcV1 antibody to detect the presence of an insect baculovirius [42], and followed this work by using similar silicon nitride cantilevers to detect a single molecule of 1587 base-pair, double-strand DNA in 2005 [43]. Both Ilic *et al.* and Ekinci *et al.* were successful in obtaining attogram-resolution with nano-scale resonating beams in 2004. Ilic *et al.* detected an adsorbed monolayer of an organo-thiol-based chemical [42] while Ekinci *et al.* measured the incident vapor flux of evaporated Au atoms [44]. In 2006 Yang *et al.* claimed a mass-resolution of 7 zg using a silicon carbide (SiC) double-clamped beam measuring 2.3 μm in length by 150 nm in width by 70 nm in thickness and resonating at 133 MHz [45]. With these groups and others pushing the length scales and resolution limits of

nanomechanical oscillators ever lower, it is quite possible that NEMS could resolve masses in the single-Dalton (1 Da = 1.6605×10^{-24} g) range, ushering in an era of NEMS-based mass spectrometry.

In addition to a decreased length scale over MEMS, NEMS brings additional focus on materials. Unlike MEMS, which are typically fabricated out of silicon and frequently employ etching of the bulk substrate material to make structures (bulk-micromachining), NEMS are regularly fabricated from one or more layers of deposited thin films on the silicon substrate (surface-micromachining). These concepts will be discussed further in a later chapter. This shift in processing method affords NEMS researchers freedom to explore the properties of new materials, as well as new fabrication methods. Carbon nanotubes, studied by many for their fascinating physical properties are entering the NEMS arena as nanomechical oscillators as has been demonstrated by Sazonova *et al.* in 2004 [46]. Multi-walled carbon nanotubes have even been used to measure the mass of attached carbon debris following fabrication with femtogram resolution [47]. Less exotic examples of NEMS material diversification include the use of silicon carbide (SiC) [48, 49], silicon nitride (Si_3N_4) [50, 51], aluminum nitride (AlN) [52], and nanocrystalline diamond films [53, 54] to fabricate mechanical resonators. These materials can be machined in similar ways to silicon, but offer superior mechanical, chemical, or surface properties in specific NEMS applications. In fact, non-silicon NEMS are a highly active field of study, one in which there is still much to be understood. Custom-made materials offer a new degree of control over device behavior that will lead to record-levels of sensitivity and may eventually bring about single-Dalton mass resolution.

1.6 Project Outline

This project is an exploration of silicon carbonitride (SiCN) as a nanomechanical structural material to develop a NEMS biomolecule sensing platform. It covers basic material development, characterization, and machining, to chemical surface modification and finally two proof-of-concept sensors; a quasi-real-time mass detection system capable of sub-femtogram resolution, and a biosensor used to detect the specific binding of the streptavidin protein to the resonator surface via the biotin complex and silane chemistry. The body

of this thesis is comprised of four sections; the results of the first two sections were published in January 2007 [55], while the last two sections are included in a manuscript to be submitted in September 2007. The following is a brief introduction to each of these sections.

1.6.1 Material Development

The development of SiCN for biosensor use begins with its deposition via plasma-enhanced chemical vapor deposition (PECVD), a technique which uses a plasma-discharge to dissociate the gas molecules instead of high temperatures. This deposition method allows a greater range of composition and stress tunability over standard Si_3N_4 via low-pressure chemical vapor deposition (LPCVD), as PECVD simply has more parameters to vary (RF power, temperature, gas flow, frequency). Ammonia (NH_3) and diethylsilane (DES) were the precursor gases used to deposit the SiCN, with nitrogen (N_2) as a carrier gas. The precursor gas flows were adjusted to manipulate the content of silicon, carbon, and nitrogen in the film which in turn affected the mechanical properties of the material, such as elastic modulus and hardness. Upon deposition, the SiCN film was found to have an intrinsic compressive stress. While stress could be controlled by adjusting the gas flows, post-deposition annealing in a 3-zone tube furnace was used to eliminate it completely. X-ray photoelectron spectroscopy (XPS), Fourier transform infrared spectroscopy (FT-IR), atomic force microscopy (AFM), scanning electron microscopy (SEM), and nanoindentation were used to characterize the thin films deposited. It was discovered that the incorporated hydrogen in the films was responsible for the compressive stress, and that annealing released hydrogen and relieved the stress.

1.6.2 Nanomachining and Nanomechanics

Following the stress optimization of the film, construction of nano-scale beam resonators could be undertaken. A standard SiCN on sacrificial-SiO_2 on Si surface-micromachining technique was used as a starting point, and a plasma recipe was developed to etch SiCN to produce vertical sidewalls. Large 1 μm wide cantilevers were initially produced, and used to measure the speed of sound in the material. Doubly-clamped beams, or *bridges*, 800

nm wide were fabricated to determine the effect of a moderate tensile stress on resonant behavior and quality factor Q. It was determined that SiCN was on par with silicon as a mechanical material, and that the intrinsic tensile stress created through post-deposition annealing was bound to dramatically increase the resonance quality factor. Finally, surface- and bulk-micromachining were combined in a potassium-hydroxide (KOH) etch-release process to ensure that the bridges were capable of withstanding liquid chemical processing. Bridges of widths as small as 400 nm were fabricated in preparation for the mass-detection experiments.

1.6.3 Surface Chemistry

An overview of silane chemistry is provided. The characterization of the SiCN surface, as well as the process used to choose an immobilization chemistry are discussed. Different monolayer-forming chemistries were applied to the SiCN surface. It was found that organo-silane molecules covalently bond to the silanol groups on the surface. This was supported by XPS, which showed the presence of oxygen on the SiCN surface, but not in the bulk, and confirmed the attachment of only silane-based chemistries. An explanation of the functionalization scheme and protocol used to immobilize biotin to attach streptavidin for resonant detection is given, in preparation for the last section.

1.6.4 NEMS BioSensing Platform

The work of the previous sections are combined in this last section to complete this project. Surface- and bulk-micromachining were combined in a potassium-hydroxide (KOH) etch-release process to create bridges capable of withstanding liquid chemical processing. Bridges of widths as small as 400 nm were fabricated in preparation for the mass-detection experiments. First, the resonant frequencies of the bridges were measured before and after an 10-hour vapor-phase addition of mercaptopropyl trimethoxysilane (MPTMS). A distinct frequency shift was observed directly related to the addition of the chemical layer, and a mass-per-unit-area of the added layer was determined. Next, the resonant frequency of the bridges was measured, then vapor-phase MPTMS was introduced for a set time in the vacuum chamber containing the resonators. The frequencies are measured again, and

this cycle was repeated every 30 min to 2 h over a total period of 8 h. Collected data shows an initial increase of the resonant frequency during the first 2 h of vapor-deposition, followed by the frequency decrease expected by the loading of mass onto the resonator. An explanation of this frequency increase is offered, and the surface stress induced by the adsorbed monolayer is roughly calculated. Lastly, the biotin-streptavidin protocol discussed in the previous section is applied here and the added mass of streptavidin is detected. It was confirmed experimentally that the observed frequency shift was due to the specific attachment of streptavidin via the biotin layer and not due to some non-specific adsorption to the SiCN resonators.

2

Material Development

This thesis reports the development of a biological sensing platform fabricated using the novel NEMS material silicon carbonitride. This chapter characterizes the control and optimization of the SiCN thin film during and after deposition. The understanding gained in this chapter is required to fabricate the high-quality resonators that will be used in the mass-sensing platform.

2.1 Introduction

While silicon has mostly dominated the field of microelectromechanical systems, this material presents intrinsic limitations related to its structural properties and the limited stability of its surface. Surface-mediated phenomena are specifically expected to dominate the smaller nanoelectromechanical system (NEMS) structures, making the issue of critical importance for the development of high-quality devices offering the highest levels of sensitivity at room temperature [56]. Other materials such as silicon nitride [51](Si_3N_4) and silicon carbide [57,58] (SiC) have been proposed for use as nanomechanical resonators due to their superior mechanical properties as well as advantageous surface characteristics. However, synthesis of these alternate materials is usually performed with low-pressure

12

chemical vapor deposition (LPCVD) at high temperatures (700 °C for Si_3N_4, 1200 °C for SiC) using silane (SiH_4), a highly toxic and unstable precursor. Additionally, Si_3N_4 and SiC films usually involve intrinsic stresses as high as 1 GPa [59, 60] impairing the machining of microstructures [61], with silicon-rich "low-stress" SiN films still retaining residual stresses approaching the $\sigma = 100$ MPa range. This chapter reports the development and characterization of silicon carbonitride deposited by PECVD. It reports the tuning of the film composition and stress, as well as the mechanical properties of the film.

2.2 Overview of PECVD

2.2.1 Plasma Physics

Plasma physics is an intense field of study with applications ranging from thermonuclear fusion, to astrophysics, to interstellar propulsion systems [62]. The most basic definition of a plasma is a gas in which the majority of species have been ionized. There exists a set list of criteria that must be met in order for a gas to be called a plasma, but that discussion is beyond the scope of this work. In the presence of an oscillating electric field, molecules may lose an outer-shell electron, leaving them charged. These charged particles are then susceptible to the oscillating electric field, causing them (and the lost electrons) to move with a certain velocity in a direction dictated by the field. During this motion the ions experience collisions with the surrounding neutral molecules. These collisions can result in the struck molecule gaining kinetic energy as well as the possibility of it losing a electron. The new charged particle is also now imparted kinetic energy by the electric field, allowing it to collide with other neutrals. This collision cascade continues until the bulk of the gas is ions and electrons, oscillating with the electric field, each with their own velocity v_i. The kinetic energy of a particle is classically defined as $\frac{1}{2}mv_i$ where m is the particle mass. If K is the Boltzmann constant, then the effective temperature of a particle is given by equation 2.1:

$$T_i = \frac{\frac{1}{2}mv_i}{\frac{3}{2}K}$$

(2.1)

Thus, while all surrounding objects in a chamber can remain at room temperature, the

energetic particles in a plasma can be at several thousand degrees. The gas in a fluorescent light bulb, for example, has an effective temperature of 20 000 °K. It is this definition of temperature that is relevant in understanding the use of plasmas in chemical vapor deposition. Lastly, the free electrons will regularly recombine with the ions to give off photons, resulting in a *glow discharge*.

2.2.2 Plasma Enhanced Chemical Vapor Deposition

Plasma-enhanced chemical vapor deposition (PECVD) differs from LPCVD in the manner by which precursor gases are dissociated into excited atoms, ions and free radicals. LPCVD uses high temperatures (600 °C - 1200 °C) to decompose the reactant gases into the desired reactive species. However, these high temperatures are incompatible with CMOS processes as they can cause unwanted dopant diffusion and have adverse effects on metal interconnects. Thus, materials deposited by LPCVD for use as nanomechanical resonators are very difficult to merge with integrated circuitry [63]. PECVD uses a glow discharge, or *plasma*, to provide the energy to decompose the reactant gases. Specifically, in the reactor used in this experiment (Trion Technologies Orion PECVD), a radio frequency (RF) plasma, excited at 400 kHz, is created in the thin space between the two parallel plates (figure 2.1).

This allows for deposition from room temperature to 400 °C, as opposed to LPCVD which typically requires temperatures well in excess of 650 °C [63]. Additionally, PECVD allows for a much wider range of pressures to be used, as well as affords the user the opportunity to tune the plasma frequency and power. Thus, PECVD introduces new and expanded parameters which in turn allow for greater control over the deposited film and its chemical and mechanical properties, and is used here to deposit SiCN employing the relatively safer liquid-state diethylsilane [64] (DES) as silicon precursor. The mechanical properties of these films are tuned through control of the gas flow ratio, as well as through post-deposition annealing. The composition of these films are characterized and the results are correlated to the mechanical properties and deposition parameters.
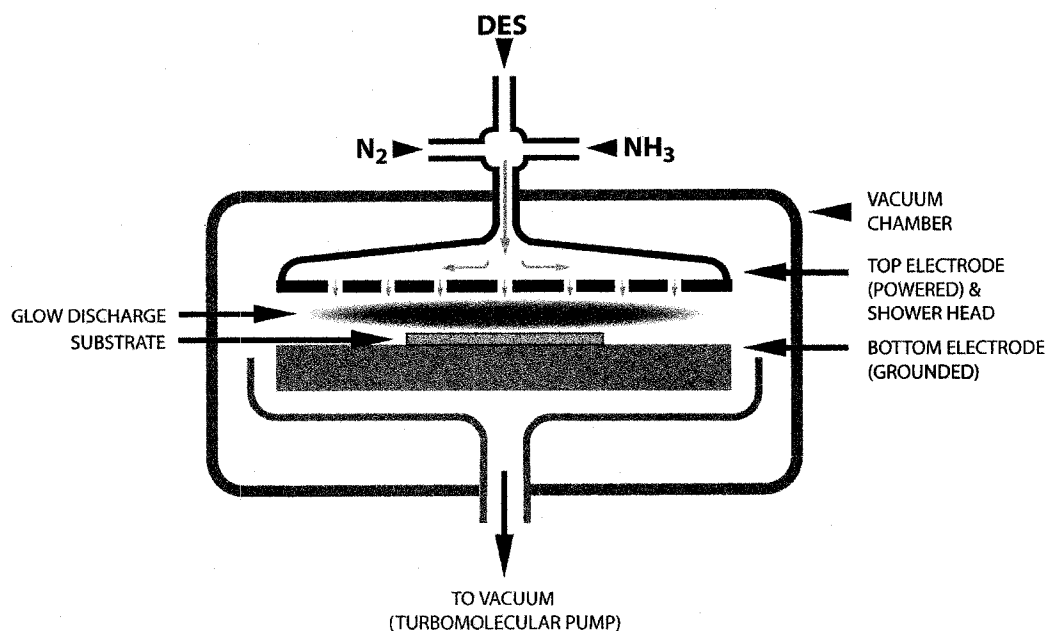
Figure 2.1: The generic setup of a parallel plate plasma-enhanced chemical vapor deposition system.

2.3 Experiment

Wafers of silicon (100) were wet oxidized in a MiniBrute three-zone tube furnace at 1000°C for 1.5 h in order to grow a 450 nm silicon dioxide layer, then cleaned in a Piranha mixture (3:1 sulfuric acid: hydrogen peroxide) for 20 min. The SiCN was deposited in a Trion Technology Orion PECVD system using ammonia (NH_3), nitrogen (N_2), and diethylsilane (DES) at a pressure of $P = 500$ mTorr, temperature of $T = 300$ °C, and power density of p = 0.63 W/cm^2. The other process parameters for the various films deposited are described in Table 2.1. All gas flows are given in standard cubic cm per minute (sccm) and the "-" sign on stress values denotes compression.

Residual stress was assessed using a KLA-Tencor FLX 2320 Flexus film stress measurement system. Films B2-B5 were then annealed under nitrogen atmosphere in the previously mentioned three-zone tube furnace for 1 h each at temperatures ranging from $T = 400$ °C to $T = 700$ °C. Films F and G were annealed at 500 °C until the stress was approximately zero. Films H and I were further annealed until the desired tensile stresses were reached. A Kratos AXIS 165 surface analysis system was employed for x-

Table 2.1: Deposition Parameters of the Silicon Carbonitride Films

Sample	Gas NH$_3$	Flow DES	(sccm) N$_2$	Film Thickness (nm)	Deposited Stress (MPa)	Anneal Temp. (°C)	Anneal Time (hours)	Final Stress (MPa)
A	40	5	40	960±50	-740±40	N/A	N/A	-740±40
B1	20	5	40	1070±70	-660±40	N/A	N/A	-660±40
B2	20	5	40	1130±50	-660±40	400	1	-430±40
B3	20	5	40	1070±50	-660±30	500	1	-230±30
B4	20	5	40	1050±70	-650±30	600	1	80±80
B5	20	5	40	1070±70	-650±60	700	1	490±80
C	5	5	40	1210±70	-590±20	N/A	N/A	-590±20
D	5	10	40	1400±80	-430±10	N/A	N/A	-430±10
E	3	12	40	1230±70	-380±20	N/A	N/A	-380±20
F	5	5	40	200±20	-510±50	500	1	-40±60
G	40	5	40	210±20	-610±60	500	1	30±40
H	20	5	40	60±1	-800±200	500	2.5	80
I	20	5	40	62±1	-700±200	500	8	220

ray photoelectron spectroscopy (XPS) to determine the elemental composition of films A, B1, C, D, and E after deposition. Films were sputter-etched with an Ar$^+$ plasma *in-situ* prior to XPS scanning to remove the native surface oxide on SiCN. Young's modulus and hardness values were obtained through nanoindentation using a Hysitron Triboindenter. A Varian FTS-7000 Fourier transform infrared spectrometer (FT-IR) was used to perform transmission spectroscopy to determine the relative hydrogen content and hydrogen bonding in films B1-B5 after annealing. Film thickness was assessed on samples A-G using a Filmetrics F50 film thickness mapping system, and for samples H and I using a Digital Instruments Dimension 3100 atomic force microscope operated in tapping mode with BS-Tap300AL aluminum coated AFM cantilevers. A Trion Phantom II reactive ion etcher was used to test the resistance of SiCN films to a standard silicon etch recipe, and x-ray diffraction (XRD) was performed with a Bruker D8 Discover diffractometer using a GADDS area detector and a copper K-α radiation source, to determine the degree of crystallinity in the films.

	Gas Flow Ratio				
Sample	NH₃:DES	**Si**	**C**	**N**	**O**
A	8:1	38%	25%	35%	2%
B1	4:1	25%	31%	29%	14%
C	1:1	37%	31%	28%	4%
D	1:2	9%	56%	28%	7%
E	1:4	12%	58%	23%	7%

Table 2.2: Film Composition from XPS

2.4 Results

X-ray photoelectron spectroscopy was used to assess the elemental content of the films as a function of gas flow ratio, NH_3:DES, as shown in Table 2.2. As stated earlier, a main objective of this project was to attain some control over the film stress. While the stress could not be reduced to zero using flow ratio modulation alone, it could be tuned from $\sigma =$ -740 MPa in sample A to $\sigma =$ -380 MPa in sample E ("-" sign denotes compressive stress, Table 2.1), albeit with having great effect on the mechanical properties of the film. Figure 2.2 and 2.3 respectively depict the Young's modulus and hardness of the deposited films as a function of their carbon-to-nitrogen (C:N) content ratio.

Films deposited using a higher NH_3:DES ratio contained a lower C:N content ratio and exhibited higher Young's modulus and hardness. On the other hand, films deposited using a NH_3:DES lower than 1:1 contain more than 50 at% carbon and approximately 10 at% silicon. These results are expected, as lower NH_3:DES ratios provide less nitrogen and more carbon available to be incorporated into the film [65]. However, it should be noted that both Si-C and C-N bonds usually induce high hardness and Young's moduli, as in silicon carbide or carbon nitride [66,67]. Yet here the hardness and modulus both decrease as the carbon content in the film increases. It can be inferred from these results that the carbon is not bonded to the silicon or nitrogen in any useful way, and rather remains in the bulk of the film as an impurity. Attempts to explore further explore the nature of carbon in the film (XPS, FT-IR, Raman) proved inconclusive. All films were reported 100% amorphous by XRD.

Annealing of the material enabled the reduction and tunability of its residual stress from the compressive ($\sigma =$ -660 MPa) to the tensile ($\sigma =$ 490 MPa) range (figure 2.4).
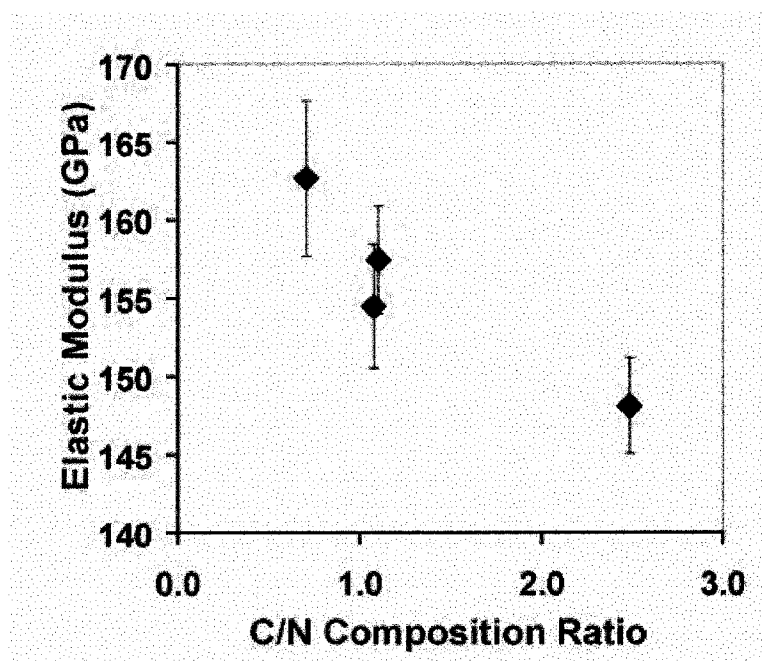
Figure 2.2: Young's modulus versus the carbon/nitrogen ratio in the films. Each data point is composed of multiple indentation measurements, with the error bars showing the standard deviation.
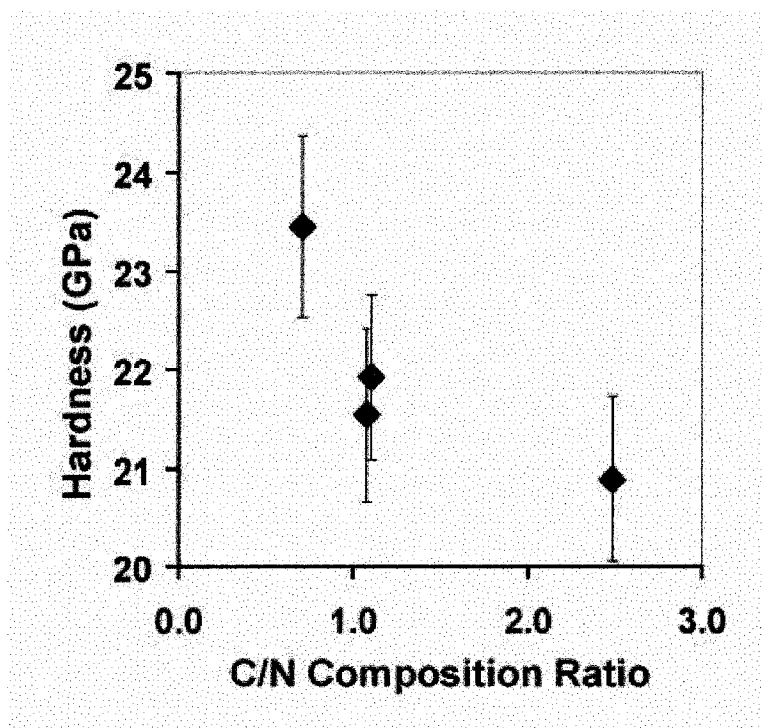

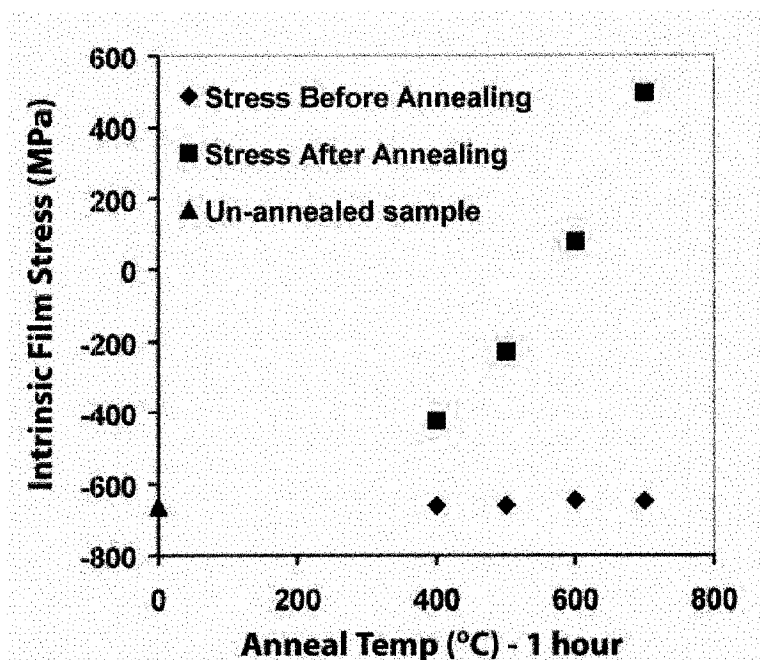Figure 2.3: Hardness versus the carbon/nitrogen ratio in the films.

Figure 2.4: The intrinsic stress before and after annealing at various temperatures. At higher temperatures the stress becomes tensile instead of compressive.

Infrared spectroscopy revealed that a reduction in incorporated hydrogen accompanied these stress changes induced by annealing (figure 2.5), suggesting that the compressive stress in the as-deposited films is related to bound hydrogen. The decrease in hydrogen-content with increasing temperature is concluded from observing the decrease of the N-H bending (single-hydrogen) and stretching FT-IR signals at 1150 cm^{-1} and 3350 cm^{-1}, respectively [68–71].

Annealing would release this hydrogen from its bound state [72,73], allowing the N and Si atoms previously bound to H atoms to bond with each other, and thus progressively lead to tensile stress [74]. These observations are consistent with stress trends in the Si_xN_y, as both stoichiometric and Si-rich low pressure chemical vapor deposition nitrides contain no hydrogen and are typically under tensile stress [63,75]. This also implies that the films deposited at low NH_3:DES flow ratios experienced lower compressive stress because there were simply less N-H bonds available in the precursor gases, thus were less present in the film. Further evidence of the effect of hydrogen-content on SiCN thin films is given in figures 2.6 and 2.7 illustrating the elastic modulus and hardness responding to the anneal temperature.
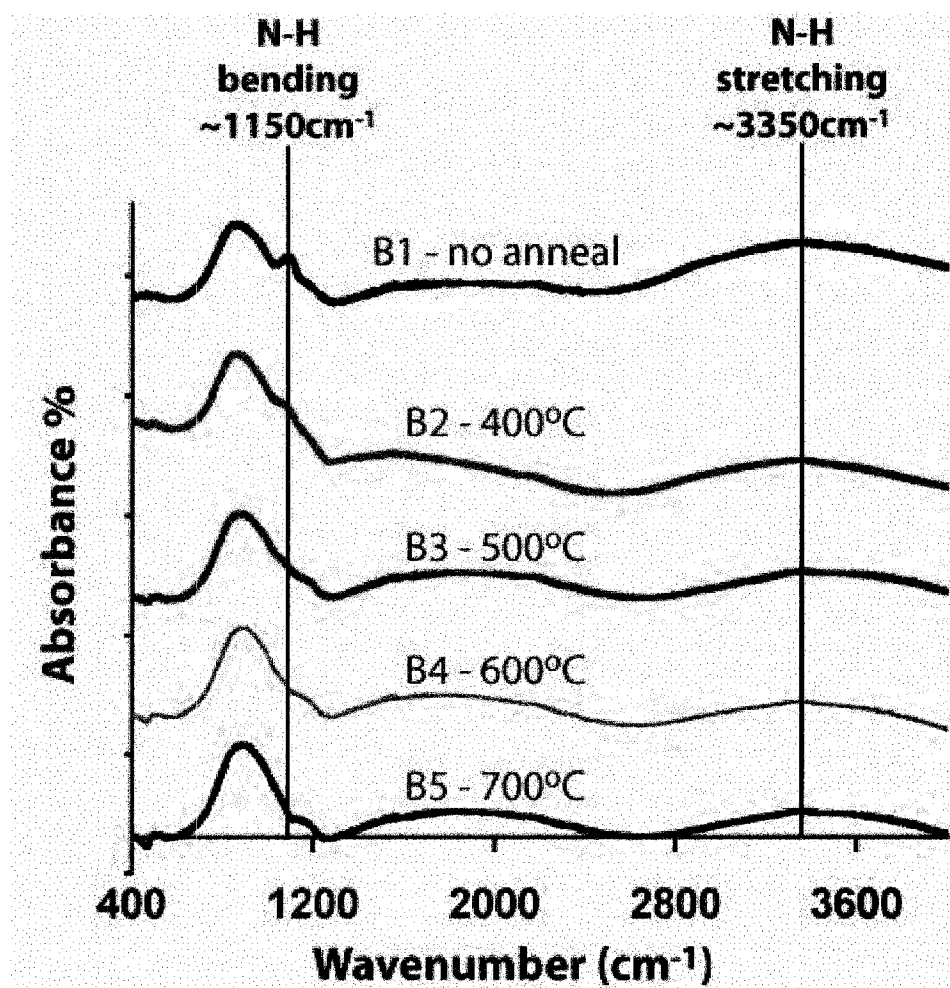
Figure 2.5: FT-IR spectra of SiCN films after annealing at various temperatures. Note the decrease in the two peaks related to N-H bonding.
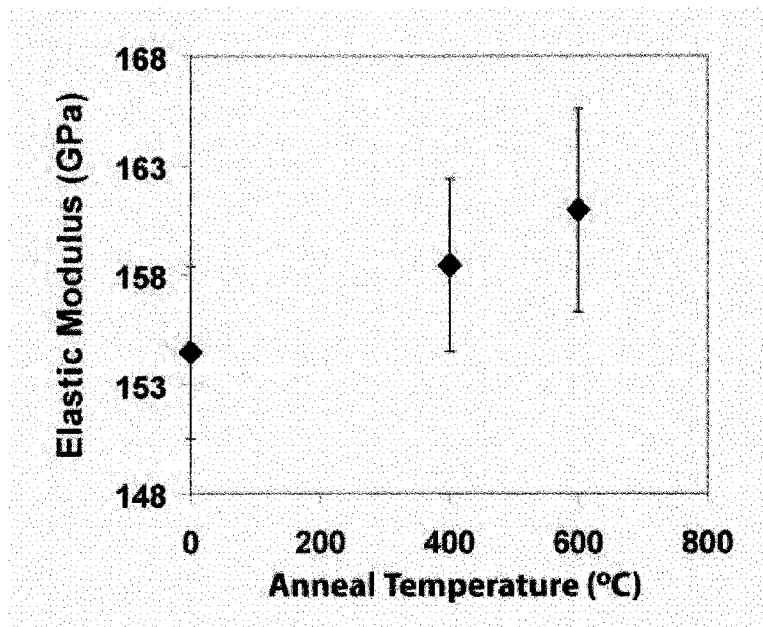
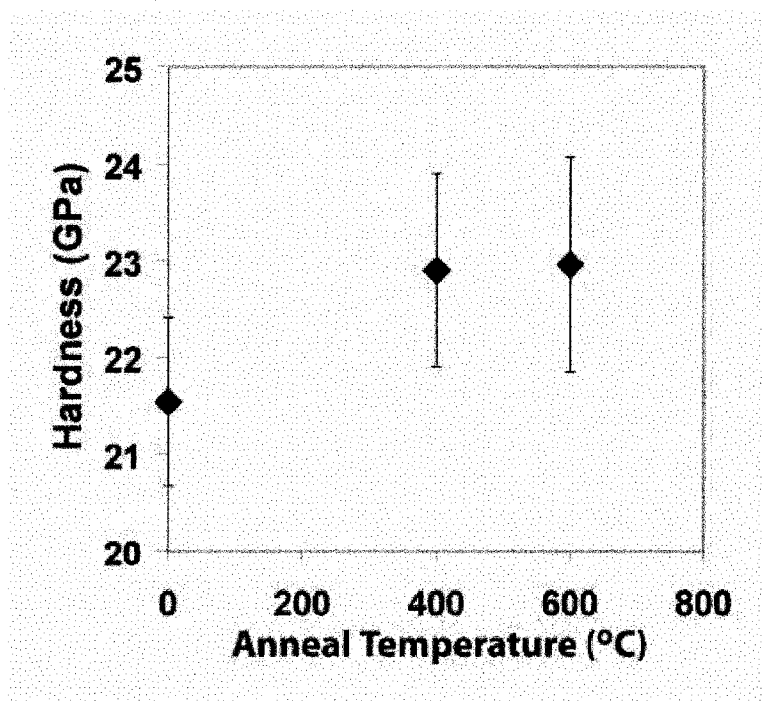Figure 2.6: Young's modulus in the annealed films.

Figure 2.7: Hardness in the annealed films.

These results indirectly imply that hydrogen incorporated into the SiCN amorphous network is responsible for the decrease in the values of both elastic modulus and hardness. This can be explained by the fact that hydrogen atoms have a coordination number of one, meaning each hydrogen atom is bound to only one atom and is not part of a network. Therefore, unlike the surrounding Si-Si or Si-N bonds in the film, the Si-H and N-H bonds do not contribute to the rigidity of the network, and instead only decrease the total number of other bond-configurations, thus leading to an overall decrease in the rigidity of the SiCN film. This concept is described in similar studies performed on amorphous hydrogenated silicon thin films (a-Si:H) [76, 77] where the effect of H-content on various mechanical properties was explored with similar findings.

It has been noted throughout the early stages of this project that film samples D and E were much more difficult to etch by RIE. Fluorine-based etch chemistries employing carbon-tetrafluoride (CF_4) or sulfur hexafluoride (SF_6) and oxygen (O_2) etched samples D and E at approximately half the rate of the other samples. It is well known that carbon is quite etch resistant to most chemistries [78], with the exception of atomic hydrogen [79]. One final note on the material investigation is that SiCN films annealed at 700 °C or above experienced cracking of the film, followed by the film peeling and flaking off of the substrate. This is because, at temperatures greater than 700 °C, the difference in thermal expansion between the silicon and the SiCN becomes too large, causing the SiCN to crack along the crystal planes of the silicon substrate.

2.5 Conclusion

The plasma-enhanced chemical vapor deposition of silicon carbonitride has been investigated. A large degree of control over the composition, as well as a moderate degree of control over the intrinsic stress in the SiCN films is possible through modulation of the NH_3:DES gas flow ratio. The Young's modulus and hardness of the films were affected as a result of this change in composition, due to the incorporated carbon not being included in the Si-N amorphous network. Post-deposition annealing was found to shift the intrinsic stress from compressive to tensile, and slightly improve the Young's modulus and hardness. Both the stress change and nanoindentation results were deemed to be a

result of the expulsion of hydrogen from the film during the annealing process. Nitrogen-hydrogen bonds are known to be responsible for compressive stress, as found in the cited literature, and thus removal of the hydrogen frees a bonding site on the nitrogen atom, allowing for the formation of the more tensile Si-N bond. An increase in stiffness was also observed due to the removal of bonded hydrogen, allowing for the formation of Si-N bonds which contributed to the rigidity of the amorphous network. Once control over the stress and composition of PECVD SiCN had been attained the project focus shifted to the development of nanomachining protocol for NEMS resonant structures and the investigation of the resonant behavior of this material.

Nanomachining and Nanomechanics

Control over the stress and composition was established in the previous chapter. On the journey to create a mass-sensing resonator device, the next step is to examine the resonant behavior of the material. This chapter explores the nanomachining processes used to create resonating structures, as well as establishes the effect of composition and stress on resonator behavior.

3.1 Introduction

Process development is a major area of research [14, 80–92]. Separate from the material development and device design fields, process development deals with simply fabricating any given desired structure. New techniques or methods can result in the fabrication of devices that previously could not be created [90–92]. In other cases researchers wish to apply batch fabrication techniques to processing in an attempt to commercialize devices [14, 82]. For example, there has been particular interest in extending the creation of high aspect-ratio structures to batch processing [81, 85, 88]. One of the virtues of MEMS is that their small, integrated nature allows for batch fabrication, reducing costs of large volume production, thus giving them an advantage over their discrete counterparts. Process

24

development and optimization is the drive to further enhance this virtue of MEMS, and naturally plays just as pivotal a role in the future of NEMS.

The ultimate goal of this project is the development of a biological mass-detection platform using nano-scale resonating structures. In order to achieve this, the structures in question must be designed and fabricated such that they withstand their intended use. First, singly-clamped (*cantilevers*) or doubly-clamped beams (*bridges*) must be produced successfully. Next, the behavior of these resonators must then be examined. PECVD SiCN is a completely unexplored material in the NEMS field, thus its behavior must be observed and controlled in order to construct the highest-quality resonators possible. Cantilevers are fabricated to examine the effect of composition changes on resonant behavior, while bridges allow the observation of stress on resonance quality.

3.2 Fabrication Methodologies

There are two key methodologies for fabricating three-dimensional mechanical structures [21]. *Bulk micromachining* is an etch-based fabrication scheme where the silicon substrate itself is fashioned into the mechanical elements and often employs the attachment, or bonding, of two or more wafers together to create a finished device. *Surface micromachining*, on the other hand, is deposition-based. Instead of machining the bulk silicon substrate, thin films of a given material are deposited onto the substrate surface. These materials are then patterned and selectively etched to produce free-standing microstructures. Since the main focus of this project is on simple resonating structures, process flows by which to fabricate this structure will be used to illustrate the difference between these two fabrication methodologies. This section assumes the reader has an understanding of basic processes such as deposition, photolithography, and wet and dry etching. Explanations of basic processes can be found in [3,93].

3.2.1 Bulk Micromachining

Figure 3.1 depicts the bulk-micromachining process for a silicon cantilever. Step 1 involves the pattern definition in an etch resistant polymer, or *resist*, where the outline of the cantilever is patterned. Step 2 uses a reactive ion etch to create a trench around the

STEP 1 — resisit / Si — PATTERN DEFINITION FRONT SIDE

STEP 2 — Si — ANISOTROPIC Si ETCH & RESIST REMOVAL

STEP 3 — SiO₂ — PECVD SiO₂ DEPOSITION

STEP 4 — resisit — PATTERN & ETCH OF BACKSIDE SiO₂

STEP 5 — RESIST REMOVAL & ETCH OF Si

STEP 6 — SiO₂ REMOVAL USING HF ACID

FINISHED STRUCTURE
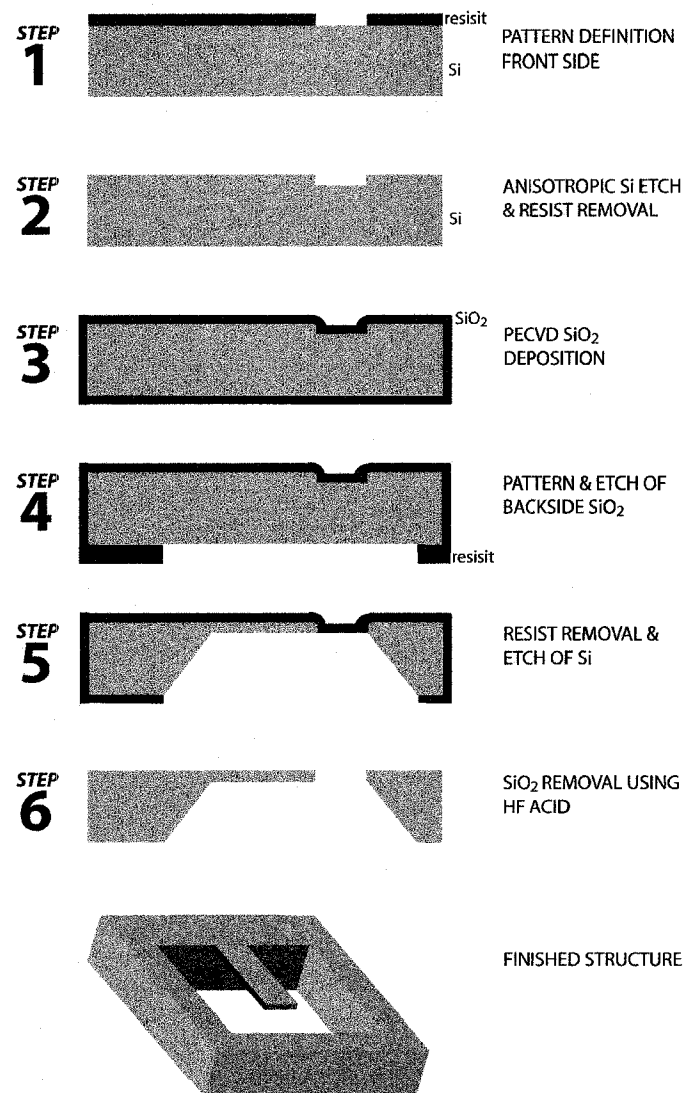
Figure 3.1: Bulk micromachining process flow

cantilever to the desired depth that will determine the cantilever thickness. The resist is removed in an organic solvent following etching. Silicon dioxide, which is resistant to potassium hydroxide (KOH) [78], is deposited via PECVD everywhere on the wafer in step 3 to prevent unwanted etching in subsequent steps. Similar to steps 1 and 2, step 4 shows the SiO2 on the wafer backside being patterned with resist and etched to allow KOH to remove the silicon substrate. In step 5 the silicon is etched through to the trenches defined in step 2. Typically an implanted dopant layer is used to create an etch-stop by making the top layer of silicon resistant to KOH, thus defining the thickness of the cantilever. Finally,

in step 6, the SiO_2 is removed in a hydrofluoric acid bath, leaving the free-standing silicon cantilever in the substrate.

3.2.2 Surface Micromachining
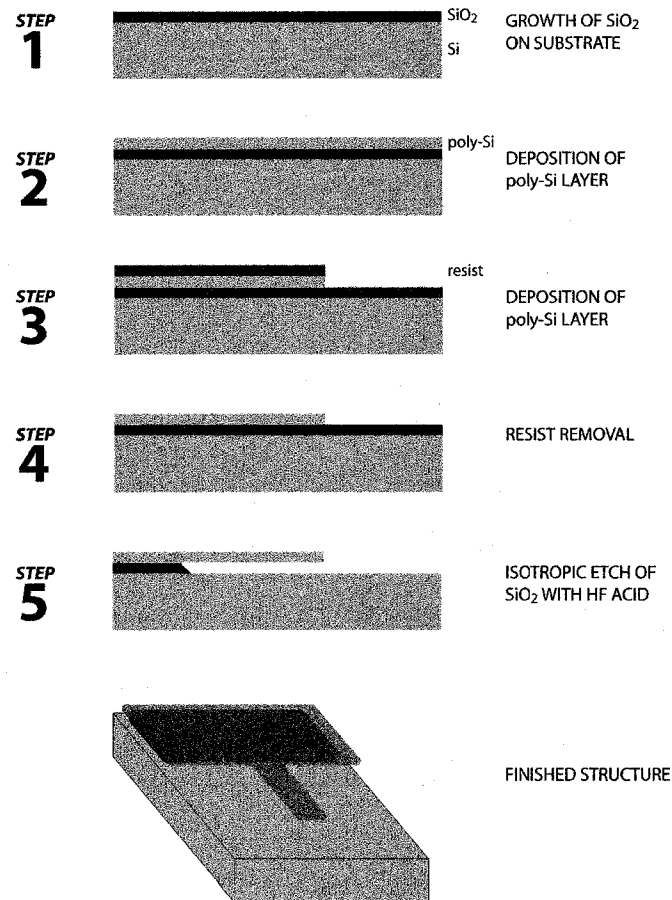
Figure 3.2: Surface micromachining process flow.

Figure 3.2 depicts the surface-micromachining process for a silicon cantilever. A layer of sacrificial silicon dioxide is formed in step 1, upon which the device layer will be formed. In step 2 a device layer of polycrystalline silicon, or *poly-Si*, is deposited via LPCVD onto the SiO_2. Step 3 shows the poly-Si layer patterned with resist, then etched using a reactive ion method. Step 4 depicts the near-finished device with the resist removed. In step 5, an isotropic wet-etch of the silicon dioxide layer is performed to release the poly-Si, thus creating a free-standing cantilever. It should be noted that because of the relatively small gap between the cantilever and the silicon substrate surface, surface tension forces of the

liquid can cause devices to stick to the surface, and thus specific liquid-removal techniques must be used (see next section).

3.3 Stiction

As described above, surface micromachining usually involves the removal of a sacrificial layer between two other layers. In the case of the surface-micromachined cantilever, this sacrificial layer is the silicon dioxide layer present between the poly-silicon device layer and the silicon substrate. A liquid etchant is used to dissolve the SiO_2, and in doing so the liquid will slowly occupy the space where the SiO_2 once was, thus there exists an interfacial force between the liquid and each of the surfaces (figure 3.3a).
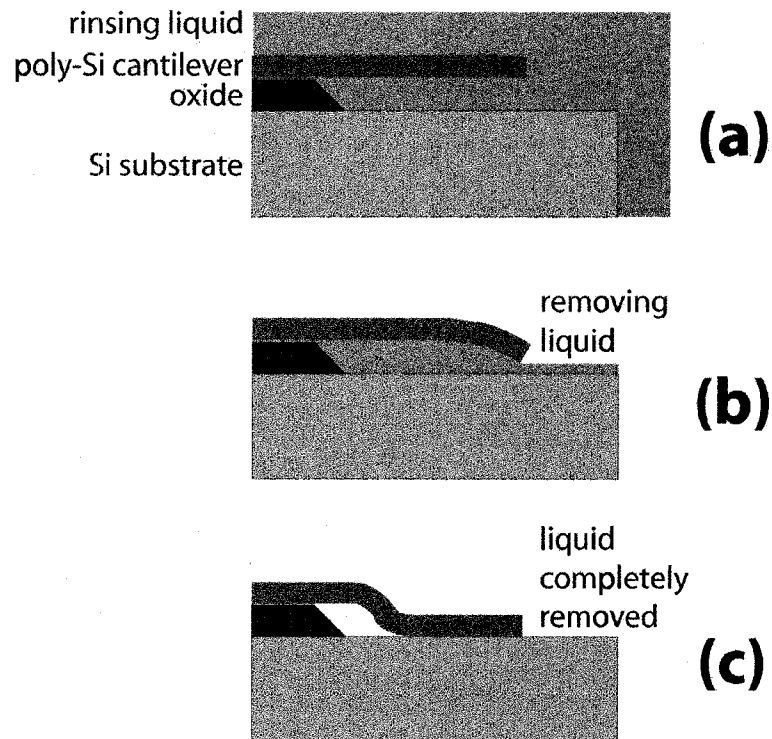
Figure 3.3: The process of stiction: (a) the rinsing liquid covers all surfaces, then as the liquid is removed (b) the structure is pulled toward the substrate surface. Finally, liquid is removed, (c), and the structure is in contact with the substrate.

This *capillary force* is known be inversely proportional to the gap distance between the upper and lower surface [94]. As the liquid is removed, the cantilever is pulled downwards, decreasing the gap distance and increasing the capillary force, in turn pulling the cantilever

downward even further (figure 3.3b). The end result of this loop is that once all liquid has been removed the cantilever may make physical contact with the substrate surface (figure 3.3c). This contact forms an irreversible bond, which holds the cantilever to the substrate, the strength of which has been attributed to hydrogen bonding [3], van der Waals forces [95], and electrostatic forces [94, 96]. Stiction is a major problem, not only in cantilever structures, but also in more elaborate devices where points of sliding contact are essential to device operation can be affected [96, 97]. However, it is possible to overcome stiction using a variety of techniques. Supercritical drying, or critical process drying, can be used to remove the liquid in the gap without forming a meniscus and therefore avoiding capillary forces [98]. Freeze drying freezes the liquid and removes it via sublimation, again avoiding capillary forces and stiction [3]. Device design can also be used to minimize damage due to stiction, such as implementing a rigid supporting top-plate to prevent cantilever collapse [99] or controlling the gap underneath a pressure-sensing diaphragm to ensure its survival [100].

3.4 Theory of Vibration

For any spring-mass system, neglecting damping, the (angular) resonant frequency ω can be described by equation 3.1:

$$\omega = \sqrt{\frac{k}{m}} \tag{3.1}$$

where k is the spring constant of the system and m is the effective mass (as stated in Chapter 1). For a beam with a Young's modulus E and moment of inertial I, both of which are invariant along the length of the beam (x-direction), the vertical displacement of the beam, u under an applied transverse load q, if u assumed to be much less than the beam length L of the beam, can be described by the Euler-Bernoulli equation [2]:

$$EI\frac{d^4u}{dx^4} - (\sigma_o wt)\frac{d^2u}{dx^2} = q \tag{3.2}$$

which neglects damping effects. In a cantilever clamped at only one end, the axial stress σ_o is zero, and the equation becomes:

$$EI\frac{d^4u}{dx^4} = q \tag{3.3}$$

Now assume a polynomial solution to $u(x) = A + Bx + Cx^2 + Dx^3 + Fx^4$, and set the boundary conditions as follows:

$$u(0) = 0 \tag{3.4}$$

$$\frac{du}{dx}(0) = 0 \tag{3.5}$$

$$\frac{d^2u}{dx^2}(L) = 0 \tag{3.6}$$

$$\frac{d^3u}{dx^3}(L) = 0 \tag{3.7}$$

Equations 3.4 and 3.5 state that the displacement and slope, respectively, of the beam at the clamping point are both zero. Equation 3.6 implies an infinite radius of curvature, r, at the unclamped end of the beam, or rather $r^{-1} = 0$. Lastly, equation 3.7 implies a shear stress of zero at the free end of the beam, since it is not connected to anything. Solving the equation, the first two boundary conditions set $A = B = 0$, and the rest of the coefficients are found to be:

$$C = \frac{qL^2}{4EI} \tag{3.8}$$

$$D = -\frac{qL}{6EI} \tag{3.9}$$

$$F = \frac{q}{24EI} \tag{3.10}$$

The effective spring constant k of the cantilever can be found by substituting the expression for the maximum displacement of the cantilever u_{max} into $F = kx$, where here x is the displacement in the direction of k and F is qL. Thus, for a cantilever, the spring constant is:

$$k_{cantilever} = \frac{8EI}{L^3} \tag{3.11}$$

and substituting into equation 3.1 and using the value of I for a beam of rectangular cross section [2, 101], the fundamental resonant frequency of the cantilever is:

$$\omega = \frac{t}{L^2}\sqrt{\frac{2}{3}}\sqrt{\frac{E}{\rho}} \tag{3.12}$$

with a L^{-2} dependency on frequency.

A doubly-clamped beam, or *bridge*, can also be described by equation 3.2. Assuming negligible axial stress (dealt with later) leads to equation 3.3 as for the cantilever. However the boundary conditions applied are different:

$$u(0) = 0 \tag{3.13}$$

$$\frac{du}{dx}(0) = 0 \tag{3.14}$$

$$u(L) = 0 \tag{3.15}$$

$$\frac{du}{dx}(L) = 0 \tag{3.16}$$

Here equations 3.13 and 3.15 specify zero deflection at both clamping points, while equations 3.14 and 3.16 state the slope of the beam is zero at the clamping points. Assuming a polynomial solution to $u(x)$ of the form $A + Bx + Cx^2 + Dx^3 + Fx^4$, the first two coefficients are set to zero by the boundary conditions in equations 3.13 and 3.14. Solving and substituting yields the remaining 3 coefficients:

$$C = \frac{qL^2}{24EI} \tag{3.17}$$

$$D = -\frac{qL}{12EI} \tag{3.18}$$

$$F = \frac{q}{24EI} \qquad (3.19)$$

For a bridge, the maximum deflection occurs at $x = L/2$, so along with the found coefficients and substituting for I, the maximum beam deflection is:

$$u_{max} = \frac{qL^4}{32Ewt^3} \qquad (3.20)$$

and the spring constant for a bridge, neglecting stress, is:

$$k_{zerostress} = \frac{32Ewt^3}{L^3} \qquad (3.21)$$

Thus, substituting into equation 3.1, we get a resonant frequency of the bridge described by equation 3.22:

$$\omega = \sqrt{32} \frac{t^2}{L^2} \sqrt{\frac{E}{\rho}} \qquad (3.22)$$

Note that the bridge, in the absence of stress, also exhibits a L^{-2} dependence on frequency. Now consider the case where the axial stress σ is sufficiently large such that it dominates the behavior of the system. In this case, the Euler-Bernoulli beam equation becomes:

$$- \sigma_o wt \frac{d^2u}{dx^2} = q \qquad (3.23)$$

The same boundary conditions and trial solution employed for a stress-free bridge can be applied here. For appearance the $\sigma_o wt$ term is written as N. From the differential equation we find C to be:

$$C = -\frac{q}{2N} \qquad (3.24)$$

with the other terms becoming more complex:

$$D = \frac{q}{2N} \frac{3L^2}{4L^3 - 3L^2} \qquad (3.25)$$

$$F = \frac{q}{2N} \frac{L - 3}{4L^3 - 3L^2} \qquad (3.26)$$

Substituting back into the equation for $u(x)$ to find the maximum deflection, and neglecting all but the highest-order-terms (for illustration purposes) we find:

$$u_{max} = \frac{11}{32}\frac{qL^2}{N}$$ (3.27)

and the spring constant for a stress-dominated bridge is:

$$k_{stress} = \frac{32}{11}\frac{\sigma_o wt}{L}$$ (3.28)

Finally, substituting into equation 3.1, we find the dependence of frequency on length L and stress σ_o as:

$$\omega \approx \frac{1}{L}\sqrt{\frac{\sigma_o}{\rho}}$$ (3.29)

So in the presence of negligible axial stress σ_o, the resonant frequency of a bridge is proportional to L^{-2}, while in a stress-dominated beam the dependence goes as $f \propto L^{-1}$.

These results will be discussed further later in this chapter. A rigorous derivation of the Euler-Bernoulli beam equation, including analytical solutions and damping effects can be found elsewhere [2, 102]

3.5 Experiment

The first generation of devices was designed to examine the effect of changing composition and stress using film samples F/G and H/I respectively (Table 2.1). These samples were then annealed in a Minibrute 3-zone tube furnace for the amount of time specified in Table 2.1, with stress measurements again done using the KLA-Tencor 2320 Flexus thin film stress measurement system. These films were then cleaned again in Pirinha-mixture and treated with buffered oxide etch (BOE, 10:1 ammonium fluoride:hydrofluoric acid) in preparation for patterning. A bilayer of polymethyl methacrylate (PMMA) 950/495 (polymer chain length) was spin-coated onto 1×1 cm^2 chips of films F - I. The resist bilayers were exposed in a Raith150 electron beam lithography system using a 20 μm aperture, an acceleration voltage of 10 kV, and an area dose of 120 μC/cm^2. A three-step bath consisting of a solution of 1:3 methyl-isobutyl-ketone: isopropanol (30 seconds),

pure isopropanol (15 seconds), and water (15 seconds) was used to develop the exposed PMMA layers. An electron beam evaporator was then used to deposit a 30 nm chromium (Cr) etch mask, followed by lift-off in a 5 minute sonic acetone bath. A Trion Technology Phantom II RIE was used to anisotropically etch the Cr-patterned-SiCN in a 4:1 sulfur hexafluoride: oxygen ($SF_6:O_2$) plasma recipe adapted from literature [103]. 1G structures were previously etched using the Nanofab standard silicon nitride RIE with a 9:1 carbon tetrafluoride: oxygen ($CF_4:O_2$) plasma, but due to a moderate undercutting of the Cr mask into the SiCN, another etch recipe was developed to produce sub-micron width bridges (etch parameters shown in table 3.1).

Table 3.1: Trion RIE Machine Parameters for Two Etch Recipes

	Standard SiN RIE	Adapted RIE (from [103])
CF_4 Flow Rate (sccm)	45	-
SF_6 Flow Rate (sccm)	-	42
O_2 Flow Rate (sccm)	5	12
RF Power (W)	125	95
Pressure (mTorr)	150	25

Once the structures were etched into the SiCN layer, the Cr mask was removed using a standard wet-chemical Cr-etch. The first generation (*1G*) structures were released by isotropically etching the sacrificial SiO_2 layer underneath the SiCN in a BOE bath (room temperature) for 14 minutes, followed by a 3-bath rinse in de-ionized (DI) water. It had been found through previous experiments that the bridges will stick to the Si substrate surface if the structures are dried using only a nitrogen-gun, or if left to dry by themselves. Thus, following the water bath, the chips were put in isopropanol, then subjected to a supercritical drying process in a Tousimis Autosamdri 815B critical process drier. This machine bathes the chip in liquid carbon dioxide (CO_2), then adjusts the pressure and temperature of the chamber to remove the CO_2 without forming a meniscus, thus eliminating the effect of surface forces and stiction.

An established interferometric technique, seen in figure 3.4, was used to assay the resonant frequencies of the first generation cantilevers and bridges [104]. For this purpose, the samples were affixed to a piezoelectric stage mounted inside a vacuum chamber which was pumped to $\sim 10^{-3}$ Torr. The piezoelectric element is then actuated by the tracking
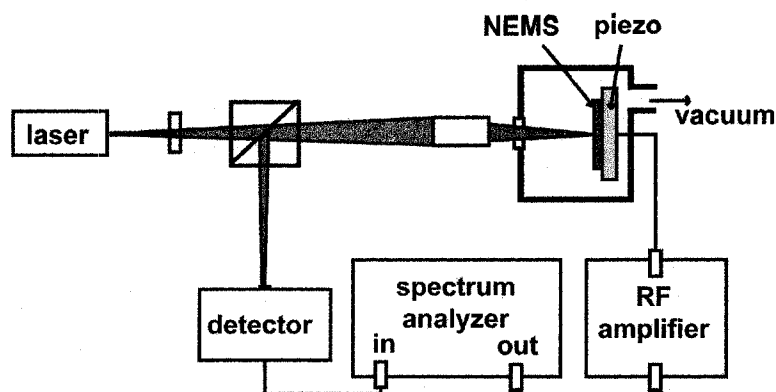
Figure 3.4: The interferometry-based resonance-assaying setup, described in [104], used to measure the frequency of the cantilevers and bridges.

output of a Hewlett-Packard ESA-L1500A spectrum analyzer. A He-Ne laser ($\lambda = 633$ nm) is focused to a beam spot of 5 μm in diameter using a 0.35 numerical aperture microscope objective. When actuated at resonance, relative motion of the structure with respect to the underlying substrate modulates the reflected signal through interferometric effects. The modulated signal is reflected back through the microscope objective. A beam splitter is then employed to divert the reflected signal towards a New Focus 1601 ac coupled photodetector, whose output is fed to the input of the spectrum analyzer. Electron microscopy of the fabricated devices was performed following resonance measurements in a Hitachi S-4800 cold field emission scanning electron microscope (FE-SEM).

3.6 Results

In the 1G structures (figures 3.6 and 3.8), the gap between the SiCN bridge and the Si-substrate was approximately 500 nm. The length of cantilevers ranges from $L = 2$ μm to 6.5 μm, while the bridges vary in length from $L = 4$ μm to 20 μm. Without critical point drying, all structures over 4 μm in length were bound to the Si-substrate surface by stiction. Even when the supercritical drying process was used, 100% device yield was not reliably attainable. The most suitable method for eliminating stiction in these structures is to increase the gap distance between the SiCN and the Si. In the surface micromachining process of the first generation devices, this could be done by increasing the thickness of the sacrificial silicon dioxide layer between the SiCN and Si. This would mean that if a

3 μm gap was desired, a 3 μm oxide would have to be deposited. This would also mean that the clamping point of the cantilever or bridge would be undercut by 3 μm because the etchant used (BOE) removes the SiO_2 isotropically. This undercut would effectively increase the total length of the beams, which would somewhat counteract the anti-stiction effect of the larger gap. Additionally, this would leave a large portion of the anchoring structure undercut and free to resonate with the cantilever or bridge. This would result in the resonators having only a moderately large thin SiCN "flap" as an anchor, effectively attaching the resonating beam to another larger beam. It was predicted that having a non-rigid clamping point would have an adverse effect on the resonant behavior of the structures. Vignola *et al.* proposed that large undercutting of resonator supports is the determining factor of resonance quality [105], later demonstrated my Verbridge *et al.* [106], while Photiadis *et al.* have shown that having a substantially thick anchor base (equivalent to having very little undercut) directly improves the quality [107]. These issues will be addressed in chapter 5 during discussion of the fabrication of second generation bridges.
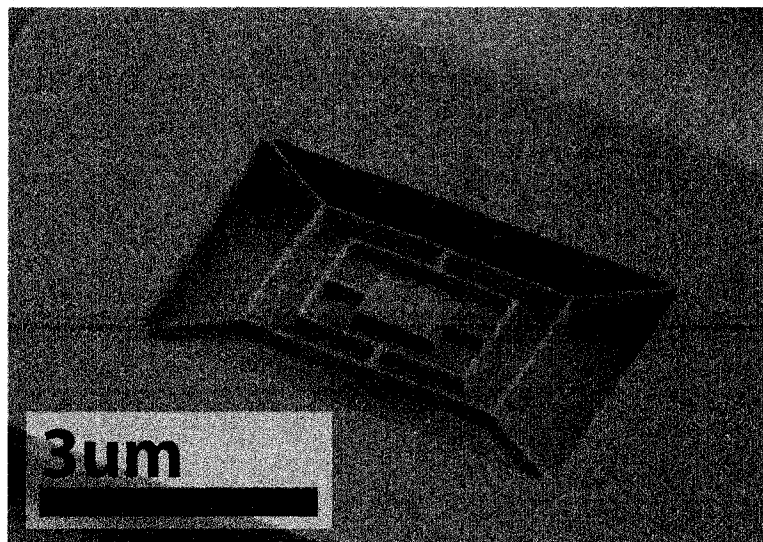
Figure 3.5: This surface machined structure consists of support beams 120 nm-wide which are suspending a 1 μm^2 paddle. This picture was featured in the month of October in the Raith 2006 Calendar.

Concurrent to resonator fabrication, more complicated structures were produced to investigate the degree to which SiCN can be reliably machined. The standard recommended Raith150 electron-beam doses were sufficient for this nanomachining, and thus no further

development was required on this front. The suspension structure in figure 3.5 was patterned, etched, and successfully released, demonstrating quite a degree of intricacy afforded by both the Raith150 machine, as well as the durability of the material. In fact, this picture was featured in the 2006 Raith calendar. Note in figure 3.5 the vertical sidewalls on the SiCN layer, a result of the $SF_6:O_2$ recipe developed.

Cantilever and bridge structures were machined in order to assess the mechanical properties of the material and to investigate its applicability for resonant nanomechanical biosensors. First, cantilevers of thickness $t = 200$ nm, width $w = 1$ μm, and lengths varying from $L = 2$ to 6.5 μm were fabricated in films F (1:1 $NH_3:DES$) and G (8:1) (figure 3.6).
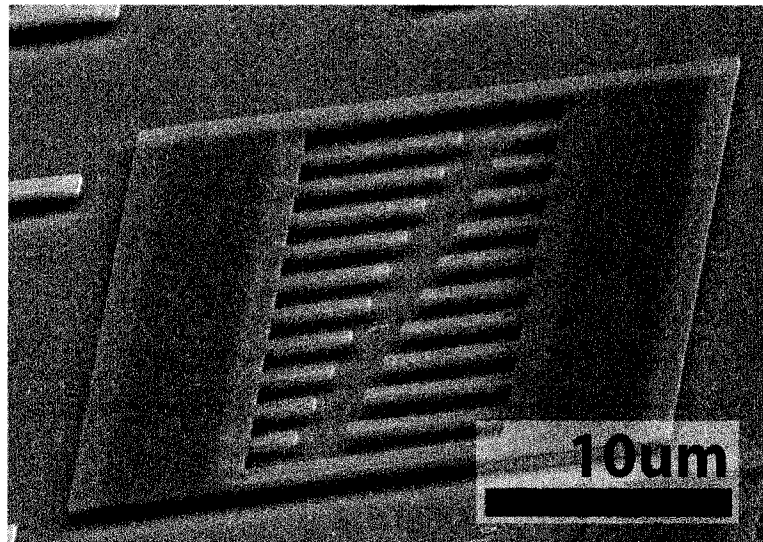
Figure 3.6: Surface micromachined cantilevers. The SiCN layer is 200 nm-thick, with the cantilevers themselves being 1 μm-wide and 2 to 6.5 μm-long, with the sacrificial oxide layer being 500 nm-thick.

An approximation of the fundamental resonant frequency of a cantilever beam with a rectangular cross section is described by equation 3.30 [108]:

$$f_o = \frac{t}{2\pi(0.98)(L+u)^2}\sqrt{\frac{E}{\rho}} \qquad (3.30)$$

where L is beam length, $u = 810$ nm is the length of the undercut (as measured by scanning electron microscopy), E is Young's modulus, and ρ is the density of the beam material. Figure 3.7 displays the results of the resonant assaying of this first set of devices.

200 nm thick cantilevers:
Frequency vs. Inverse-length squared
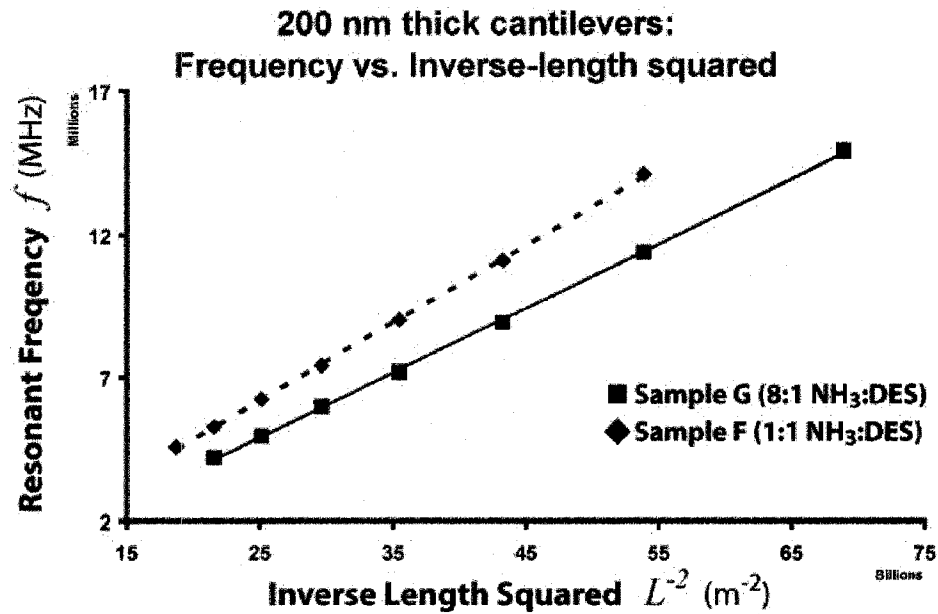
Figure 3.7: A logarithmic plot of the data obtained through resonance of the cantilevers.The speed of sound ($\sqrt{\frac{E}{\rho}}$) in the high-carbon film is found to be 8.35 × 10³ m/s, while a value of 6.20 × 10³ m/s is found in the low-carbon film.

Fitting the data to equation 3.30 gives root-modulus-over-density ratios of $\sqrt{\frac{E}{\rho}}$ = 8.35×10³ m/s for sample F and $\sqrt{\frac{E}{\rho}}$ = 6.95×10³ m/s for sample G. The result for sample F roughly agrees with previously reported values of $\sqrt{\frac{E}{\rho}}$ = 6.20×10³ m/s for a similar carbonitride material [64]. On the other hand, the result for sample G is comparable to the speed of sound in silicon of $\sqrt{\frac{E}{\rho}}$ = 8.45×10³ m/s. We note that the fabrication of singly clamped cantilevers allows the relaxation of the intrinsic stress at their neutral axis upon release of the devices. The absence of noticeable bending of the released cantilever suggests that the devices are not subjected to any significant stress gradient that could also affect their mechanical properties. The differing modulus-over-density ratios observed from material to material are therefore intrinsically related to variations in film composition, and not to the residual stress present as a result of those compositions. The analysis of bridges now allows studying of the effect of residual stress in the mechanical properties of the devices. Doubly clamped beams of thickness t = 50 nm, width w = 800 nm, and lengths varying from L = 4 to 20 μm were fabricated in materials H and I for such purpose (figure 3.8).
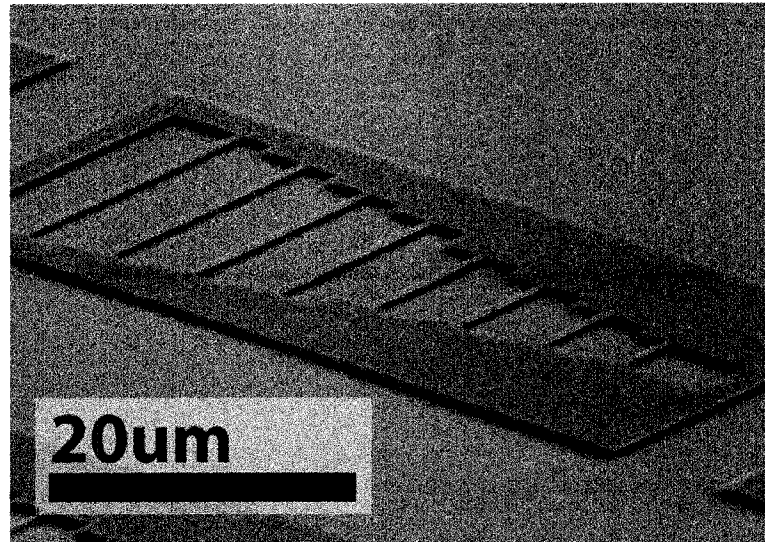
Figure 3.8: Surface micromachined bridges. The SiCN layer is 60 nm-thick, with the bridges themselves being 800 nm-wide and 4 to 20 μm-long, with the sacrificial oxide layer being 500 nm-thick.

The approximate resonant frequency for a doubly clamped beam of under tensile stress σ is given by equation 3.31 [102]:

$$f_o = 1.057t\sqrt{\frac{E}{\rho}(L+u)^{-2} + \sqrt{\frac{0.31\sigma}{\rho}}(L+u)^{-1}} \qquad (3.31)$$

where σ is the residual stress in the device, and $u = 530$ nm was the length of the undercut, as measured by scanning electron microscopy. Unstressed beams are therefore expected to exhibit a L^{-2} dependence on frequency f, while highly stressed beams are rather expected to progressively show a L^{-1} dependence. Figure 3.9 graphs the dependence of resonant frequency on length for beams fabricated in films H and I.

Films H and I initially possessed residual tensile stress values of σ = 80 MPa and σ = 220 MPa, respectively. A fit of data to equation 3.31 reveals a $L^{-0.935}$ dependence in the lower stress film (sample H) and a $L^{-0.999}$ dependence in the higher stress film (sample I), as would be expected. Additionally, the quality factor appears to be affected by the stress present in the beams. All of the frequency spectra captured for low-stress sample H had a quality factor ranging between 3000 and 5000, at frequencies between f = 6.1 MHz and f = 16 MHz, with a fQ product of 1.5×10^{10} s^{-1}. Low-stress samples similar to sample
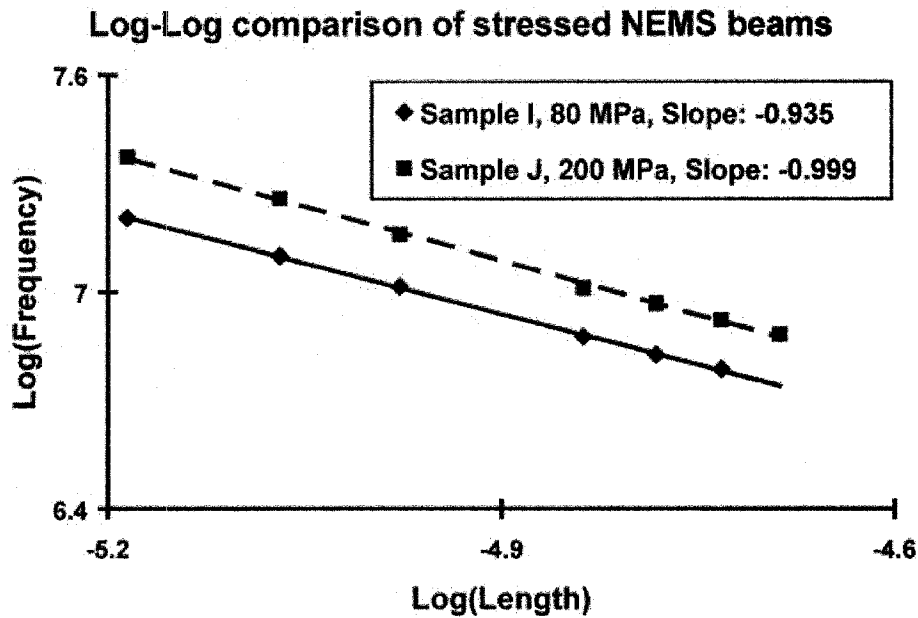
Log-Log comparison of stressed NEMS beams

Figure 3.9: A logarithmic plot of the data obtained through resonance of the bridges. The low stress sample (H) was found to exhibit a $L^{-0.935}$ dependence of frequency on length, while the high stress sample (I) was $L^{-0.999}$, completely dominated by stress.

H (not reported here) showed similar quality factor data. On the other hand, the beams in high-stress sample I experienced quality factors between 8000 and 23 000, at frequencies between f = 7.6 and 24 MHz, with fQ products as high as of $1.5 \times 10^{11} \text{ s}^{-1}$. The maximum Q factor obtained in sample I was 26 000, at f = 7.6 MHz, (fQ = $2 \times 10^{11} \text{ s}^{-1}$), exceeding the room temperature performance of Si devices across many dimensions [56, 109–111]. Indeed, silicon structures described as having very high Q (100 000) have traditionally been macroscopic in nature, with operating frequencies in the 1 - 100 kHz range, limiting their fQ product to the 10^9 - 10^{10} s^{-1} range [109–111]. On the other hand, silicon devices of dimensions similar to those presented here have been known to exhibit surface-mediated issues impairing their performance, limiting their fQ product to the mid-10^{10} s^{-1} range, even following extensive surface conditioning [56]. These effects have also been observed by Verbridge *et al.* [106, 112] where quality factors of over 200 000 were achieved using a wafer-bending technique to increase stress. One possible explanation for this was that the introduction of a marginal tensile stress improved energy confinement by mitigating mechanical coupling with the clamping points. Verbridge *et al.* note a dependence on

Q with the length of the clamping point undercut, and also note an increase in Q after applying tension to the beams [106]. He describes the effect as limiting energy transfer between the beam and clamping point by "increasing the acoustic impedance". It was also proposed that the Q in these resonators is dominated by thermoelastic dissipation (TED). Thermoelastic dissipation describes an irreversible flow of energy across the resonator due to a temperature gradient setup by the deflection of the beam creating areas of compression (warm) and tension (cool) [113, 114]. Consider that by putting the bridge under tension, the magnitude of this temperature gradient is reduced, due to the decreased magnitude of deflection and the difference in stress levels of the "compression" and "tension" areas. This, conceptually, would subsequently reduce the amount of energy lost, increasing Q. Figure 3.10 shows the quality factors for samples H and I plotted against their resonant frequencies, with a theoretical slope for the TED limited quality factor.

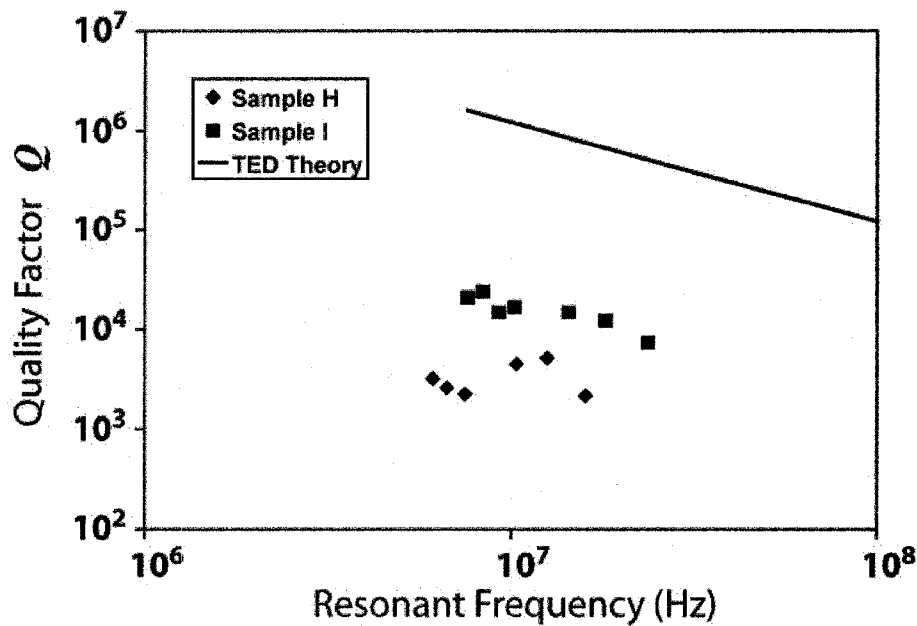Figure 3.10: Frequency versus Q for samples H and I, as well as the theoretical TED-limited quality factor slope calculated for these structure parameters.

The theoretical TED-limited quality factor plot is obtained from equation 3.32 [112]:

$$Q_{TED} = \frac{c_v}{E\alpha^2 T} \left(\frac{6}{\xi^2} - \frac{6}{\xi^3} \frac{sinh\xi + sin\xi}{cosh\xi + cos\xi} \right)^{-1} \qquad (3.32)$$

and

$$\xi = \sqrt{\frac{\omega \rho c}{2\kappa}} \qquad (3.33)$$

where the values of the equation parameters are:

c_v is the specific heat per volume, 710 J/m^{3}K [112]

T is the temperature of the beams, 300 K

ω is the angular resonant frequency

E is Young's modulus, 160 GPa as obtained from nanoindentation

α is the linear coefficient of thermal expansion, 1.5×10^{-6} K^{-1} [63]

ρ is the density, 1900 kg/m^3 [64]

c is the specific heat capacity, 0.4 J/gK [115]

κ is the thermal conductivity, 3.2 W/mK [112]

As seen in figure 3.10, both samples H and I are more that two orders of magnitude below the theoretical TED-limited quality factor. While the theoretical curve was based off of approximate parameters, all parameters are believed to be within an order of magnitude or less to their true values for PECVD SiCN. Additionally, varying any combination of the parameters within this range does not bring the TED-limit significantly closer to the experimental data than it is in the figure. Thus, the increase in quality factor is not due to limiting thermoelastic dissipation.

3.7 Conclusion

First generation devices, cantilevers and bridges created using the surface-micromachining sacrificial oxide technique, were subjected to interferometric assaying to determine the effect of composition and stress on resonant behavior. Through resonant characterization of cantilevers fabricated from samples F and G, these films were found to have root-modulus-to-density values ranging from $\sqrt{\frac{E}{\rho}} = 8.35 \times 10^3$ and $\sqrt{\frac{E}{\rho}} = 6.95 \times 10^3$ m/s for high and

low C:N ratios, respectively. Annealing was used to modulate the intrinsic film stress (as described last chapter) and create samples with low (sample H) and high (sample I) tensile stress. Bridges were fabricated from films with stresses of $\sigma = 80$ MPa and $\sigma = 200$ MPa to analyze its effect on resonant behavior. The length dependencies on resonant frequency were found to be $L^{-0.935}$ and $L^{-0.999}$, respectively, in agreement with the L^{-1} dependence expected in stressed structures. Resonant quality factors of 5000 were obtained for the low-stress film, while a maximum Q factor of 26 000 was obtained in the beams fabricated from the high-tensile-stress films. A stress-induced restriction of thermoelastic dissipation (TED) was proposed as a possible explanation for this increased quality factor, but the Q of the bridges was found to be several orders of magnitude from the TED-limit.

Stiction was a prevalent problem in this first generation of devices. This was attributed to the small gap between the beam and substrate. It was noted that this gap could not be sufficiently enlarged to resist stiction without having an adverse effect on resonance quality. Thus, bridges resistant to the effects of stiction must be fabricated using another method, which will be discussed in chapter 5.

4

Surface Chemistry

Chapter 2 described the optimization of film stress and composition. This led to an investigation of resonator behavior in chapter 3, where a process to create high-quality bridge resonators was developed. A strategy for specifically attaching the streptavidin protein to the SiCN resonator surface is formulated in this chapter. This strategy will eventually be required to use these resonators detect the protein mass in the following chapter.

4.1 Introduction

4.1.1 Surface Functionalization

Micromechanical sensors are affected by a wide variety of external stimuli [29, 30]. Heat can cause expansion or contraction of structures, and possible changes in material properties (i.e. density), chemical species can cause stress gradients and changes in spring constants, and adsorbed masses can cause a shift in the frequency of microresonators. It is because of this that these types of sensors are so versatile, as discussed in chapter 1. This versatility, combined with the ability to mass-produce complete sensor systems at a low-cost makes mircomechanical sensors the best choice for many applications. However, these

44

sensors are useless unless they are able to somehow determine what stimulus is causing the transducer to produce an output signal.

Surface plasmon resonance (SPR) operates by detecting the attenuation in a beam of light reflected from a thin gold film surface [116]. The metal surface, typically gold, supports an evanescent wave while the analytes bound to the surface absorb this wave, causing a sharp drop in reflected intensity. This sharp attenuation can be detected and used to determine what is on the gold surface. A quartz crystal microbalance (QCM) measures the frequency change in a resonating thin quartz crystal to determine the amount of mass added [117]. Both of these methods will register a detection signal, regardless of what attaches to the transduction surface. These surfaces must be *functionalized* for them to act as detectors of specific biological agents . The surface must be prepared such that only one certain species will occupy the surface, meaning that it is only this species that will be responsible for the detected signal. Quartz-crystal microbalance and SPR-based devices have been functionalized with polymers [118, 119], thin films [120], and self-assembled monolayers (SAMs) [121–123]. In all these cases, the active layer on the device will only permit a very specific analyte to attach to the surface, thus only that analyte will be responsible for the output signal from the device.

Such is the same with resonant micro- and nanomechanical sensors. Certain sensor applications are concerned with only detecting very small masses regardless of what attaches to the resonant sensor [42, 44, 45], because the impinging particles are already filtered sufficiently, or the precise mass of the particle is enough to determine its identity. Many times, however, the purpose of a biosensor is to differentiate between many particles of similar size and composition (proteins, antibodies, viruses, etc.) [124]. In these cases, the cantilevers or bridges must be coated with an active layer that will permit attachment of a specific particle, while blocking all others. By *immobilizing* certain molecules that act as receptors for a specific particle the device can detect the desired particle without the need for it to be labeled [125]. Ji *et al.* are able to sense the bending of a cantilever due to the adsorption of metal ions onto a self-assembled monolayer [23, 126], while Cherian *et al.* do the same but with a coating of proteins [127]. Hwang *et al.*, [128], and Kumar *et al.*, [129], both use immobilized antibodies to specifically bind the corresponding antigens to the

surface. Yoo *et al.* use bound bacteria to detect the presence of toxins [130], while Adrega *et al.* use single-strand DNA immobilized via organosilanes to detect the complementary DNA strand [131]. In the cases of biological detection, the receptor for the biomolecule must be bound to the cantilever surface by an intermediate chemistry, of which there are many. A common approach to this task is to use self-assembled monolayers, or *SAMs*.

4.1.2 SAMs: Self-Assembled Monolayers
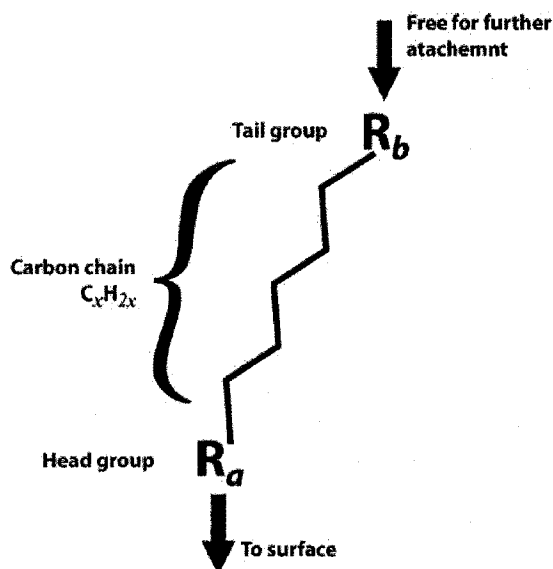
Figure 4.1: SAM molecule. The head group binds covalently to the substrate, while the tail group can be customized to accept a multitude of analytes.

The term *self-assembled monolayer* is used to describe a species that will adsorb to a surface and spontaneously self-organize into a complete or semi-complete monolayer [132]. Figure 4.1 depicts a generic SAM molecule, consisting of a head group used to attach to the substrate surface, a carbon chain of arbitrary length which through van der Waals forces assists in self-organization, and a highly-customizable tail group to which other species may bind [133]. It is this highly customizable tail group which, through proper synthesis, can bind to a broad range of chemical and biological agents [134, 135], usually in a manner similar to naturally occurring molecular recognition [136]. As for the head group, there are two variations typically used in MEMS/NEMS biodetection immobilization strategies: alkane-thiols and organo-silanes.

Alkane-thiols are alkyl chains with a thiol group, S-H, as the chain head. This sulfur-containing terminal creates a remarkably strong and stable bond with gold [132], which is why its use in biofunctionalization of transducer surfaces is so widespread [137]. Because of this, whenever alkane-thiols are employed a thin layer of gold must first be deposited onto the transducer surface [138–140]. This is also true in the case of resonating cantilevers used as mass sensors, where one or both sides of the beam are Au-coated [141, 142]. However, while gold allows the thiol-based SAM to form, it also affects the resonant behavior of the cantilever. In vacuum it has been shown that the addition of metals to the surface of a resonator decreases its Q-factor with increasing metal-thickness [143,144]. For thick (multiple-μm) resonators, 25 - 38 nm of gold [139,141,142] will not significantly degrade the quality factor. In NEMS, with cantilever thicknesses of $t = 20$ - 60 nm, the gold coatings compose half of the cantilever, nullifying the efforts to produce high-Q resonators. Furthermore, the thermoelastic damping of a metal layer on a silicon-based resonator has has been shown to be negligible at low frequencies (MEMS) but quite significant at frequencies above 1 MHz, squarely in the regime of NEMS [145]. One approach in this situation involves patterning the gold-coating such that it is present only at certain section of the cantilever [146]. However, this introduces complex alignment into an already delicate fabrication process. Thus, for larger MEMS resonators or static-mode cantilever measurements, using alkane-thiol monolayers on a Au-layer to bind target species is perfectly acceptable, but the smaller, more sensitive NEMS devices would benefit from an alternative immobilization chemistry.

Organosilane compounds consist of a Si-based head group. The compounds require the presence of silanol groups, Si-OH, in order to bind to the surface by forming siloxane bonds, Si-O-Si [132]. The synthesis chemistry for organo-silanes is quite well known [147, 148], meaning the tail group may be customized, similar to alkane-thiols, as may the head group to facilitate specific bonding-orientations or cross-linking [149]. Additionally, vapor-phase deposition of silanes has been shown to be quite successful and reliable [150], and the facilities and expertise to perform it are readily available [151]. This is of particular interest in this project since vapor deposition would enable *in-situ* deposition during resonance assaying as well as remove a wet-chemistry step from the functionalization

process, improving the chances of a high device yield. Finally, for silicon-based resonators there is no significant pretreatment required to allow the attachment of organosilane species. A bath in an acidic peroxide solution is indeed enough to create silanol groups on the surface Si atoms [152], thus readying the surface for functionalization. Organosilane chemistry has recently been used to create biologically favorable conditions on silicon-based and oxidized surfaces [153–156], although its use in resonating mechanical sensors remains limited.

4.2 SiCN Functionalization Strategy

MERCAPTOPROPYL TRIMETHOXYSILANE
(a)

MERCAPTOPROPIONIC ACID
(b)
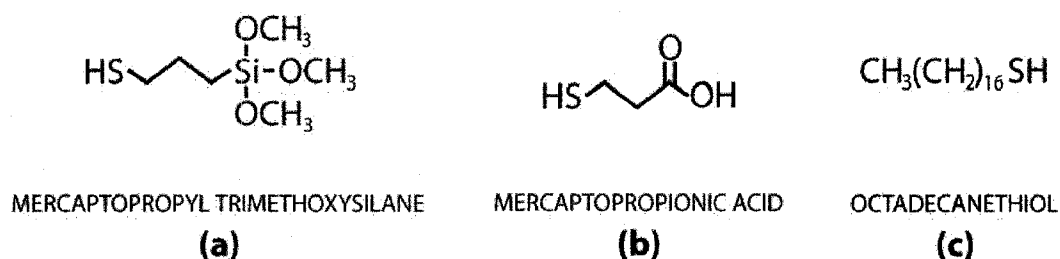
OCTADECANETHIOL
(c)

Figure 4.2: The three SAMs employed in this section; (a) mercaptopropyl trimethoxysilane, (b) mercaptopropionic acid, (c) octadecanethiol.

Before a biosensing platform can be tested, a strategy for immobilizing biological agents onto the resonator surface must be developed. The surface composition of the film is characterized using XPS. The SiCN material-signal in FT-IR is so large that it washes out any surface signals. Following this the binding affinity of three SAMs will be investigated. *Mercaptopropyl trimethoxysilane* (MPTMS, figure 4.2a) is expected to bind to the Si-OH present on the surface, since SiCN is silicon-based [155]. *Mercaptopropionic acid* (MPA, figure 4.2b) will form a peptide bond between its carboxyl group and any possible NH_2 on the SiCN surface. This was considered because the presence of active amine groups on the SiCN surface would allow for direct immobilization of antibodies, and FT-IR indicated the presence of NH_2 in the film bulk. *Octadecanethiol* (ODT, figure 4.2c) is not expected to bind to the surface at all and acts as an experimental control here. Finally, the ability to deposit MPTMS via a vapor-phase method is investigated.

4.3 Experiment

Silicon carbonitride (SiCN) was deposited 40 nm-thick onto (100) single crystal silicon wafers (500 μm thick, 100 mm diameter) using the process described in chapter 2, following a standard 20 minute piranha clean (3:1 sulfuric acid:hydrogen peroxide) [55]. The same piranha clean was performed a second time following a 2 hour, 500 °C post-deposition anneal, after which the wafers were then cleaved into 1 × 1 cm chips. X-ray photoelectron spectroscopy (XPS) was performed at the Alberta Centre for Surface Engineering and Science using a Kratos AXIS 165 surface analysis system. The bare SiCN surface was scanned in survey mode to determine the relative composition. Then the SiCN sample was sputter-etched in a weak argon plasma to remove the top layer of native oxide and survey-scanned again.

Sets of the the aforementioned 1 cm^2 chips were then subjected to surface modification with MPTMS (95%), mercaptopropionic acid (MPA, 99%), and octadecanethiol (ODT, 95%), all purchased from Sigma-Aldrich (Milwaukee, WI), by placing one chip each in a 10:1 solution of toluene and the chosen chemical for 2 hours. MPTMS and MPA were chosen to determine the degree of surface binding via active silanol and amine groups, respectively. Octadecanethiol was introduced to act as a control experiment, as it should not bind to anything. Following modification the chips were again analyzed by XPS, specifically looking for the sulfur signal at as a marker. Sulfur is indeed present in the MPTMS (figure 4.2a), MPA (figure 4.2b), and ODT (figure 4.2c) molecules, but not in the bare SiCN surface. A fourth chip of SiCN was survey-scanned to act as a reference. Following these trials, one final chip was placed in a dry seal vacuum desiccator with 200 μL of MPTMS and pumped down to 30 mTorr for 10 hours, then subsequently survey scanned in XPS, again looking for the sulfur signal.

4.4 Results

Figure 4.3 displays the atomic percent (at%) content of each element (Si, C, N, O) in the SiCN surface and bulk. As seen in figure 4.3, before sputter-etching the the SiCN surface contains a significant amount of oxygen, 16 at%, mainly bonded to silicon. However, after

sputter-etching to remove the surface oxide (1-2 nm) the oxygen content drops to 2 at%. It is this abundance of surface oxygen that led to choosing MPTMS as one of the tested monolayers. It was already known from the material development experiments in chapter 2 that a small part of the SiCN films was composed of oxygen. This experiment confirms the presence of silicon and oxygen on the surface, most likely in the form of silanol groups.
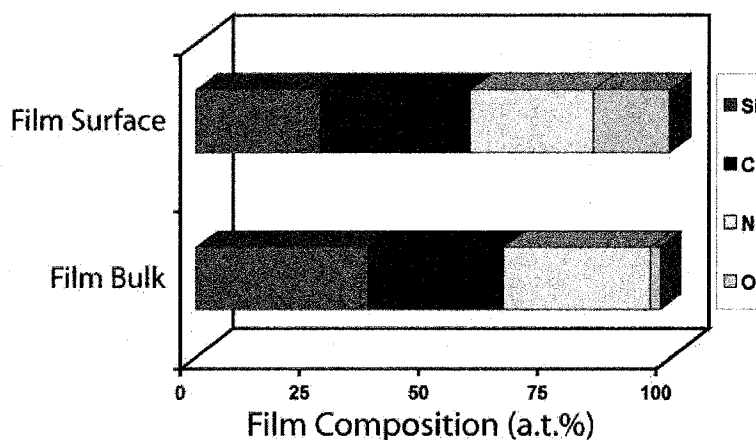

Figure 4.3: The surface composition of the SiCN surface as characterized by XPS before and after sputter-etching 2 - 3 nm into the film.

Figure 4.4 shows the XPS spectrum results of the three chips modified with the different chemicals, as well as the experimental control. The S 2p peak of sulfur located at 162 eV is the signal usually sought to confirm the presence of the element [157]. However, the silicon Si 2s peak is located at 155 eV and is quite strong. Also, when bonded to oxygen or other atoms, the Si 2s-orbital electrons are known to exhibit kinetic energy loss through inelastic scattering, causing "ripples" in the XPS spectra at energies above the 155 eV Si 2s signal [158–160]. It is for this reason that the weaker S 2s peak at 226 eV was rather used to determine the presence of sulfur, and thus the presence of the bound monolayer.

Figure 4.4) is the entire SiCN XPS survey spectrum capture. Figures 4.4b-d are the magnified scans of the 226 eV S 2s peak for the unmodified control sample, and the samples treated with MPA and ODT, respectively. These plots show mainly noise, with any minuscule signal in this region being less than 0.4 at% of the surface composition, attributable to trace contamination or physisorption. However, the sample treated with the MPTMS solution (figure 4.2c) shows a much more prominent and pronounced S 2s signal,

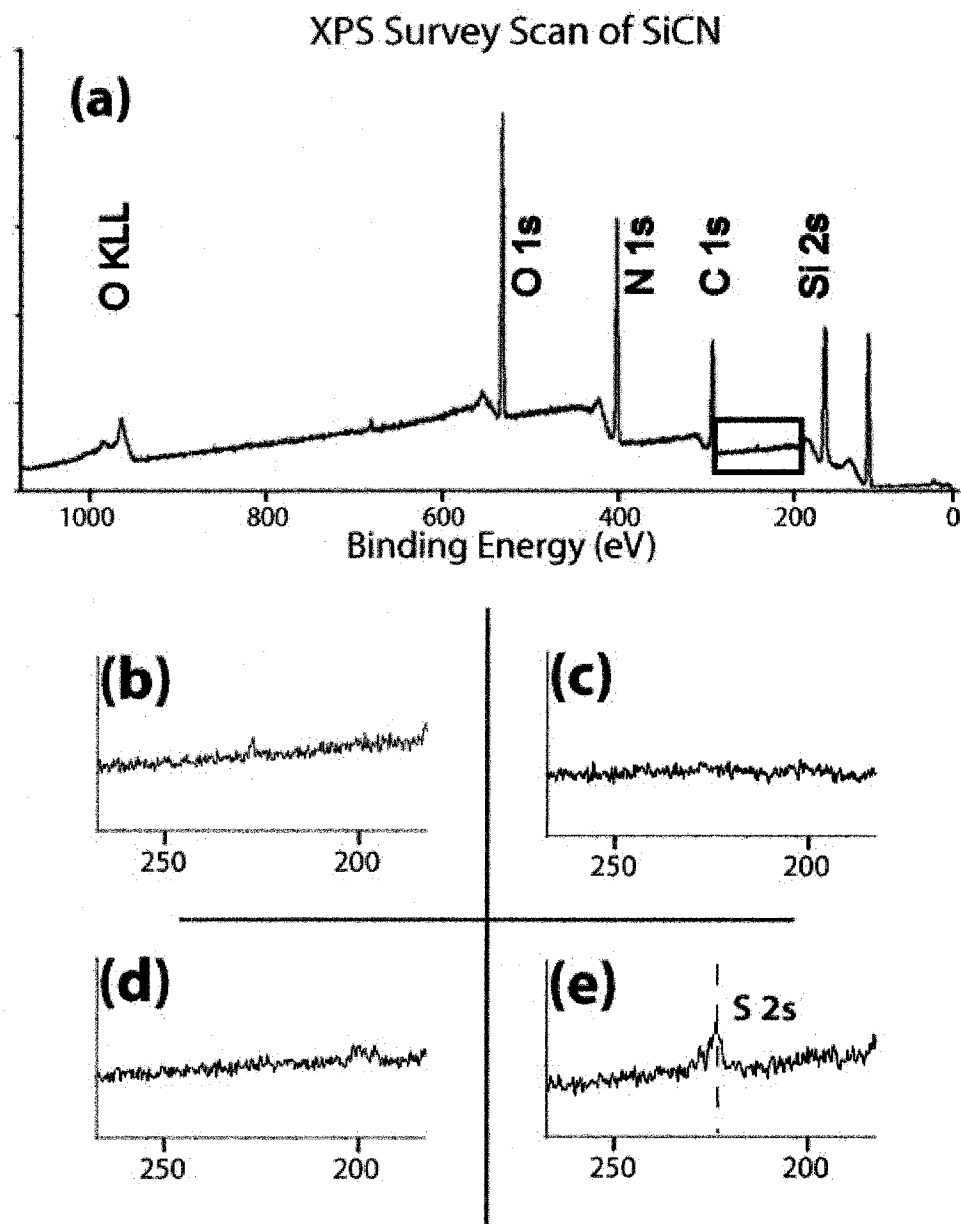Figure 4.4: (a) the entire SiCN surface survey scan. A close up of the region where a sulfur XPS signal is expected (226 eV) for (b) the unmodified control, (c) the MPA treated sample, (d) the ODT treated sample, and (e) the MPTMS treated sample.

corresponding to 2 - 5 at% of the composition. This indicates a strong affinity of MPTMS over the other chemistries attempted, further supporting the existence of silanol groups on the surface, thus making an organosilane-based immobilization scheme the method choice for detection experiments. Petoral *et al.* observed very similar results with respect to the XPS spectrum of an MPTMS-modified silicon-based-surface, including the blocking of the S 2p signal at 162 eV by the very strong Si 2s peak [155].

Finally, samples treated with vapor-phase MPTMS were characterized using XPS. The S 2s signal was also quite prominent in these vapor-silanized samples, with the percent surface composition of sulfur being 3 - 3.8 at%. The ability to deposit MPTMS by this vapor-method grants the opportunity of *in-situ* surface modification during resonance assaying.

4.5 Conclusion

The presence of silicon and oxygen on the film surface in relatively large amounts, as well as the observation that MPTMS readily binds to the SiCN surface indicates that there are silanol groups on the surface, and that an organosilane-based immobilization chemistry is suitable for this system. Vapor-phase MPTMS deposition was found to be a reliable method, and enables *in-situ* detection of monolayer formation.

The purpose of this section of the project was to determine a suitable immobilization chemistry for the biotin-streptavidin complex for the biosensing proof-of-concept. This system has been chosen to test the biosensing capabilities of the SiCN resonators due to it being readily available and well-understood. By depositing a monolayer of MPTMS the SiCN surface effectively becomes "thiol-terminated" (figure 4.5a). Biotin molecules with integrated thiol groups , or thiolated-biotin, can be purchased from Pierce Biotechnology (Rockford, IL 61105), and will readily form a covalent disulfide bond with the thiol group on the MPTMS layer (figure 4.5b). Finally, streptavidin, with four biotin-binding sites, will specifically attach to this functionalized surface (figure 4.5c).
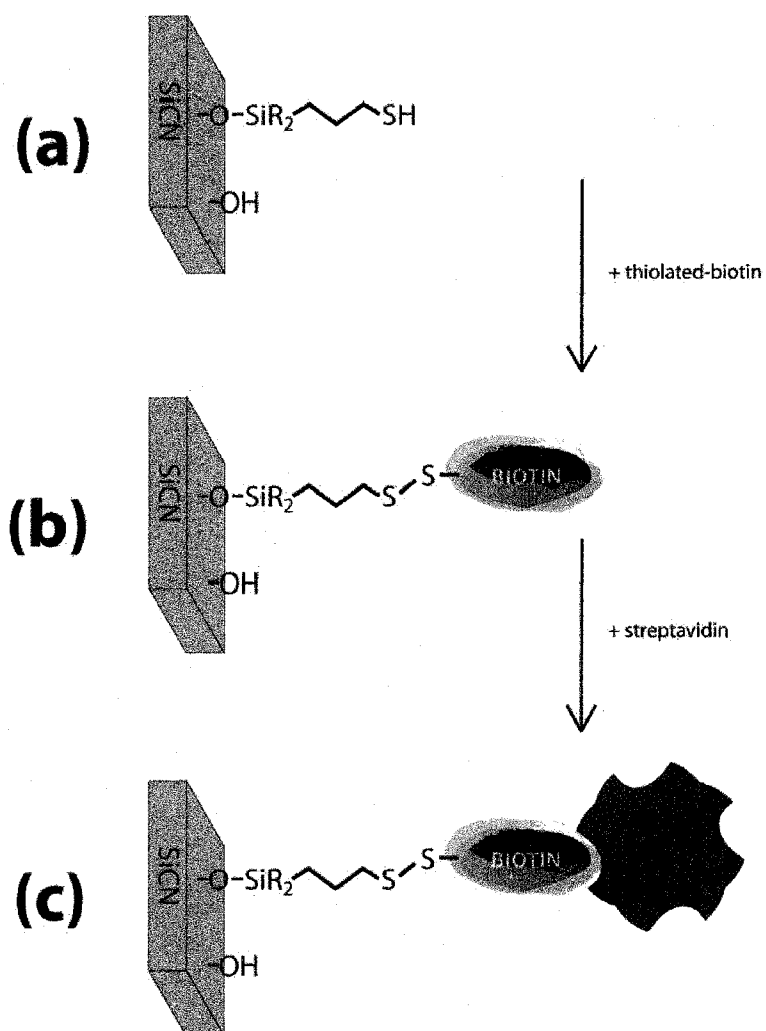
Figure 4.5: The final streptavidin immobilization chemistry to be applied to the biosenor platform. This figure depicts the SiCN surface following the addition of: (a) MPTMS, (b) thiolated-biotin, and (c) streptavidin.

5

NEMS BioSensing Platform

The objective of this project was to create a biological-mass-sensing device. The previous chapters examined the creation of high-quality resonators from optimized silicon carbonitride, as well as the functionalization scheme to be used to specifically attach the streptavidin protein to the resonators. This chapter ties together all the work presented so far by investigating the development of stiction-resistant resonators and performing mass-detection using these structures, thus completing this project.

5.1 Introduction

Micro- and nanomechanical resonant structures have been demonstrated as a highly-sensitive means of detecting extremely small masses. Thundat *et al.* had already shown detection of humidity [161] and mercury vapor [162] in the mid-1990s by measuring both the shift in resonance frequency of a cantilever due to the added mass, as well as the static deflection due to surface adsorption. Cherian *et al.* [127] and Ji *et al.* [126] did similar work detecting static deflections of cantilevers due to adsorbed metal ions. Calleja *et al.* have sensed the adsorption of thiolated single-strand DNA on gold-coated polymer cantilevers [25], also by measuring static deflection. Recently, Ilic *et al.* have

54

used the frequency shift of resonating cantilevers to detect the presence of viruses [42], as well as single DNA molecules [43] that are bound to the silicon via a functionalized surface, followed by Adrega *et al.* in 2006 [131]. Similarly, Hwang *et al.* demonstrated *in-situ* dynamic specific-detection of a prostate-specific antigen on a self-actuating PZT-incorporating cantilever [128]. Godin *et al.* [163] and Datskos *et al.* [164] both measured the effects of adsorbed-thiols from vapor phase onto gold-coated cantilevers in real-time, again by measuring static deflection. Most recently, Li *et al.* have demonstrated room-temperature, real-time detection of chemisorbed species on nano-scale VHF cantilevers with attogram resolution [165]. As indicated, the trend in micro/nano-resonator sensors is leading towards higher sensitivity, vapor and liquid phase analyte binding, and real-time measurement of this binding. With the advent of zeptogram sensing-capabilities [45] the thrust in these endeavors will soon turn to single-atom, and eventually single Dalton detection possibly enabling the use of nano-oscillators used as mass-spectrometers.

The work in chapter 2 enabled silicon carbonitride thin film to be deposited at a desired composition and stress. Chapter 3 explored the resonant behavior of the material and justified the use of high-stress SiCN films for fabricating resonators. Chapter 4 justified the use of the chosen immobilization scheme for the biotin-streptavidin complex. This chapter ties all of this work together and executes the goal of this project: the development of a silicon carbonitride resonator-based biosensing platform.

To start, the device stiction issue presented in chapter 3 must be addressed and resolved. Second generation (*2G*) high-quality bridge resonators are fabricated using a KOH-etching process. These bridges are then modified with MPTMS using vapor-phase deposition and measured to observe the frequency shift. This is followed by quasi-real-time monitoring of the deposition resulting in *in-situ* detection of vapor-phase MPTMS forming a monolayer. Lastly, biotin is immobilized onto the SiCN surface via MPTMS, facilitating the specific attachment of the streptavidin protein and its detection. A final experiment is performed to determine the degree of non-specific binding to the bare SiCN resonators.

5.2 Experiment

For the second generation of resonators, 35 nm of SiCN was deposited via PECVD at a gas ratio of 4:1 NH_3:DES onto piranha-cleaned (3:1 H_2SO_4:H_2O_2) single-crystal (100) silicon wafer. The SiCN-coated wafers were annealed in a MiniBrute 3-zone tube furnace at 500°C for 8 hours to drive off hydrogen and maximize tensile stress, followed by another piranha clean, and a BOE bath in preparation for resist. These wafers were then cleaved into 1.5 × 1.5 cm squares, and spin-coated with a bilayer of polymethyl methacrylate (PMMA) 950/495 for electron-beam lithograhpy (EBL) resist. Patterning of the substrates was performed at the University of Alberta Micromachining and Nanofabrication Facility using a Raith150 electron beam lithography system with a 20 μm aperture, an accelerating voltage of 10 kV, and an area dose of 125 μC/cm^2. Following development of the PMMA in 1:3 methyl-isobutyl-ketone (MIBK): isopropanol (IPA), an electron beam evaporator was used to deposit a 30 nm chromium (Cr) masking layer, after which a 5 min ultrasonic acetone bath facilitated lift-off of the PMMA to produce the patterned etch mask. A Trion Technology Phantom II reactive ion etcher (RIE) was used to anisotropically etch the Cr patterned SiCN in a 30 s, 4:1 SF_6:O_2 plasma recipe adapted from literature [103], and described in chapter 3. The Cr etch mask was then removed with a 20 min bath in stock chrome etch (Arch Chemicals, Inc.). These 2G structures were released by anisotropically etching the bulk silicon substrate underneath the SiCN in a potassium hydroxide (KOH) bath (75 °C), saturated with isopropanol, for 5-10 minutes, followed by a 3-bath rinse in DI water. Bridges released using KOH were found to not require supercritical drying and were thus dried in a gentle nitrogen flow. This resulted in the 35 mn-thick, 400 nm-wide, and 40 - 50 μm-long structures seen in figure 5.1. These structures were then cleaned once more in piranha, this time to ensure the presence of silanol groups.

One set of resonators is subjected to resonance assaying in the interferometry setup described in [104], and in chapter 3. Then the sample was placed inside a vacuum desiccator with an open vial containing 100 μL of MPTMS (95% pure) and the chamber was pumped to 200 mTorr and left sealed for 10 hours. Following silanization the resonators were measured a second time in the interferometry setup to observe the frequency shift.

A second set of nanobridges was placed in the resonance-testing vacuum with 200 μL of MPTMS in a 5 mL glass vial partitioned by a butterfly valve. All functional bridges on the sample were measured once, then the butterfly valve was opened, the system was pumped to 80 mTorr, and the vacuum pump was disconnected. The vacuum chamber was left in this state for a set period of time (30 min, 1 h, 2 h) depending on the stage of the experiment. All functional bridges were measured again following this silanization period, and then another silanization period was initiated. These silanization periods continued such that the total time added to 8 hours. The resonant frequency of all beams was tracked as a function of silanization time.

A third set of beams was measured, then subjected to the same 10 hour silanization described above. The sample was subsequently placed in 0.5 mL solution of 2 mg/mL biotin-HPDP mixed with dimethyl sulfoxide, then mixed with 0.5 mL of phosphate buffered saline and incubated for 30 min. Following rinsing, the sample was placed in a 10 μM solution of streptavidin, again for 30 min, and rinsed a final time. A detailed description of this protocol is outlined by Janshoff *et al.* [166]. A resonance measurement was made of all beams that remained functional through this process.

Lastly, a solution was prepared of 10 μM streptavidin (0.5 mL) treated with a 1 mM biotin-HPDP solution (0.5 mL), which is a 2.5 times excess as streptavidin has only four biotin binding spots. A fourth set of bridges was measured, then placed in this solution for 60 min at a temperature of 37 °C. Upon removal the sample was rinsed with toluene, trichloromethane, and ethanol, gently blown dry with N_2, and finally measured for a second time to assess resonant frequencies.

5.3 Results

5.3.1 Stiction Resistant Nanobridges

Chapter 3 discussed how the 1G surface micromachined structures succumbed to stiction. The solution presented called for an enlargement of the beam-substrate gap, but doing this using purely surface micromachining techniques would result in a large anchor-undercut with adverse effects on resonance. It was because of this prediction that an increased SiO_2
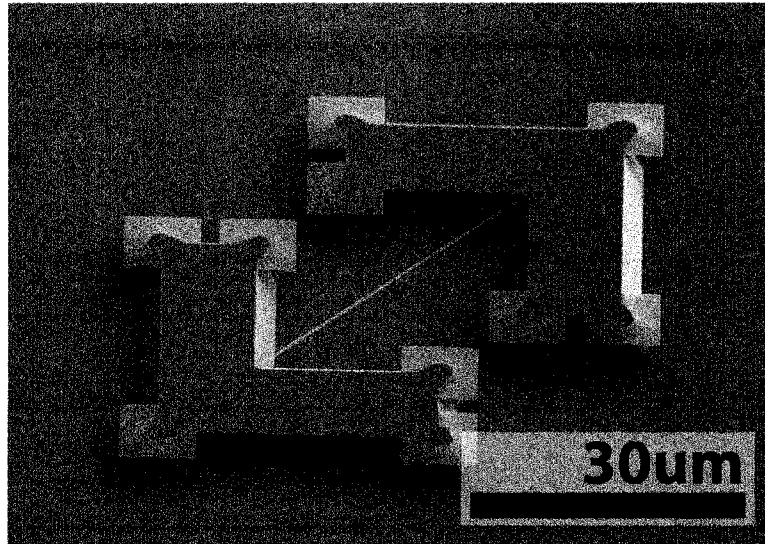
Figure 5.1: A 35 mn-thick, 400 nm-wide, 45 μm-long bridge that is immune to the effects of stiction, produced by KOH-etching of the substrate to release the bridge.
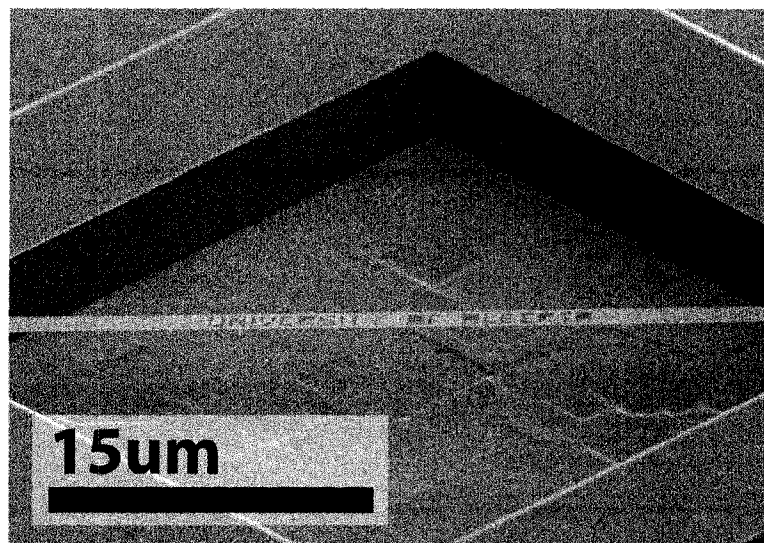

Figure 5.2: A 35 mn-thick bridge produced using the same KOH-release process as the above bridge. The bridge itself as well as the text in it were etched in one step, using the anisotropic RIE recipe from chapter 3.

thickness was not used to reduce stiction. Instead, a process using KOH to etch the bulk silicon substrate was developed. KOH is usually employed in bulk micromachining for its ability to etch silicon anisotropically, a result of the (111) crystal plane resisting the chemical [3]. A sample of the 2G structures, typically 400 nm-wide, 30 - 50 μm-long, can be seen in figure 5.1.

Once again, as in chapter 3, non-resonator structures were fabricated. The etched beam in figure 5.2 again demonstrates the durability of SiCN in this process.

Electron-beam lithography provided the ability to precisely align the patterns to the crystal planes of the substrate. The use of KOH to anisotropically remove Si resulted in bridges that have less than 50 nm of undercut at the anchoring point, while having a 3 - 6 um gap between the bridge and the substrate, allowing the devices seen in figure 5.1 to be dried under a nitrogen flow without requiring supercritical drying. These 2G structures are capable of withstanding wet-chemical processing, which was essential for applying biotin and streptavidin. Indeed, this is the very reason the KOH-based process was developed.

5.3.2   Resonance Before & After 10 h Silanization

Figure 5.3 plots the bridge resonance of the first set of resonators before and after deposition of the MPTMS layer. Out of 15 bridges fabricated (5 × 50 μm, 5 × 45 μm, and 5 × 40 μm in length) all but 1 50 μm-long beam were functional. All beams show a consistent decrease in center frequency after the addition of the organosilane. We expect a shift in frequency that follows the 1st-order mass-sensitivity equation [42]:

$$\frac{\Delta m}{\Delta f} = \frac{2m_{osc}}{f_o} \tag{5.1}$$

$\frac{\Delta m}{\Delta f}$ is called the *mass sensitivity* (g/Hz) of the resonator, with m_{osc} being the mass of the resonating structure and f_o is the initial frequency of the oscillator.

Table 5.1 presents the average frequency shifts per bridge length. It is necessary to average the frequency shifts since the measurement error introduced by operating the interferometry setup can be as high as 10 kHz. Additionally, beam uniformity may vary from structure to structure, causing deviations in the measurements. It should be noted that shorter beams experience larger shifts than longer ones. This is expected from interpreting
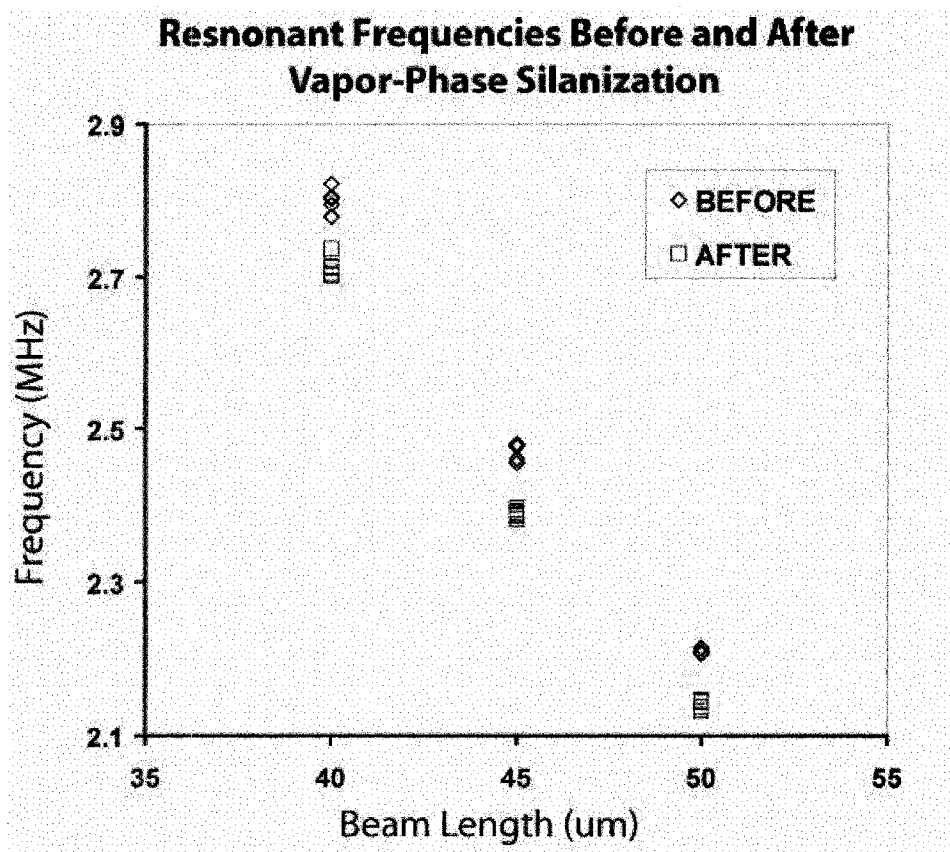
Figure 5.3: The fundamental resonant frequencies of the 14 bridges measured. All beams were 35 nm-thick and 400 nm-wide.

Table 5.1: Mass Detection Calculations For Silanized Resonators

Beam Length μm	50	45	40
Average Shift Δf (kHz)	70.5	80.9	86.7
Mass Sensitivity $\frac{\Delta m}{\Delta f}$(ag/Hz)	1.47	1.18	0.92
Added Mass Δm (fg)	104	96	80
Bridge Surface Area ($\times 10^{-11}$ m^2)	4.66	4.19	3.73
Mass Per Area (mg/m^2)	*2.22*	*2.28*	*2.14*

equation 5.1 since the mass the bridge loses by becoming shorter is roughly an order of magnitude greater that the mass of the monolayer lost by the reduction in surface area. Thus, since the added mass changes very little, the shorter bridge with the higher sensitivity will experience a larger frequency shift.

Table 5.1 also calculates the added mass of the MPTMS layer. Again, as expected the shorter beams report the addition of less mass due to their decreased surface area. To prove that the decreased mass observed by the shorter beams is actually due to the smaller surface area, the surface areas of the three different bridge lengths have been calculated. Finally, these numbers are used to produce the mass-per-area detected by the beams, 2.22 ± 0.07 mg/m^2, averaged across the three beam lengths. Using a molecular mass of 196.34 g/mol (Sigma-Aldrich), this corresponds to 6.8×10^{18} MPTMS molecules per m^2. Assuming each MPTMS molecule occupies ~ 1 nm^2, these measurements yield an estimated 6.8 monolayers of MPTMS coverage.

Thus, these SiCN NEMS resonators have a theoretical mass sensitivity of ~ 1 ag/Hz, and have demonstrated detection capabilities on the order of femtograms.

5.3.3 *In-Situ* Silanization Detection

Figure 5.4 shows the frequencies of two 2G bridges (50 μm and 40 μm in length) as they are silanized over an 8 hour period. The term *quasi*-real-time is applied here because the silanization was stopped to perform the measurements. Both plots show a distinct increase in the resonant frequency of the structure within the first 2 hours, followed by a rapid decrease, and ending with a steady frequency decrease after 4 hours. Equation 3.1 dictates the frequency should decrease as mass is added to the oscillator, which is observed after 4 hours. It should be noted that MPTMS is *trifunctional*, meaning that there are three sites on
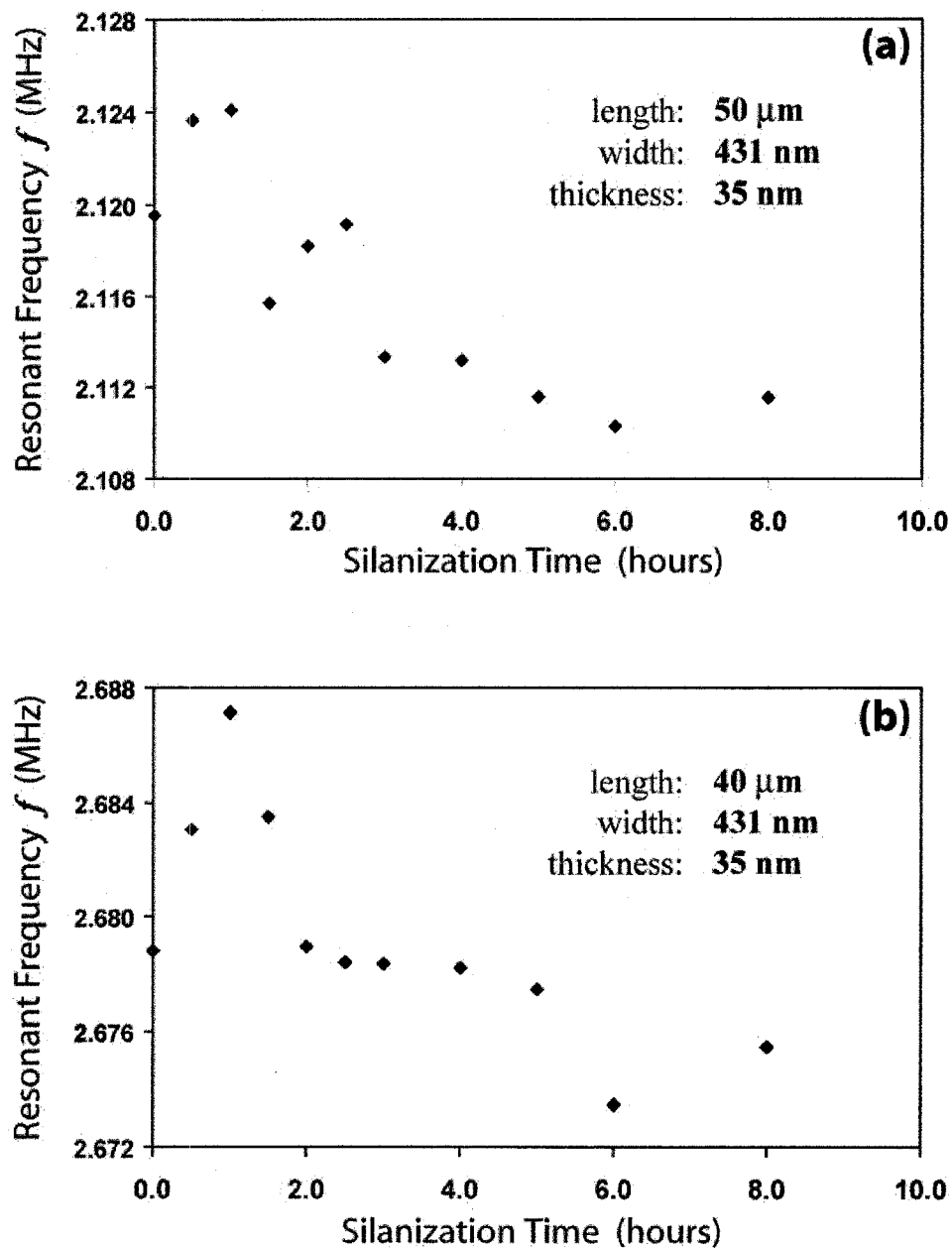
Figure 5.4: Two bridge resonators, measured at the stated time intervals during silanization. Note in both beams the initial increase in resonance frequency.

the molecule where siloxane bonds may form. This allows the molecules to not only bond to the surface, but also to bond laterally with each other and *cross-link* to form a network and a multilayer [149]. Additionally, it was shown in chapter 3 that the behavior of these bridges is stress dominated, as seen from the L^{-1} dependence of length on frequency. Work from chapter 3 also brought forth equation 5.2 as the solution to the Euler-Bernoulli beam equation for a stress dominated beam:

$$f_{o,stress} = 0.271 \frac{1}{L} \sqrt{\frac{\sigma_o}{\rho}} \tag{5.2}$$

Keeping beam length L and density ρ constant, an effective increase in the tensile stress in the beam would cause a corresponding increase in the resonant frequency.

Godin *et al.* made similar observations regarding the vapor-phase deposition of an alkylthiol onto a gold coated cantilever [163]. By monitoring static deflection they were able to detect the surface stress created by the formation of the thiol monolayer. Godin also notes that in most cases the deflection of the cantilever quickly reaches a maximum, then slowly settles to a certain values, which he corresponded to an initial high-tensile stress due to early stages of SAM formation, followed by a relaxation dependent on deposition geometry [163]. As described earlier, the trifunctional nature of MPTMS allows for it to cross-link and to form a multilayer [149]. Thus, in similar fashion to the work by Godin *et al.*, the resonating bridges can be used to approximately determine the surface stress induced by the deposited organosilane. Calculating stress, $\Delta\sigma$ from cantilever deflection is done through straightforward application of the Stoney Formula [167]. With a bridge that is clamped at both ends, however, the radius of curvature is always infinite (in the case of tensile stresses) and there is no static deflection. Alternatively, since an increase in tensile stress in a beam will cause a corresponding increase in the spring constant k, seen in equation 3.28, the stress can be determined through analysis of the resonance shifts. To start, in this system one can safely assume that all frequency decreases are due to the addition of mass, and all frequency increases are due to an increase in tensile stress of the beam. The following assumptions must also be made:

1. The resonant behavior of these bridges is stress dominated, as shown by the observed L^{-1}-dependence in chapter 3.

2. Mass is being added to the beam at a constant rate (i.e. grams/second) via vapor deposition.

3. The stress change in the bridge due to the added molecules will reach a constant value and cease to change further as more molecules are added (at some point) [163, 168, 169].

Following these assumptions the effects of mass and stress on the behavior of the bridge may be decoupled. This can be done by effectively canceling the mass added by the adsorbed MPTMS. Assume an invariant spring constant k (so the effect of stress remains after removal of the mass), a frequency f_o of the unmodified resonator, a frequency of f'_o after modification, an oscillator mass of m_{osc}, and an added mass of Δm. Through a simple rearrangement of equation 3.1, equation 5.3 is created:

$$f_o = f'_o \sqrt{\frac{m_{osc} + \Delta m}{m_{osc}}} \qquad (5.3)$$

which *zeroes* the mass of the added molecules, without removing the effect they have on the spring constant. However, to apply this formula an accurate estimate of the mass being added must first be obtained. By applying assumption 2, a least squares fit can be made to the data in figure 5.4 to estimate the average frequency shift per hour, excluding data points in the $0h < t < 3h$ where the frequency is clearly dominated by the changing stress. Then, by applying equation 5.1, the mass added per hour can be determined. Table 5.2 displays the mass-loading estimate found using this method.

Table 5.2: Mass Loading Estimate Calculations

Beam Length μm	40	50
Average Shift per Hour $\frac{\Delta f}{\Delta t}$ (Hz/h)	-571	-470
Fundamental Frequency f_o (MHz)	2.679	2.120
Oscillator Mass m_{osc} (pg)	1.146	1.433
Mass Added per Hour $\frac{\Delta m}{\Delta t}$ (ag/h)	*488*	*635*
Bridge Surface Area ($\times 10^{-11}$ m^2)	3.73	4.66
Mass Added per Area per Hour (μg/m^2/h)	*13.1*	*13.6*

The mass-added-per-hour-per-area has been calculated to show that this method of estimating the mass-loading is at least consistent with itself across the two different bridge

lengths. With this estimate, the raw data in figure 5.4 can be shifted to frequency values representative of an added layer mass of zero, while still retaining the effect of the added surface stress. Since the resonant behavior is stress dominated, equation 5.2 can be applied to find the tensile stress in the bridge as MPTMS is being deposited. These calculations revealed a tensile stress of 290 MPa in the 50 μm-long bridge, and 296 MPa in the 40 μm-long structure before the vapor-deposition had begun. These numbers are then used to calculate the change in total stress caused by the addition of the MPTMS layer as a function of time. Finally, this added stress actually has nothing to do with the bridge structure itself (the bridge is only the transduction element) and is contained entirely within the surface layer added. Stress is given in units of Pascals, Pa, which is equivalent to Newtons per metre-squared, N/m^2. To acquire a value for the surface stress induced by the MPTMS, the change in stress is multiplied by the half the beam thickness, 17.5 nm, since the beam thickness is 35 nm but the deposition occurs on both the top and bottom surfaces; the edges can be neglected since they are more than 10 times smaller than the top and bottom surfaces. This results in an estimate of the surface stress in the forming of the MPTMS multilayer, where maximum values of 0.024 N/m and 0.035 N/m are obtained from the 50 μm- and 40 μm-long bridges, respectively. Figure 5.5 shows the evolution of the surface stress in the 50 μm (figure 5.5a) and 40 μm (figure 5.5b) bridges.

Both bridges experience the same rapid increase in surface stress over the first hour, followed by a rapid decrease over the second hour, finally settling at some non-zero value. While the 40 μm bridge stabilizes at a tensile stress, $\sim$0.005 N/m, the 50 μm structure settles at a compressive value, $\sim$-0.02 N/m. This can be attributed to a measurement error that may have resulted in the first one or two data points being several kHz higher than they should have been. This is completely reasonable since, as stated earlier, the method of measurement can introduce errors such as this through manual aligning and focusing of the laser. The 6-hour data point in figure 5.5b also appears to be suffering from this affliction. Nonetheless, a standard procedure was followed while taking measurements, and these deviations are exceptions to the rule, and do not greatly hinder the overall results.
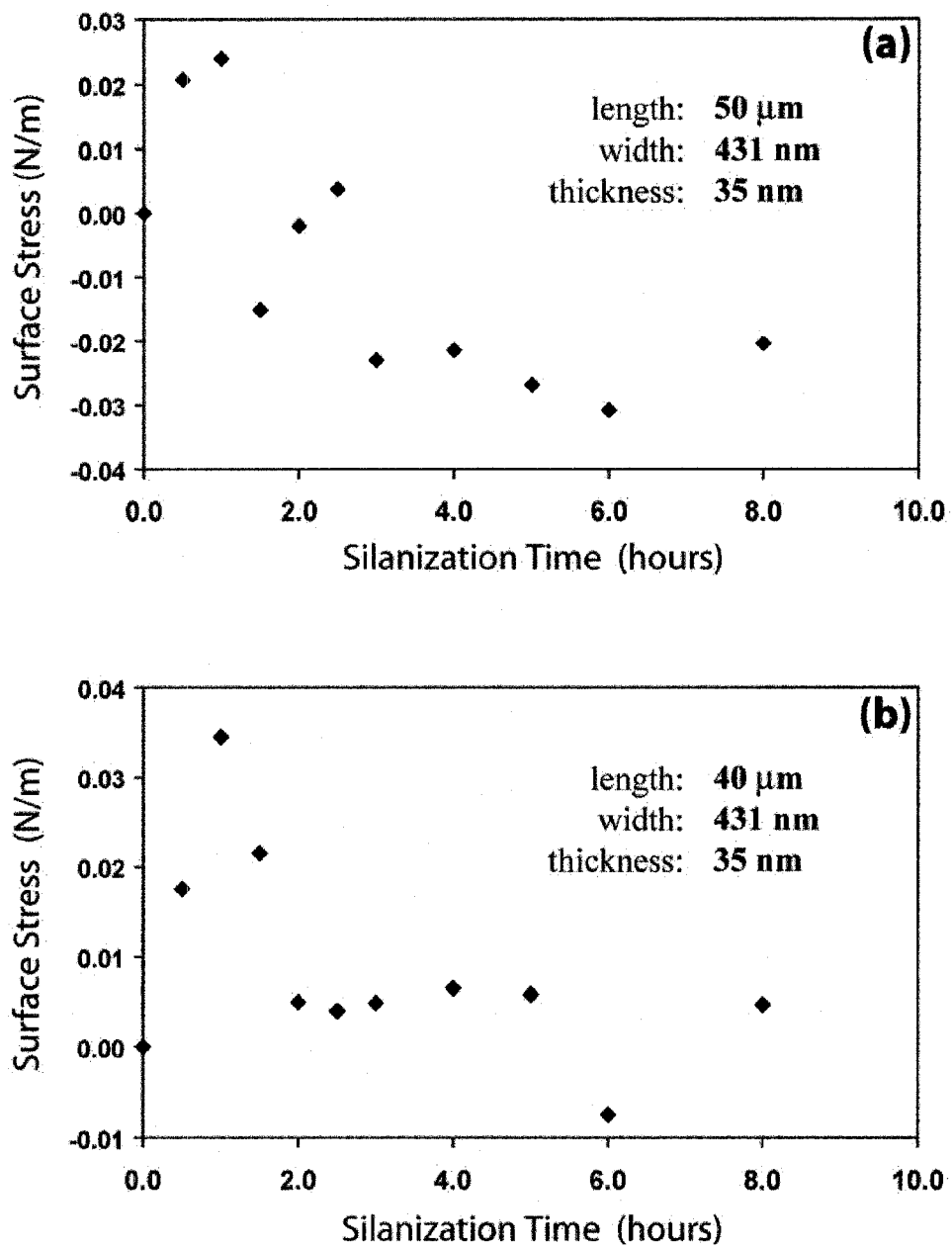
Figure 5.5: Plots of the surface stress induced during the formation of a MPTMS multilayer on the surface of a (a) 50 μm, and (b) 40 μm beam.
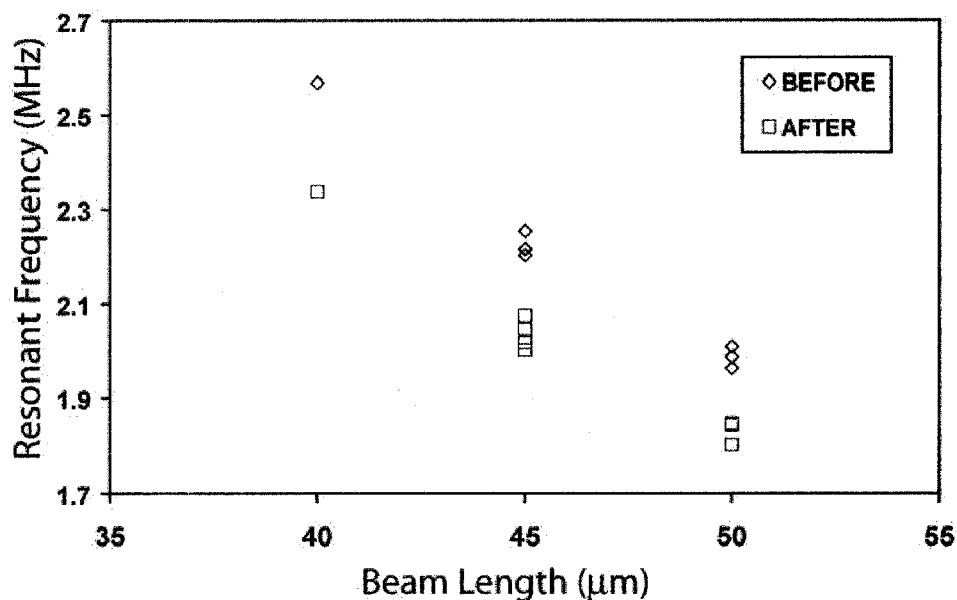
Figure 5.6: A plot of the frequencies of the bridges measured before and after a complete MPTMS/biotin/streptavidin treatment.

5.3.4 BioSensing: The Detection of Streptavidin

Figure 5.6 plots the resonance frequency of the bridges before and after they were subjected to the entire silanization/biotin/streptavidin protocol, thus the frequency shift will reflect the added mass of the entire tri-layer. The same analysis was performed on this data as was performed on that in figure 5.3. It should be noted that, due to the multi-step wet chemistry process in this experiment, fewer bridges survived than did in the previous experiments; 3 $\times$ 50 μm, 4 $\times$ 45 μm, and 1 $\times$ 40 μm long bridges were capable of being measured after the entire functionalization process was completed. Table 5.3 contains the quantitative data obtained from these resonators.

Table 5.3: Mass Detection Calculations For Streptavidin Coated Bridges

Beam Length μm	**50**	**45**	**40**
Average Shift Δf (kHz)	157	185	231
Mass Sensitivity $\frac{\Delta m}{\Delta f}$(ag/Hz)	1.63	1.31	1.01
Added Mass Δm (fg)	256	243	233
Bridge Surface Area ($\times 10^{-11}$ m^2)	4.66	4.19	3.73
Mass Per Area (mg/m^2)	*5.49*	*5.81*	*6.24*

Once again it should be noted that the frequency shifts observed, and therefore the

mass detected, is a result of the 3-layers on the beam; MPTMS, biotin, and streptavidin. An estimate can be obtained of the mass-per-area of biotin/streptavidin added, using the estimated mass-per-area (M/A) of the MPTMS coating from a previous section. The average M/A of the 3-layer deposition is 5.8 ± 0.4 mg/m^2, while only the 10 h vapor MPTMS layer is 2.2 ± 0.1 mg/m^2. Therefore, 3.6 mg/m^2 can be attributed to the biotin/streptavidin mass. It should be noted that biotin is a linker molecule with a molecular weight of 244 g/mol, while streptavidin, a protein, has a molecular weight of $\sim$60,000 g/mol (1 g/mol = 1 Da), obtained from Pierce Biotechnology. Converting the mass values, the total mass of a biotin (0.4 zg) and streptavidin (99.6 zg) molecule together is 100 zg, so the estimated surface density of streptavidin is 3.6×10^{16} m^{-2}. This corresponds to roughly one streptavidin molecule per 27 nm^2, approximately a sparse monolayer.

5.3.5 Streptavidin Negative Control
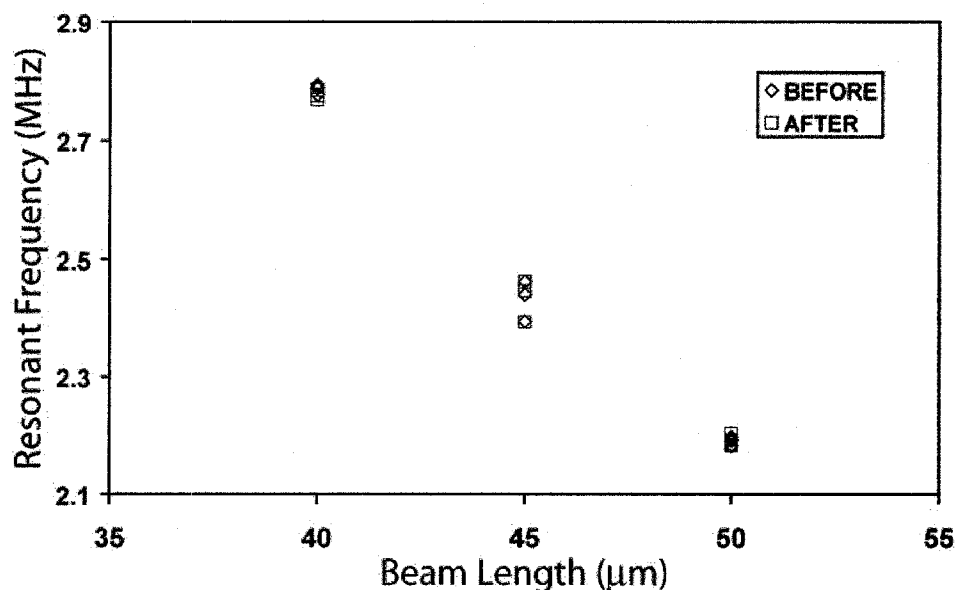
Figure 5.7: A plot of the frequencies of the bridges measured before and after application of streptavidin with blocked binding sites, to test the degree of non-specific binding to the resonators.

Figure 5.7 plots the bridge resonance measurements of the negative control experiment. The bridges were measured once (following piranha cleaning) and then again following the application of over-biotinylated-streptavidin to the bare resonators (no silanization

occurred in this instance). This experiment was intended to investigate the amount of physisorption by biological particles to the clean SiCN surface. As is shown, the before and after frequencies are quite similar, and many of the shifts can be attributed to random measurement errors as previously discussed. To follow suit with the analysis of the previous data sets, table 5.4 collects the frequency shifts of these bridges.

Table 5.4: Negative Control Frequency Shift Data

Beam Length μm	50	45	40
Average Fundamental Frequency f_o (MHz)	2.191	2.433	2.786
Average Shift Δf (kHz)	0	-1	9
Standard Deviation in Shift (kHz)	6	4	2

In all cases, the standard deviation is roughly the same magnitude as the shift itself. Thus it can be concluded that there is very little or no non-specific attachment of the streptavidin protein to the bare SiCN surface.

5.4 Conclusion

Fabrication of stiction resistant second generation nanobridges was successful. Using KOH to anisotropically etch the bulk-Si substrate dramatically decreased the amount of anchor undercut, making a 3 - 6 μm gap between the SiCN bridge and silicon possible, thus eliminating the chances of stiction. These 2G resonators were then used to detect a multilayer of MPTMS formed during a 10 h vapor deposition. An average multilayer mass of 2.22 $\pm$ 0.07 mg/m^2 is detected after this deposition, corresponding to roughly 6.8 MPTMS monolayers. Quasi-real-time frequency detection during the deposition of MPTMS yielded a mass-per-hour loading of 488 ag/h and 635 ag/h for the 40 μm and 50 μm bridges respectively, corresponding to an average mass-per-area-per-hour loading of 13.4 $\pm$ 0.4 μg m^{-2}/h. A stress change in the beam during MPTMS deposition was also observed, which is believed to be a result of the trifunctional organosilanes cross-linking, causing an initial tensile stress which relaxes shortly after. The maximum value of this surface stress induced by the cross-linking organosilane was found to be 0.024 N/m for the 50 μm bridge and 0.035 N/m for the 40 μm bridge, and this discrepancy was attributed to random measurement errors during focusing and aligning of the laser spot. With respect to

biosensing, a layer of attached streptavidin was detected, and a mass-per-area of 3.6 mg/m^2 was believed to be the result of the attached protein layer. A streptavidin surface density of 3.6×10^{16} m^{-2} was calculated from this, corresponding to one protein particle per 27 nm^2 on the resonator surface. Finally, a negative control experiment found that there is very little or no attachment of bio-molecules to the bare SiCN surface without functionalization.

6

Conclusions

6.1 Summary

During this work the successful development of materials and fabrication processes have been used to ultimately produce a sub-femtogram, biosensing platform.

The plasma-enhanced chemical vapor deposition (PECVD) of silicon carbonitride (SiCN) was investigated, resulting in an ability to reliably control both the chemical composition and intrinsic stress of the thin film. By modulating the gas flow ratio NH$_3$:DES, the carbon-to-nitrogen ratio, C:N, could be varied between 0.7 and 2.5, resulting in a corresponding range in Young's modulus from 162 GPa to 148 GPa, and hardness from 23.5 GPa to 20.9 GPa, respectively. Post-deposition annealing was found to drive out the incorporated hydrogen, allowing the film to form additional Si-N bonds, changing the intrinsic stress from compressive ($\sigma = \sim$-800 MPa) to tensile ($\sigma = \sim$400 MPa).

Surface micromachined cantilevers and bridges were fabricated to investigate the effects of film composition and stress on resonant behavior, respectively. Cantilever resonance was used to determine the speed of sound, which was found to be $\sqrt{\frac{E}{\rho}} = 8.35 \times 10^3$ m/s and $\sqrt{\frac{E}{\rho}} = 6.20 \times 10^3$ m/s for the low and high C:N ratio films, respectively. High tensile stress in the bridge structures was found to give them a dependence of frequency on length

71

of $f \propto L^{-1}$, and increased the quality factor of the resonators to values as high as 26 000. Issues of stiction were addressed as they pertained to resonator fabrication.

It was determined that active silanol groups on the SiCN surface could be used to attach mercaptopropyl trimethoxysilane (MPTMS), which could be deposited effectively by both wet chemistry and vapor-phase methods. Mercaptopropionic acid (MPA) and octadecanethiol (ODT) were found not to attach significantly to the surface. Thiolated biotin was used as a linking molecule to attach streptavidin to the silanized surface.

A machining process was developed using potassium hydroxide to release the 2G nanobridges while preventing severe undercutting of the anchors, thus allowing for a large (3 - 6 μm) gap between the bridge and substrate. This drastically reduced the effects of stiction and eliminated the need for specialized drying techniques. These stiction resistant resonators were then used for mass detection. A 10 hour vapor-phase silanization was performed and found to deposit 2.22 $\pm$ 0.07 mg/m^2 of MPTMS on the bridges. *In-situ* silanization revealed an initial surface stress due to cross-linking of the MPTMS layer of 0.024 N/m for the 50 μm bridge and 0.035 N/m for the 40 μm bridge measured. Upon relaxation of this surface stress to a constant value, the mass-per-area-per-hour loading during silanization was found to be 13.4 $\pm$ 0.4 μg m^{-2}/h. A layer of thiolated-biotin and streptavidin was added to the resonator surface following a 10 hour vapor silanization. A mass-per-area of 3.6 mg/m^2 was attributed to the addition of the streptavidin, and a surface density value of 3.6 $\times$ 10^{16} m^{-2}, or one protein per 27 nm^2, was obtained. Lastly it was shown that there is no measurable attachment of proteins to the clean, unfunctionalized SiCN surface.

Thus SiCN nanomechanical resonators have been successfully developed, and their capabilities as detectors of biological molecules has been established.

6.2 Recommendations for Future Work

Several improvements may be made to further future work. First, decreasing the width and length of the bridges used would result in higher resonant frequencies and mass sensitivities. This would entail optimization of the exposure parameters during electron-beam lithography, and perhaps reexamining the type of resist used or its application

process. Bridge thickness was pushed sufficiently low (35 nm) for this work, but an optimization of the flow rates and a decrease in deposition rate could yield thinner SiCN films (<20nm).

A great deal of sensitivity could be gained from a restructuring of the interferometry-based resonance-assaying setup. Vibration isolation and the addition of a butterfly valve to the vacuum pump attachment would result in a system wherein the pressure could be controlled precisely and the pump could remain on at all times. This would allow for vapor-phase silanization to occur continuously during measurements and *true* real-time mass detection. While this platform is very well suited to biosensing, much work could also be done on investigating the behavior of forming monolayers and cross-linking.

Finally, to practically apply these resonators as biosensors, their behavior in liquid must still be examined. Fabricating SiCN nano-bridges in microfluidic channels would allow for observation and subsequent optimization of quality factor in a liquid environment, followed by the eventual creation of a microfluidic NEMS-based protein sensor.

Bibliography

[1] S. Middelhoek, "Celebration of the tenth transducers conference: the past, present and future of transducer research and development," *Sensor. Actuat. A-Phys.*, vol. 82, pp. 2–23, May 2000.

[2] S. D. Senturia, *Microsystem Design*. New York, NY: Springer Science+Business Media, Inc., 1st ed., 2001.

[3] S. A. Campbell, *The Science and Engineering of Microelectronic Fabrication*. New York, NY: Oxford Univerity Press, 2nd ed., 2001.

[4] B. G. Streetman and S. Banerjee, *Solid State Electronic Devices*. Upper Saddle River, NJ: Prentice Hall, 5th ed., 2000.

[5] J. M. Bustillo, R. T. Howe, and R. S. Muller, "Surface micromachining for microelectromechanical systems," *Proc. IEEE*, vol. 86, pp. 1552–1574, Aug 1998.

[6] J. W. Judy, "Microelectromechanical systems (MEMS): fabrication, design and applications," *Smart Mater. Struct.*, vol. 10, pp. 1115–1134, Dec 2001.

[7] K. E. Petersen, "Silicon as a mechanical material," *Proc. IEEE*, vol. 70, no. 5, pp. 420–457, 1982.

[8] "ADXL50: Monolithic accelerometer with signal conditioning (obsolete)." Data Sheet, Analog Devices, Inc., Norwood, MA 1996.

[9] "ADXL78: Single-axis, high-g iMEMS accelerometer." Data Sheet, Analog Devices, Inc., Norwood, MA 2005.

[10] "Analog Devices and Nintendo collaboration drives video game innovation with iMEMS motion signal processing technology." Press Release, Analog Devices, Inc., Norwood, MA 2006.

[11] "ADXL330: Small, low-power, 3-axis +/-3g iMEMS accelerometer." Data Sheet, Analog Devices, Inc., Norwood, MA 2007.

[12] R. Neul, U. M. Gomez, K. Kehr, W. Bauer, J. Classen, C. Doring, E. Esch, S. Gotz, J. Hauer, B. Kuhlmann, C. Lang, M. Veith, and R. Willig, "Micromaching angular rate sensors for automitive applications," *IEEE Sens. J.*, vol. 7, pp. 302–309, Feb 2007.

[13] L. Spangler and C. J. Kemp, "ISAAC: Integrated silicon automotive accelerometer," *Sensor. Actuat. A-Phys.*, vol. 54, pp. 523–529, Jun 1996.

[14] J. N. Palasagaram and R. Ramadoss, "Mems-capacitive pressure sensor fabricated using printed-circuit-processing techniques," *IEEE Sens. J.*, vol. 6, pp. 1374–1375, Dec 2006.

[15] W. P. Eaton and J. H. Smith, "Micromachined pressure sensors: review and recent developments," *Smart Mater. Struct.*, vol. 6, pp. 530–539, May 1997.

[16] G. Binnig, C. F. Quate, and C. Gerber, "Atomic Force Microscope," *Phys. Rev. Lett.*, vol. 56, pp. 930–933, Mar 1986.

[17] P. C. Markiewicz, "Atomic force microscopy studies of mesoscopic structures," Master's thesis, University of Toronto, Toronto, ON, 1998.

[18] M. A. Roseman, "Design and characteristics of a low temperature atomic force microscope," Master's thesis, McGill University, Montreal, QC, 1997.

[19] K. W. Ng, *Scanning Probe Micro scopes*, ch. 3, pp. 75–100. Norwell, MA: Kluwer Academic Publishers, 2004.

[20] J. Li, "A scanning probe study of self-assembled alkylsilane films," Master's thesis, Queen's University, Kingston, ON, 2001.

[21] H. P. Lang, M. Hegner, E. Meyer, and C. Gerber, "Nanomechanics from atomic resolution to molecular recognition based on atomic force microscopy technology," *Nanotechnology*, vol. 13, pp. R29–R36, Oct 2002.

[22] H. P. Lang, M. K. Baller, R. Berger, C. Gerber, J. K. Gimzewski, F. M. Battiston, P. Fornaro, J. P. Ramseyer, E. Meyer, and H. J. Guntherodt, "An artificial nose based on a micromechanical cantilever array," *Anal. Chim. Acta*, vol. 393, pp. 59–65, Jun 1999.

[23] H. F. Ji, T. Thundat, R. Dabestani, G. M. Brown, P. F. Britt, and P. V. Bonnesen, "Ultrasensitive detection of CrO_4^{2-} using a microcantilever sensor," *Anal. Chem.*, vol. 73, pp. 1572–1576, Apr 2001.

[24] J. D. Adams, B. Rogers, L. Manning, Z. Hu, T. Thundat, H. Cavazos, and S. C. Minne, "Piezoelectric self-sensing of adsorption-induced microcantilever bending," *Sensor. Actuat. A-Phys.*, vol. 121, pp. 457–461, Jun 2005.

[25] M. Calleja, M. Nordstrom, M. Alvarez, J. Tamayo, L. M. Lechuga, and A. Boisen, "Highly sensitive polymer-based cantilever-sensors for DNA detection," *Ultramicroscopy*, vol. 105, pp. 215–222, Nov 2005.

[26] H. Sone, Y. Fujinuma, and S. Hosaka, "Picogram mass sensor using resonance frequency shift of cantilever," *Jpn. J. Appl. Phys.*, vol. 43, pp. 3648–3651, Jun 2004.

[27] M. Villarroya, J. Verd, J. Teva, G. Abadal, E. Forsen, F. P. Murano, A. Uranga, E. Figueras, J. Montserrat, J. Esteve, A. Boisen, and N. Barniol, "System on chip mass sensor based on polysilicon cantilevers arrays for multiple detection," *Sensor. Actuat. A-Phys.*, vol. 132, pp. 154–164, Nov 2006.

[28] J. K. Gimzewski, C. Gerber, E. Meyer, and R. R. Schlittler, "Observation of a chemical-reaction using a micromechanical sensor," *Chem. Phys. Lett.*, vol. 217, pp. 589–594, Jan 1994.

[29] Z. Y. Hu, T. Seeley, S. Kossek, and T. Thundat, "Calibration of optical cantilever deflection readers," *Rev. Sci. Instrum.*, vol. 75, pp. 400–404, Feb 2004.

[30] N. V. Lavrik, M. J. Sepaniak, and P. G. Datskos, "Cantilever transducers as a platform for chemical and biological sensors," *Rev. Sci. Instrum.*, vol. 75, pp. 2229–2253, Jul 2004.

[31] R. Berger, C. Gerber, H. P. Lang, and J. K. Gimzewski, "Micromechanics: A toolbox for femtoscale science: "towards a laboratory on a tip"," *Microelectron. Eng.*, vol. 35, pp. 373–379, Feb 1997.

[32] R. Berger, H. P. Lang, C. Gerber, J. K. Gimzewski, J. H. Fabian, L. Scandella, E. Meyer, and H. J. Guntherodt, "Micromechanical thermogravimetry," *Chem. Phys. Lett.*, vol. 294, pp. 363–369, Sep 1998.

[33] "Concentris Introduces the First Measurement Kits for Nanomechanical Canitlever Sensors." Press Release, Concentris GmbH., Basel, Germany, Jul 2007.

[34] I. R. Voiculescu, M. E. Zaghloul, R. A. McGill, and J. F. Vignola, "Modelling and measurements of a composite microcantilever beam for chemical sensing applications," *J. Mech. Eng. Sci.*, vol. 220, pp. 1601–1608, Oct 2006.

[35] M. Tanaka, "An industrial and applied review of new MEMS devices and features," *Microelectron. Eng.*, vol. 84, pp. 1341–1344, May-Aug 2007.

[36] N. Yazdi, F. Ayazi, and K. Najafi, "Micromachined inertial sensors," *Proc. IEEE*, vol. 86, pp. 1640–1659, Aug 1998.

[37] B. Ilic, D. Czaplewski, M. Zalalutdinov, H. G. Craighead, P. Neuzil, C. Campagnolo, and C. Batt, "Single cell detection with microcantilever oscillators," *J. Vac. Sci. Tech. B*, vol. 19, pp. 2825–2828, Nov-Dec 2001.

[38] S. D. Parker, J. S. Wall, and E. Hunter, "Analysis of Mason-Pfizer monkey virus gag particles by scanning transmission electron microscopy," *J. Virol.*, vol. 75, pp. 9543–9548, Oct 2001.

[39] Z. Nie, Y.-K. Tzeng, H.-C. Chang, C.-C. Chiu, C.-Y. Chang, C.-M. Chang, and M.-H. Tao, "Microscopy-based mass measurement of a single whole virus in a cylindrical ion trap," *Agnewandte Chemie*, vol. 45, pp. 8131–8134, 2006.

[40] A. Gupta, D. Akin, and R. Bashir, "Single virus partilce mass detection using microresonators with nnoscale thickness," *Appl. Phys. Lett.*, vol. 84, pp. 1976–1978, Mar 2004.

[41] M. L. Quillin and B. W. Matthews, "Accurate calculation of the density of proteins," *Acta Crystallogr.D*, vol. 56, pp. 791–794, Jul 2000.

[42] B. Ilic, Y. Yang, and H. G. Craighead, "Virus detection using nanoelectromechanical devices," *Appl. Phys. Lett.*, vol. 85, pp. 2604–2606, Sep 2004.

[43] B. Ilic, Y. Yang, K. Aubin, R. Reichenbach, S. Krylov, and H. G. Craighead, "Enumeration of DNA molecules bound to a nanomechanical oscillator," *Nano Lett.*, vol. 5, pp. 925–929, May 2005.

[44] K. L. Ekinci, X. M. H. Huang, and M. L. Roukes, "Ultrasensitive nanoelectromechanical mass detection," *Appl. Phys. Lett.*, vol. 84, pp. 4469–4471, May 2004.

[45] Y. T. Yang, C. Callegari, X. L. Feng, K. L. Ekinci, and M. L. Roukes, "Zeptogram-scale nanomechanical mass sensing," *Nano Lett.*, vol. 6, pp. 583–586, Apr 2006.

[46] V. Sazonova, Y. Yaish, H. Ustunel, D. Roundy, T. A. Arias, and P. L. McEuen, "A tunable carbon nantotube electromechanical oscillator," *Nature*, vol. 431, pp. 284–287, Sep 2004.

[47] P. Poncharal, Z. L. Wang, D. Ugarte, and W. A. de Heer, "Electrostatic deflections and electromechanical resonances of carbon nanotubes," *Science*, vol. 283, pp. 1513–1516, Mar 1999.

[48] C. Forster, V. Cimalla, K. Brucker, M. Hein, J. Pezoldt, and O. Ambacher, "Micro-electromechanical systems based on 3C-SiC/Si heterostructures," *Mat. Sci. Eng. C-Bio S*, vol. 25, pp. 804–808, Dec 2005.

[49] C. A. Zorman and M. Mehregany, "Advanced processing techniques for silicon carbide MEMS and NEMS," *Mater. Sci. Forum.*, vol. 457-460, pp. 1451–1456, 2004.

[50] B. Ilic, S. Krylov, K. Aubin, R. Reichenbach, and H. G. Craighead, "Optical excitation of nanoelectromechanical oscillators," *Appl. Phys. Lett.*, vol. 86, p. Art. No. 193114, May 2005.

[51] L. Sekaric, D. W. Carr, S. Evoy, J. M. Parpia, and H. G. Craighead, "Nanomechanical resonant structures in silicon nitride: fabrication, operation and dissipation issues," *Sensor. Actuat. A-Phys.*, vol. 101, pp. 215–219, Sep 2002.

[52] S. S. Hullavarad, R. D. Vispute, B. Nagaraj, V. N. Kulkarni, S. Dhar, T. Venkatesan, K. A. Jones, M. Derenge, T. Zheleva, M. H. Ervin, A. Lelis, L. J. Scozzie, D. Habersat, A. E. Wickenden, L. J. Currano, and M. Dubey, "Advances in pulsed-laser-deposited aln thin films for high-temperature capping, device passivation, and piezoelectric-based RF MEMS/NEMS resonator applications," *J. Electron. Mater.*, vol. 35, pp. 777–794, Apr 2006.

[53] L. Sekaric, J. M. Parpia, H. G. Craighead, T. Feygelson, B. H. Houston, and J. E. Butler, "Nanomechanical resonant structures in nanocrystalline diamond," *Appl. Phys. Lett.*, vol. 81, pp. 4455–4457, Dec 2002.

[54] I. S. Forbes, J. R. Rabeau, J. I. B. Wilson, and P. John, "Nanocrystalline diamond films for nanotechnology applications," *Mater. Sci. Technol.*, vol. 19, pp. 553–556, May 2003.

[55] L. M. Fischer, N. Wilding, M. Gel, and S. Evoy, "Low-stress silicon carbonitride for the machining of high-frequency nanomechanical resonators," *J. Vac. Sci. Technol. B*, vol. 25, pp. 33–37, Jan-Feb 2007.

[56] Y. Wang, J. A. Henry, A. T. Zehnder, and M. A. Hines, "Surface chemical control of mechanical energy losses in micromachined silicon structures," *J. Phys. Chem. B*, vol. 107, pp. 14270–14277, Dec 2003.

[57] R. F. Wiser, J. Y. Chung, M. M., and C. A. Zorman, "Polycrystalline silicon-carbide surface-micromachined vertical resonators - part i: Growth study and device

fabrication," *Journal of Microeletromechanical Systems*, vol. 14, pp. 567–578, Jun 2005.

[58] X. M. H. Huang, X. L. Feng, C. A. Zorman, M. Mehregany, and M. L. Roukes, "VHF, UHF and microwave frequency nanomechanical resonators," *New J. Phys.*, vol. 7, p. Art. No. 247, Nov 2005.

[59] N. Sabate, D. Vogel, A. Gollhardt, J. Keller, C. Cane, I. Gracia, J. R. Morante, and B. Michel, "Measurement of residual stress by slot milling with focused ion-beam equipment," *J. Micromech. Microeng.*, vol. 16, pp. 254–259, Feb 2006.

[60] D. Resnik, U. Aljancic, D. Vrtacnik, M. Mozek, and S. Amon, "Mechanical stress in thin film microstructures on silicon substrate," *Vacuum*, vol. 80, pp. 236–240, Oct 2005.

[61] P. J. French, P. M. Sarro, R. Mallee, E. J. M. Fakkeldij, and R. F. Wolffenbuttel, "Optimization of a low-stress silicon nitride process for surface-micromachining applications," *Sensor. Actuat. A-Phys.*, vol. 58, pp. 149–157, Feb 1997.

[62] F. F. Chen, *Introduction to Plasma Physics and Controlled Fusion*. New York, NY: Plenum Press, 2nd ed., 1984.

[63] K. A. Stoffel, A., W. Kronast, and B. Muller, "LPCVD against PECVD for micromechanical applications," *J. Micromech. Microeng.*, vol. 6, pp. 1–13, Mar 1996.

[64] R. A. Levy, L. Chen, J. M. Grow, and Y. Yu, "A comparative study of plasma enhanced chemically vapor deposited Si-O-H and Si-N-C-H films using the environmentally benign precursor diethylsilane," *Mater. Lett.*, vol. 54, pp. 102–107, May 2002.

[65] D. E. Kotecki and J. D. Chapplesokol, "Hydrogen incorporation in silicon nitride films deposited by remote electron-cyclotron resonance chemical-vapor-deposition," *J.Appl. Phys.*, vol. 77, pp. 1284–1293, Feb 1995.

[66] T. P. Smirnova, A. M. Badalyan, V. O. Borisov, V. V. Kaichev, L. F. Bakhturova, V. N. Kichai, V. I. Rakhlin, and B. A. Shainyan, "Plasma deposition and properties of silicon carbonitride films," *Inorg. Mater.*, vol. 41, pp. 706–712, Jul 2005.

[67] P. Jedrzejowski, J. Cizek, A. Amassian, J. E. Klemberg-Sapieha, J. Vlcek, and L. Martinu, "Mechanical and optical properties of hard sicn coatings prepared by PECVD," *Thin Solid Films*, vol. 447, pp. 201–207, Jan 2004.

[68] B. K. Agrawal, P. S. Yadav, and B. K. Ghosh, "Vibrational excitations in a-Si_3N_4-H(D) alloys," *J. Phys. C: Solid State Phys.*, vol. 21, pp. 3397–3406, Jun 1988.

[69] Z. Yin and F. W. Smith, "Optical dielectric function and infrared absorbtion of hydrogenated amorphous silicon nitride films: Experimental results and effective-medium-approximation analysis," *Phys. Rev. B*, vol. 42, pp. 3666–3675, Aug 1990.

[70] A. M. Wrobel, I. Blaszczyk-Lezak, A. Walkiewicz-Pietrzykowska, D. M. Bielinski, T. Aoki, and Y. Hatanaka, "Silicon carbonitride films by remote hydrogen-nitrogen plasma CVD from a tetramethyldisilazane source," *J. Electrochem. Soc.*, vol. 151, no. 11, pp. C723–C730, 2004.

[71] E. Cianci, F. Pirola, and V. Foglietti, "Analysis of stress and composition of silicon nitride thin films deposited by electron cyclotron resonance plasma-enhanced chemical vapor deposition for micrpfabrication processes," *J. Vac. Sci. Technol. B*, vol. 23, pp. 168–172, Jan/Feb 2005.

[72] L. G. Boehme, C., "H loss mechanism during anneal of silicon nitride: Chemical dissociation," *J. Appl. Phys.*, vol. 88, pp. 6055–6059, Nov 2000.

[73] L. Cai, A. Rohatgi, and E. M. A. Yang, D., "Effects of rapid thermal anneal on refractive index and hydrogen content of plasma-enhanced chemical vapor deposited silicon nitride films," *J. Appl. Phys.*, vol. 80, pp. 5384–5388, Nov 1996.

[74] C. W. Pearce, R. F. Fetcho, M. D. Gross, R. F. Koefer, and R. A. Pudliner, "Characteristics of silicon-nitride deposited by plasma-enhanced chemical vapor-

deposition using a dual frequency radiofrequency source," *J. Appl. Phys.*, vol. 71, pp. 1838–1841, Feb 1992.

[75] A. Kaushik, H. Kahn, and A. H. Heuer, "Wafer-level mechanical characterization of silicon nitride MEMS," *J. Microelectromech. S.*, vol. 14, pp. 359–367, Apr 2005.

[76] C. R. Miranda, K. V. Tretiakov, and S. Scandolo, "A computational study of elastic properties of disordered systems with voids," *J. Non-Cryst. Solids*, vol. 352, pp. 4283–4286, Nov 2006.

[77] E. Spanakis, E. Stratakis, P. Tzanetakis, and Q. Wang, "Elastic properties, intrinsic and photoinduced stress in hydrogenated amorphous-silicon thin films with different hydrogen," *J. Appl. Phys.*, vol. 89, pp. 4294–4300, Apr 2001.

[78] K. R. Williams, K. Gupta, and M. Wasilik, "Etch rates for micromachining processing - part II," *J. Microelectromech. S.*, vol. 12, pp. 761–778, Dec 2003.

[79] U. Schubert and N. Husing, *Synthesis of Inorganic Materials*. Weinheim, Germany: Wiley-VCH Verlag GbmH & Co. KGaA, 2nd ed., 2005.

[80] S. G. Kandlikar and W. J. Grande, "Evolution of microchannel flow passages - thermohydraulic performance and fabrication technology," *Heat Transfer Eng.*, vol. 24, pp. 3–17, Jan-Feb 2003.

[81] B. Loechel, "Thick-layer resists for surface micromachining," *J. Micromech. Microeng.*, vol. 10, pp. 108–115, Jun 2000.

[82] P. Ohlckers, A. Hanneborg, and M. Nese, "Batch processing for micromachined devices," *J. Micromech. Microeng.*, vol. 5, pp. 47–56, Jun 1995.

[83] D. Dornfeld, S. Min, and Y. Takeuchi, "Recent advances in mechanical micromachining," *Crip Annals - Manuf. Tech.*, vol. 55, no. 2, pp. 745–768, 2006.

[84] S. Reyntjens and R. Puers, "A review of focused ion beam applications in microsystem technology," *J. Micromech. Microeng.*, vol. 11, pp. 287–300, Jul 2001.

[85] M. McNie, D. King, C. Vizard, A. Holmes, and K. W. Lee, "High aspect ratio micromachining (HARM) technologies for microinertial devices," *Microsyst. Technol.*, vol. 6, pp. 184–188, Aug 2000.

[86] M. C. Wu, "Micromachining for optical and optoelectronic systems," *Proc. IEEE*, vol. 85, pp. 1833–1856, Nov 1997.

[87] C. Molpeceres, S. Lauzurica, J. J. Garcia-Ballesteros, M. Morales, and J. L. Ocana, "Advanced 3d micromachining techniques using UV laser sources," *Microelectron. Eng.*, vol. 84, pp. 1337–1340, May-Aug 2007.

[88] R. A. Lawes, "Manufacturing costs for microsystems/MEMS using high aspect ratio microfabrication techniques," *Microsyst. Technol.*, vol. 13, pp. 85–95, Jan 2007.

[89] M. Kitsara, M. Chatzichristidi, D. Niakoula, D. Goustouridis, K. Beltsios, P. Argitis, and I. Raptis, "Layer-by-layer UV micromachining methodology of epoxy resist embedded microchannels," *Microelectron. Eng.*, vol. 83, pp. 1298–1301, Apr-Sep 2006.

[90] Q. Chen, T. Tong, J. P. Longtin, S. Tankiewicz, S. Sampath, and R. J. Gambino, "Novel sensor fabrication using direct-write thermal spray and precision laser micromachnining," *J. Manuf. Sci. E-T ASME*, vol. 126, pp. 830–836, Nov 2004.

[91] K. I. Jolic, M. K. Ghantasala, J. P. Hayes, and H. Jin, "Fabrication of three-dimensional inductor coil using excimer laser micromachining," *J. Micromech. Microeng.*, vol. 13, pp. 782–789, Sep 2003.

[92] S. Deladi, M. J. de Boer, G. Krijnen, D. Rosen, and M. C. Elwenspoek, "Innovative process development for a new micro-tribosensor using surface micromachining," *J. Micromech. Microeng.*, vol. 13, pp. S17–S22, Jul 2003.

[93] L. R. Harriot and R. Hull, *Nanolithography*, ch. 1, pp. 7–39. Norwell, MA: Kluwer Academic Publishers, 2004.

[94] R. Legtenberg, H. A. C. Tilmans, J. Elders, and M. Elwenspoek, "Stiction of surface micromachined structures after rinsing and drying: Model and investigation of adhesion mechanisms," *Sensor. Actuat. A-Phys.*, vol. 43, pp. 230–238, May 1994.

[95] J. Ricci and C. Cetinkaya, "Air-coupled acoustic method for testing and evaluation of microscale structures," *Rev.Sci. Instrum.*, vol. 78, p. Art. No. 055105, May 2007.

[96] T. Yu, R. Ranganathan, N. Johnson, N. Yadav, R. Gale, and T. Dallas, "In situ characterization of induced stiction in a MEMS," *J. Microelectromech. S.*, vol. 16, pp. 355–364, Apr 2007.

[97] B. Bhushan, "Nanotribology and nanomechanics of MEMS/NEMS and BioMEMS/BioNEMS materials and devices," *Microelectron. Eng.*, vol. 84, pp. 387–412, Mar 2007.

[98] K. J. Y. Kim, C. J. and B. Sridharan, "Comparative evaluation of drying techniques for surface micromachining," *Sensor. Actuat. A-Phys.*, vol. 64, pp. 17–26, Jan 1998.

[99] K. D. Vora, A. G. Peele, B. Y. Shew, E. C. Harvey, and J. P. Hayes, "Fabrication of support structures to prevent SU-8 stiction in high aspect ratio structures," *Microsyst. Technol.*, vol. 13, pp. 487–493, Mar 2007.

[100] H. S. Ko, C. W. Liu, and C. Gau, "Micropressure sensor fabrication without problem of stiction for a wider range of measurement," *Sensor. Actuat. A-Phys.*, vol. 138, pp. 261–267, Jul 2007.

[101] S. Evoy, M. Duemling, and T. Jaruhar, *Nanoelectromechanical Systems*, ch. 16, pp. 389–416. Norwell, MA: Kluwer Academic Publishers, 2004.

[102] L. M. Zhang, D. Uttamchandani, B. Culshaw, and P. Dobson, "Measurement of Young modulus and internal-stress in silicon microresonators using a resonant frequency technique," *Meas. Sci. Technol.*, vol. 1, pp. 1343–1346, Dec 1990.

[103] B. D. Pant and U. S. Tandon, "Etching of silicon nitride in CCl_2F_2, CHF_3, SiF_4, and SF_6 reactive plasma: A comparative study," *Plasma Chem. Plasma P.*, vol. 19, no. 4, pp. 545–563, 1999.

[104] D. W. Carr, L. Sekaric, and H. G. Craighead, "Measurement of nanomechanical resonant structures in single-crystal silicon," *J. Vac. Sci. Technol. B*, vol. 16, pp. 3821–3824, Nov-Dec 1998.

[105] J. F. Vignola, X. Liu, S. F. Morse, B. H. Houston, J. A. Bucaro, M. H. Marcus, D. M. Photiadis, and L. Sekaric, "Characterization of silicon micro-oscillators by scanning laser vibrometry," *Rev. Sci. Instru.*, vol. 73, pp. 3584–3588, Oct 2002.

[106] S. S. Verbridge, D. F. Shapiro, H. G. Craighead, and M. Parpia, "Macroscopic tuning of nanomechanics: Substrate bending for reversible control of frequency and quality factor of nanostring resonators," *Nano Lett.*, vol. 7, pp. 1728–1735, Jun 2007.

[107] D. M. Photiadis and J. A. Judge, "Attachment losses of high Q oscillators," *Appl. Phys. Lett.*, vol. 85, pp. 482–484, Jul 2004.

[108] P. G. Datskos, N. V. Lavrik, and M. J. Sepaniak, *Micromechanical Sensors*, ch. 17, pp. 417–439. Norwell, MA: Kluwer Academic Publishers, 2004.

[109] R. A. Buser and N. F. De Rooij, "Very-high Q-factor resonators in monocrystalline silicon," *Sensor. Actuat. A-Phys.*, vol. 21, pp. 323–327, Feb 1990.

[110] X. Liu, J. F. Vignola, D. M. Photiadis, A. Sarkissian, B. H. Houston, R. D. Merithew, and R. O. Pohl, "Low temperature study of loss mechanisms of mechanical oscillators," *Physica B*, vol. 316, pp. 393–396, May 2002.

[111] C. N. Hahtela, O. and I. Tittonen, "Non-tilting out-of-plane mode high-Q mechanical silicon oscillator," *J. Micromech. Microeng.*, vol. 15, pp. 1848–1853, Oct 2005.

[112] S. S. Verbridge, J. M. Parpia, R. B. Reichenbach, L. M. Bellan, and H. G. Craighead, "High quality factor resonance at room temperature with nanostrings under high tensile stress," *J. Appl. Phys.*, vol. 99, p. Art. No. 124304, Jun 2006.

[113] K. Y. Yasumura, T. D. Stowe, E. M. Chow, T. Pfafman, T. W. Kenny, B. C. Stipe, and D. Rugar, "Quality factors in micron- and submicron-thick cantilevers," *J. Microelectromech. S.*, vol. 9, pp. 117–125, Mar 2000.

[114] D. A. Czaplewski, J. P. Sullivan, T. A. Friedmann, D. W. Carr, B. E. N. Keeler, and J. R. Wendt, "Mechanical dissipation in tetrahedral amorphous carbon," *J. Appl. Phys.*, vol. 97, p. Art. No. 023517, Jan 2005.

[115] B. L. Zink and F. Hellman, "Specific heat and thermal conductivity of low-stress amorphous Si-N membranes," *Solid State Commun.*, vol. 129, pp. 199–204, Jan 2004.

[116] D. R. Shankaran, K. Gobi, and N. Miura, "Recent advancements in surface plasmon resonance immunosensors for detection of small molecules of biomedical, food and environmental interest," *Sensor. Actuat. B*, vol. 121, pp. 158–177, Jan 2007.

[117] K. A. Marx, "Quartz crystal microbalance: A useful tool for studying thin polymer films and complex biomolecular systems at the solution-surface interface," *Biomacromolecules*, vol. 4, pp. 1099–1120, Sep-Oct 2003.

[118] M. A. Rahman, M. J. A. Shiddiky, J. S. Park, and Y. B. Shim, "An impedimetric immunosensor for the label-free detection of bisphenol A," *Biosens. Bioelectron.*, vol. 22, pp. 2464–2470, May 2007.

[119] K. V. Gobi, H. Iwasaka, and N. Miura, "Self-assembled PEG monolayer based SPR immunosensor for label-free detection of insulin," *Biosens. Bioelectron.*, vol. 22, pp. 1382–1389, Feb 2007.

[120] B. Sun, P. E. Colavita, H. Kim, M. Lockett, M. S. Marcus, L. M. Smith, and R. J. Hamers, "Covalent photochemical functionalization of amorphous carbon thin films for integrated real-time biosensing," *Langmuir*, vol. 22, pp. 9598–9605, Nov 2006.

[121] B. D. Spangler and B. J. Tyler, "Capture agents for a quartz crystal microbalance-continuous flow biosensor: functionalized self-assembled monolayers on gold," *Anal. Chim. Acta*, vol. 399, pp. 51–62, Nov 1999.

[122] T. Kawaguchi, D. R. Shankaran, G. K. V. Kim, S. J., K. Matsumoto, K. Toko, and N. Miura, "Fabrication of a novel immunosensor using functionalized self-

assembled monolayer for trace level detection of TNT by surface plasmon resonance," *Talanta*, vol. 72, pp. 554–560, Apr 2007.

[123] G. Wenz and P. Liepold, "Self-assembly of biotin and thio-functionalized carboxymethyl celluloses on gold and molecular recognition of streptavidin detected by surface plasmon resonance," *Cellulose*, vol. 14, pp. 89–98, Apr 2007.

[124] D. R. Reyes, D. Iossifidis, P. A. Auroux, and A. Manz, "Micro total analysis systems. 1. introduction, theory, and technology," *Anal. Chem.*, vol. 74, pp. 2623–2636, Jun 2002.

[125] J. Fritz, M. K. Baller, H. P. Lang, H. Rothuizen, P. Vettiger, E. Meyer, H. J. Guntherodt, C. Gerber, and J. K. Gimzewski, "Translating biomolecular recognition into nanomechanics," *Science*, vol. 288, pp. 316–318, Apr 2000.

[126] H. F. Ji and T. Thundat, "In situ detection of calcium ions with chemically modified microcantilevers," *Biosens. Bioelectron.*, vol. 17, pp. 337–343, Apr 2002.

[127] S. Cherian, R. K. Gupta, B. C. Mullin, and T. Thundat, "Detection of heavy metal ions using protein-functionalized microcantilever sensors," *Biosens. Bioelectron.*, vol. 19, pp. 411–416, Dec 2003.

[128] K. S. Hwang, J. H. Lee, J. Park, D. S. Yoon, J. H. Park, and T. S. Kim, "In-situ quantitative analysis of a prostate-specific antigen (PSA) using a nanomechanical PZT cantilever," *Lab Chip*, vol. 4, no. 6, pp. 547–552, 2004.

[129] A. Kumar, S. Aravamudhan, M. Gordic, S. Bhansali, and S. S. Mohaptra, "Ultrasensitive detection of cortisol with enzyme fragment complementation technology using functionalized nanowire," *Biosens. Bioelectron.*, vol. 22, pp. 2138–2144, Apr 2007.

[130] S. K. Yoo, J. H. Lee, S. S. Yun, M. B. Gu, and J. H. Lee, "Fabrication of a bio-MEMS based cell-chip for toxicity monitoring," *Biosens. Bioelectron.*, vol. 22, pp. 1586–1592, Mar 2007.

[131] T. Adrega, D. M. F. Prazeres, V. Chu, and J. P. Conde, "Thin-film silicon MEMS DNA sensors," *J. Non-Cryst. Solids*, vol. 352, pp. 1999–2003, Jun 2006.

[132] A. Ulman, "Formation and structure of self-assembled monolayers," *Chem. Rev.*, vol. 96, pp. 1533–1554, Jun 1996.

[133] R. Shenhar, T. B. Norsten, and V. M. Rotello, *Self-Assembly and Self-Organization*, ch. 2, pp. 41–72. Norwell, MA: Kluwer Academic Publishers, 2004.

[134] S. Flink, F. C. J. M. van Veggel, and D. N. Reinhoudt, "Sensor functionalities in self-assembled monolayers," *Adv. Mater.*, vol. 12, pp. 1315–1328, Sep 2000.

[135] S. Ferretti, S. Paynter, D. A. Russell, and K. E. Sapsford, "Self-assembled monolayers: a versatile tool for the formulation of bio-surfaces," *Trac. Trend. Anal. Chem.*, vol. 19, no. 9, pp. 530–540, 2000.

[136] D. J. Revell, J. R. Knight, D. J. Blyth, A. H. Haines, and D. A. Russell, "Self-assembled carbohydrate monolayers: Formation and surface selective molecular recognition," *Langmuir*, vol. 14, pp. 4517–4524, Aug 1998.

[137] N. K. Chaki and K. Vijayamohanan, "Self-assembled monolayers as a tunable platform for biosensor applications," *Biosens. Bioelectron.*, vol. 17, pp. 1–12, Jan 2002.

[138] C. Boozer, J. Ladd, S. F. Chen, Q. Yu, J. Homola, and S. Y. Jiang, "DNA directed protein immobilization on mixed ssDNA/oligo(ethylene glycol) self-assembled monolayers for sensitive biosensors," *Anal. Chem.*, vol. 76, pp. 6967–6972, Dec 2004.

[139] J. Lahiri, L. Isaacs, and W. G. M. Tien, J., "A strategy for the generation of surfaces presenting ligands for studies of binding based on an active ester as a common reactive intermediate: A surface plasmon resonance study," *Anal. Chem.*, vol. 71, pp. 777–790, Feb 1999.

[140] S. Susmel, C. K. O'Sullivan, and G. Guilbault, "Human cytomegalovirus detection by a quartz crystal microbalance immunosensor," *Enzyme Microb. Tech.*, vol. 27, pp. 639–645, Nov 2000.

[141] V. Dauksaite, M. Lorentzen, F. Besenbacher, and J. Kjems, "Antibody-based protein detection using piezoresistive cantilever arrays," *Nanotechnology*, vol. 18, p. Art. No. 125503, Mar 2007.

[142] M. Alvarez, A. Calle, J. Tamayo, L. M. Lechuga, A. Abad, and A. Montoya, "Development of nanomechanical biosensors for detection of the pesticide DDT," *Biosens. Bioelectron.*, vol. 18, pp. 649–653, May 2003.

[143] A. Olkhovets, S. Evoy, D. W. Carr, J. M. Parpia, and H. G. Craighead, "Actuation and interanl friction of torsional nanomechanical silicon resonators," *J. Vac. Sci. Technol. B*, vol. 18, pp. 3549–3551, Nov-Dec 2000.

[144] M. K. Sandberg, R., A. Boisen, and W. Svendsen, "Effect of gold coating on the Q-factor of a resonant cantilever," *J. Micromech. Microeng.*, vol. 15, pp. 2249–2253, Dec 2005.

[145] S. Prabhakar and S. Vengallatore, "Thermoelastic damping in bilayered micromechanical beam resonators," *J. Micromech. Microeng.*, vol. 17, pp. 532–538, Mar 2007.

[146] B. Ilic, H. G. Craighead, S. Krylov, W. Senaratne, C. Ober, and P. Neuzil, "Attogram detection using nanoelectromechanical oscillators," *J. Appl. Phys.*, vol. 95, pp. 3694–3703, Apr 2004.

[147] P. K. G. Thames, S. F., "Organosilane polymer chemistry: a review," *J. Inorg. Organomet. P.*, vol. 6, pp. 59–94, Jun 1996.

[148] J. M. Buriak, "Organometallic chemistry on silicon and germanium surfaces," *Chem. Rev.*, vol. 102, pp. 1272–1306, May 2002.

[149] M. A. Brook, *Silicon in organic, organometallic, and polymer chemistry*. New York, NY: John Wiley & Sons, Inc., 2000.

[150] G. Y. Jung, Z. Y. Li, W. Wu, Y. Chen, D. L. Olynick, S. Y. Wang, W. M. Tong, and R. S. Williams, "Vapor-phase self-assembled monolayer for improved mold release in nanoimprint lithography," *Langmuir*, vol. 21, pp. 1158–1161, Feb 2005.

[151] M. T. McDermott. Private Communications, Sep-Dec 2006.

[152] K. Y. Sasidharan, M., N. K. Mal, and F. Mizukami, "Synthesis, characterization, and application of mesoporous silica functionalized with alkyl-hydroperoxides," *Adv. Funct. Mater.*, vol. 16, pp. 1853–1858, Sep 2006.

[153] K. D. Bhalerao, S. C. Lee, W. O. Soboyejo, and A. B. O. Soboyejo, "A folic acid-based functionalized surface for biosensor systems," *J. Mater. Sci. - Mater. M.*, vol. 18, pp. 3–8, Jan 2007.

[154] A. G. Mantzila and M. I. Prodromidis, "Performance of impedimetric biosensors based on anodically formed Ti/TiO$_2$ electrodes," *Electroanal.*, vol. 17, pp. 1878–1885, Oct 2005.

[155] R. M. J. Petoral, G. R. Yazdi, A. L. Spetz, R. Yakimova, and K. Uvdal, "Organosilane-functionalized wide band gap semiconductor surfaces," *Appl. Phys. Lett.*, vol. 90, p. Art. No. 223904, May 2007.

[156] E. J. Moore, M. Curtin, J. Ionita, A. R. Maguire, G. Ceccone, and P. Galvin, "Selective release of DNA from the surface of indium-tin oxide thin electrode films using thiol-disulfide exchange chemistry," *Anal. Chem.*, vol. 79, pp. 2050–2057, Mar 2007.

[157] M. C. Bourg, A. Badia, and R. B. Lennox, "Gold-sulfur bonding in 2d and 3d self-assembled monolayers: XPS characterization," *J. Phys. Chem.*, vol. 104, pp. 6562–6567, Apr 2000.

[158] I. Kusunoki, T. Takagaki, S. Ishidzuka, and T. T. Igari, Y., "Reaction of Si surfaces with a C$_2$H$_4$ beam," *Surf. Sci.*, vol. 380, pp. 131–144, May 1997.

[159] N. H. Turner and J. A. Schreifels, "Surface analysis: X-ray photoelectron spectroscopy and auger electron spectroscopy," *Anal. Chem.*, vol. 72, pp. 99R–110R, Jun 2000.

[160] D. Karpuzov. Private communications, Sep 2007.

[161] T. Thundat, G. Y. Chen, R. J. Warmack, D. P. Allison, and E. A. Wachter, "Vapor detection using resonating microcantilevers," *Anal. Chem.*, vol. 67, pp. 519–521, Feb 1995.

[162] T. Thundat, E. A. Watchter, S. L. Sharp, and R. J. Warmack, "Detection of mercury-vapor using resonating microcantilevers," *Appl. Phys. Lett.*, vol. 66, pp. 1695–1697, Mar 1995.

[163] M. Godin, P. J. Williams, V. Tabard-Cossa, O. Laroche, L. Y. Beaulieu, R. B. Lennox, and P. Grutter, "Surface stress, kinetics, and structure of alkanethiol self-assembled monolayers," *Langmuir*, vol. 20, pp. 7090–7096, Aug 2004.

[164] P. G. Datskos and I. Sauers, "Detection of 2-mercaptoethanol using gold-coated micromachined cantilevers," *Sensor. Actuat. B-Chem.*, vol. 61, pp. 75–82, Dec 1999.

[165] M. Li, H. X. Tang, and M. L. Roukes, "Ultra-sensitive NEMS-based cantilevers for sensing, scanned probe and very high-frequency applications," *Nat. Nanotech.*, vol. 2, pp. 114–120, Feb 2007.

[166] A. Janshoff, K. P. S. Dancil, C. Steinem, D. P. Greiner, V. S. Y. Lin, C. Gurtner, K. Motesharei, M. J. Sailor, and M. R. Ghadiri, "Macroporous p-type silicon fabry-perot layers. fabrication, characterization, and applications in biosensing," *J. Am. Chem. Soc.*, vol. 120, pp. 12108–12116, Nov 1998.

[167] P. G. Datskos, S. Rajic, M. J. Sepaniak, N. Lavrik, C. A. Tipple, L. R. Senesac, and I. Datskou, "Chemical detection based on adsorption-induced and photoinduced stresses in microelectromechanical systems devices," *J. Vac. Sci. Technol. B*, vol. 19, pp. 1173–1179, Jul-Aug 2001.

[168] S. Kohale, S. M. Molina, B. L. Weeks, R. Khare, and L. J. Hope-Weeks, "Monitoring the formation of self-assembled monolayers of alkanedithiols using a micromechanical cantilever sensor," *Langmuir*, vol. 23, pp. 1258–1263, Jan 2007.

[169] A. W. McFarland and J. S. Colton, "Chemical sensing with micromolded plastic microcantilevers," *J. Microelectromech. S.*, vol. 14, pp. 1375–1385, Dec 2005.

[170] P. A. Rasmussen, A. V. Grigorov, and A. Boisen, "Double sided surface stress cantilever sensor," *J. Micromech. Microeng.*, vol. 15, pp. 1088–1091, May 2005.

[171] K. D. Wise, "Integrated sensors, MEMS, and microsystems: Reflections on a fantastic voyage," *Sensor. Actuat. A-Phys.*, vol. 136, pp. 39–50, May 2007.

[172] M. A. Huff, D. A. Aidala, and J. E. Butler, "MEMS applications using diamond thin films," *Solid State Technol.*, vol. 49, pp. 45–+, Apr 2006.

[173] H. G. Craighead, "Nanoelectromechanical systems," *Science*, vol. 290, pp. 1532–1535, Nov 2000.

[174] K. L. Ekinci and M. L. Roukes, "Nanoelectromechanical systems," *Rev. Sci. Instrum.*, vol. 76, p. Art. No. 061101, Jun 2005.

[175] H. C. Nathanson, W. E. Newell, R. A. Wickstrom, and J. R. Davis, "The resonant gate transistor," *IEEE T. Electron Dev.*, vol. 14, no. 3, pp. 117–, 1967.

[176] W. Lang, "Silicon microstructuring technology," *Mat. Sci. Eng. R*, vol. 17, pp. 1–55, Sep 1996.

[177] B. Ilic, D. Czaplewski, H. G. Craighead, P. Neuzil, C. Campagnolo, and C. Batt, "Mechanical resonant immunospecific biological detector," *Appl. Phys. Lett.*, vol. 77, pp. 450–452, Jul 2000.